Theory and Experiment of Slow-Light Coupled-Resonator Structures

Thesis by

Hsi-Chun Liu

In Partial Fulfillment of the Requirements for the

Degree of

Doctor of Philosophy

California Institute of Technology

Pasadena, California

2012

(Defended May 16 2012)

Thesis Committee

Professor Amnon Yariv (Chair)

Professor Bruno Crosignani

Professor P. P. Vaidyanathan

Professor Kerry Vahala

Professor Changhuei Yang

Acknowledgements

I am grateful for the many people who have supported and encouraged me during my doctoral studies at Caltech. I am thankful for Prof. Amnon Yariv for giving me the opportunity to conduct research in this supportive environment and the freedom to mature as a researcher. I have always enjoyed discussing physics and ideas with him. Through our frequent interaction, especially my first summer at Caltech, I have acquired a lot of knowledge and built up my confidence as a researcher. His keen physical intuition and consistent enthusiasm have always been a constant source of motivation and inspiration.

I thank Profs. Bruno Crosignani, P. P. Vaidyanathan, Changhuei Yang, and Kerry Vahala for being part of my thesis committee, as well as Prof. Oskar Painter who was part of my candidacy committee. I enjoyed working with Prof. Bruno Crosignani on solving interesting physics problems. I thank Dr. Willie Ng of HRL Laboratories for collaborating with us on the iPhod project.

I would like to thank the past and current members of our research group. I am most grateful to Christos Santis who collaborated with me on our grating CROW projects. We started our collaboration three years ago when we had no experience on fabrication and testing of silicon photonic devices. We learned from failure and adjusted the fabrication process, design, and experimental setup. We shared lots of research ideas. Without him, I would not have accomplished so much. I am thankful for Sinan Zhao who has been the person I shared many theoretical ideas with. He catches up with new things quickly and is always eager to learn. Our work on waveguide bends and high-Q racetrack resonators is an interesting and surprising outcome of the iPhod project. I would like to thank Dr. Xiankai Sun, who worked with me on the design of adiabatic mode converters on hybrid

Si/III-V platform and the iPhod project. He was always kind enough to help me and give me advice. I am thankful for Prof. Joyce Poon, who was my mentor in my first year at Caltech. She instructed me in working on my first research project at Caltech. I would like to thank Dr. Naresh Satyan, for all the helpful input and suggestions for my theory and experiment. I am grateful to Jacob Sendowski and Scott Steger, who have helped me on the optical setup and sample processing. I have enjoyed technical and other discussions with Arseny Vasilyev, Yasha Vilenchik, and Mark Harfouche. I am thankful for Dr. John Choi, Dr. Wei Liang, Dr. Philip Chak, Dr. Reginald Lee, Prof. Avi Zadok, Prof. Lin Zhu, for their support in my early years at Caltech. I would like to thank Connie Rodriguez who looks after our group thoughtfully. I also thank Ali Ghaffari, Kevin Cooper, and Mabel Chik for their support.

I would like to acknowledge the support from National Science Council in Taiwan (Taiwan Merit Scholarship TMS-094-2-A-039) for my first three years at Caltech. The work in this thesis was financially supported by National Science Foundation (Award No. 0925389) and the Army Research Office (Award No. W911NF-10-1-0103).

I would like to thank the Taiwanese community at Caltech, who looked after me when I first came to Caltech. I am fortunate to have formed so many friendships. Every weekend we gathered for dinner and grocery shopping, played softball and board games. There are lots of memories that I will never forget.

Above all, I would like to express my deepest gratitude to my Dad, my Mom, and my lovely wife, Kai-Wei, for their endless support and encouragement. Kai-Wei and I came to the United States for our doctoral studies in the same year. During our long-distance relationship, we travelled a lot between California and Texas to meet each other. I am thankful for her steadfast love, sacrifice, understanding, and the many things she has done for me.

Abstract

Slow light has been an inter-disciplinary topic and a rapidly growing area, especially over the last decade with the improvement of fabrication technology. The ability to slow down and control the group velocity of light may find applications such as optical buffers, optical delay lines, and enhanced light-matter interaction in optical modulator, amplifier, detectors, lasers, and nonlinear optics. The spirit of slow light is to replace a bulky device with a much shorter, compact structure.

This thesis explores the design and experiment of coupled-resonator optical waveguides (CROWs), which consist of arrays of optical resonators in which light propagates through the coupling between resonators. The group velocity of light is dictated by the inter-resonator coupling strength. Light can be significantly slowed down if the inter-resonator coupling is weak. CROWs can be realized with various types of resonators. This thesis focuses on grating resonators in silicon waveguides, including grating-defect resonators and bandgap-modulated resonators. With the strong gratings, the grating resonators are only a few microns long. We control the inter-resonator coupling via the number of holes between adjacent resonators.

The major limitations in the realization of CROWs have been various kinds of transmission losses, including the resonator losses, the discontinuity between CROWs and the coupling waveguides, and the fabrication disorder. These transmission losses limit the achievable group velocity and the maximum number of resonators. We address these transmission losses throughout this thesis. The resonator losses are overcome with the design and optimized fabrication of tapered grating-defect resonators and bandgap-modulated resonators. The discontinuity between CROWs and waveguides is reduced by tailoring the coupling along the CROW for adiabatic conversion. The optimization of the CROW response leads to the study of filter design based on CROW. Filter design formalism based on coupled-mode theory is presented. The effect of fabrication disorder on CROWs is analyzed, and the Butterworth filters are shown to be more robust against fabrication disorder. The fabrication and measurement of grating CROWs are presented, featuring high-Q (Q=10^5) grating resonators, coupling of up to 50 resonators, control of group velocity between c/13 and c/49, and Butterworth filters.

Finally, an optical analog of electromagnetically induced transparency is presented. The structure consists of two co-spatial gratings imposed on a three-mode waveguide. One of the supermodes, the Dark mode, possesses a group velocity which depends on the ratio of the grating strengths. The group velocity can be nearly zero if the two grating strengths are nearly identical.

Contents

List of Figures

List of Tables

Glossary of Acronyms

DBP Delay-bandwidth product

CMT Coupled-mode theory

CROW Coupled-resonator optical waveguide

TMM Transfer matrix method

QWS Quarter wave shift

MMM Mode-matching method

SSC Spot-size converter

TE Transverse electric

NA Numerical aperture

APD Avalanche photodiode

EIT Electromagnetically induced transparency

GIT Grating induced transparency

Chapter 1

Overview

1.1 Slow Light — Reducing the Group Velocity of Light

The term “slow light” refers to a reduction in the group velocity of light. Group velocity of light is usually compared with the phase velocity, the velocity with which the wave fronts propagate. For a monochromatic wave $\cos(\omega t - kx)$ propagating in the x direction, the phase velocity is given by $v_p = \omega / k$. Group velocity refers to the velocity of the “envelope”, i.e., the amplitude of the sinusoidal wave. Considering a wave $\mathrm{A}(x,t)\cos(\omega t - kx)$ with the slowly varying envelope $\mathrm{A}(x,t)$, the velocity with which $\mathrm{A}(x,t)$ propagates is called group velocity since an envelope $\mathrm{A}(x,t)$ consists of a group of sinusoidal waves.

The propagation of the envelope can be described in terms of interference between frequency components around ω, which results in a group velocity given by $v_g = \partial\omega / \partial k$. The group velocity is also expressed as c / n_g, where n_g denotes the group index and is given by

$$n_g = n + \omega \frac{dn}{d\omega}, \tag{1-1}$$

where n is the material refractive index or the effective index of a waveguide. For materials with normal dispersion ($dn / d\omega > 0$), group velocity is smaller than phase velocity. In most cases, we consider the group velocity rather than the phase velocity–the

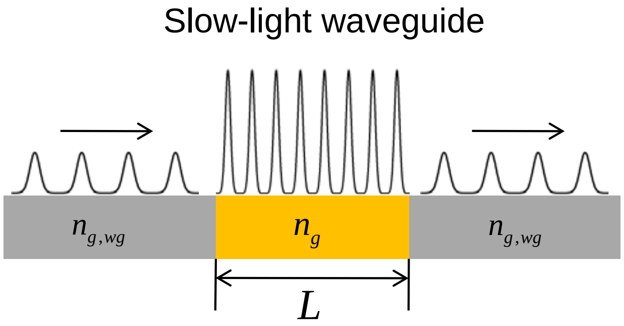

Fig. 1.1. Schematic drawing of a pulse train entering a slow-light waveguide

propagation of optical pulses, optical signals in communication systems, or even turning on a laser. Group velocity determines how fast signals travel and when the signals arrive at the destination.

In normally dispersive ($v_g < v_p$) and nondissipative media, group velocity is equal to energy velocity, v_e, which is given by the Poynting vector S divided by the energy density [1]. When group velocity is varied along the propagating direction, energy density is inversely proportional to the group velocity for conservation of energy. In other words, the flow of photons can be harnessed via controlling the group velocity of light.

Fig. 1.1 shows a pulse train entering a slow-light waveguide with a group index n_g from a conventional waveguide with a group index $n_{g,wg}$. We define a slowing factor $S \equiv n_g / n_{g,wg}$. The spatial pulse lengths are squeezed in the slow-light waveguide, and the intensity of light is enhanced, both by the slowing factor. The time it takes to pass through the slow-light waveguide is known as the group delay, which is given by $n_g L / c$.

1.2 Applications of Slow Light

One important application of slow light is for optical buffers and delay lines. In optical packet switch (OPS) applications, buffers are required for synchronization of incoming packets and for collision avoidance on outgoing lightpaths [2]. Optical delay lines are useful for phase control in interferometers [3] and phased-array laser radars [4]. Delay lines based on conventional waveguides are typically very long. The length can be greatly reduced if the group velocity of light is significantly slowed down. An important parameter of optical buffers is the capacity, which refers to the number of bits that can be stored in the buffer. The capacity is equal to the delay-bandwidth product (DBP), $\tau \cdot \Delta f$ [2]. For example, although large group delay can be achieved with a high-Q resonator, the bandwidth is inversely proportional to the delay, and the DBP is smaller than one. Therefore, a single resonator is only capable of delaying one bit.

Another application of slow light is the enhanced light-matter interaction due to the enhanced intensity of light. Slow light can enhance optical gain, absorption, and nonlinearity per unit length, which enables compact optical devices such as modulators, detectors, amplifiers, and lasers [5]. The enhancement of optical nonlinearity by slow light is especially promising. For third-order nonlinear process, the effective nonlinear coefficient is proportional to S^2, and the wavelength conversion efficiency is proportional to S^4 [6, 7]. Slow light enhanced nonlinear optics has been demonstrated in four-wave mixing [7-10], third harmonic generation [11], XOR logic gates [12], and optical demultiplexing [13]. For ultrafast all-optical signal processing, the bandwidth of slow-light devices is strongly desirable.

1.3 Approaches to Achieve Slow Light

Slow light has been an inter-disciplinary topic and can be realized with many different approaches. One category is based on material resonances, such as sharp absorption resonances of atomic vapor or nonlinear optics. Examples are electromagnetically induced transparency (EIT) [14], coherent population oscillations (CPO) [15], stimulated Brillouin scattering [16], and stimulated Raman scattering [17]. The general characteristic

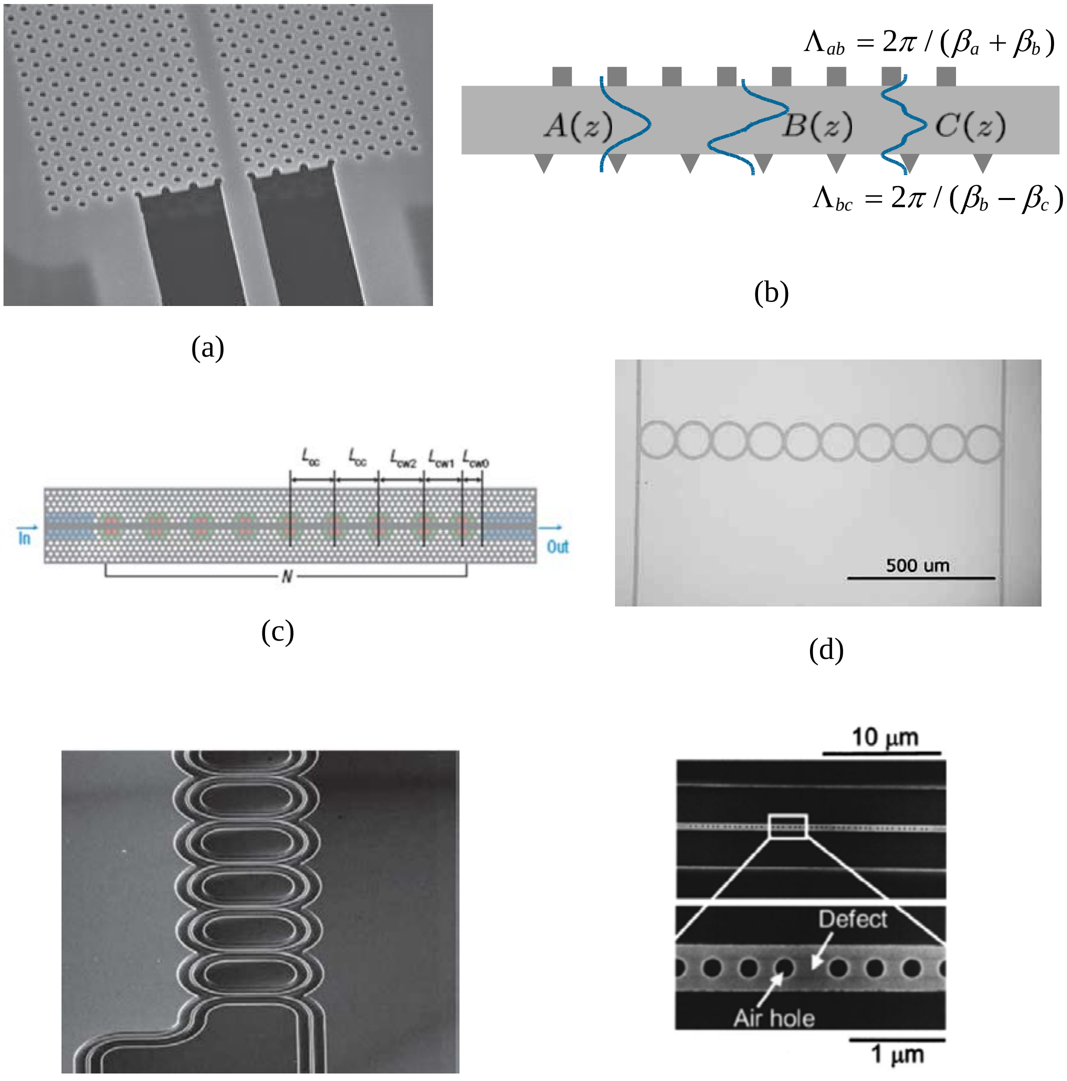

(a) (b) (c) (d) (e) (f)

Fig. 1.2. Various types of slow-light structures. (a) Photonic crystal waveguide [11]. (b) Grating structures [18]. (c–f) coupled-resonators optical waveguides based on (c) photonic crystal resonators [19], (d) polymer ring resonators [20], (e) silicon racetrack resonators [21], and (f) silicon grating resonators [22]

is a narrow resonance which corresponds to strong dispersion according to Kramers-Kronig relations which relate the real and imaginary parts of the refractive index. A peak in the gain spectrum or a dip in absorption spectrum leads to strong normal dispersion ($dn/d\omega \gg 0$) and thus slow light, whereas a dip in the gain spectrum or a peak in absorption spectrum leads to strong anomalous dispersion ($dn/d\omega \ll 0$) and fast light.

Slow-light media based on material resonances are usually bulky and working at low temperature. Group velocity as small as 17 m/s has been demonstrated [14], but the bandwidth is ultra-narrow.

The other category is engineered photonic structures where light bounces back and forth as it propagates forward. Examples of engineered structures are photonic crystal waveguides, where a line defect is introduced in a two-dimensional periodic structure (Fig. 1.2(a)) [23, 24], grating structures based on modulation of gratings or superimposed dual gratings (Fig. 1.2(b)) [18, 25], and coupled-resonator structures (Fig. 1.2(c–f)) [19-22, 26]. The general characteristic is a dispersion curve $\omega(k)$ whose slope $d\omega/dk$ is small over a range of frequencies. While the group velocity at the band edge of a dispersion curve approaches zero, the second-order dispersion $d^2\omega/dk^2$ is large, which causes distortion of signal and limits the bandwidth. The design of engineered slow-light structures aims at a linear, flat band over a range of frequencies so that the higher-order dispersion is small. The group velocity of engineered structures is more moderate, typically c/100 to c/10. However, their bandwidths are much larger, and they are capable of delaying many bit signals. Engineered photonic structures are more compact, able to work in room temperature, and compatible with advanced fabrication technology.

1.4 Coupled-Resonator Optical Waveguides (CROWs)

A coupled-resonator optical waveguide consists of a chain of weakly-coupled optical resonators, as shown in Fig. 1.3 [26]. Light with a frequency near resonance can propagate along a CROW through the inter-resonator coupling. The properties of CROWs such as group velocity and bandwidth are dictated solely by the coupling coefficient κ and are independent of the type of resonators. CROWs can be realized in various types of resonators, such as photonic crystal resonators [9, 19], microring

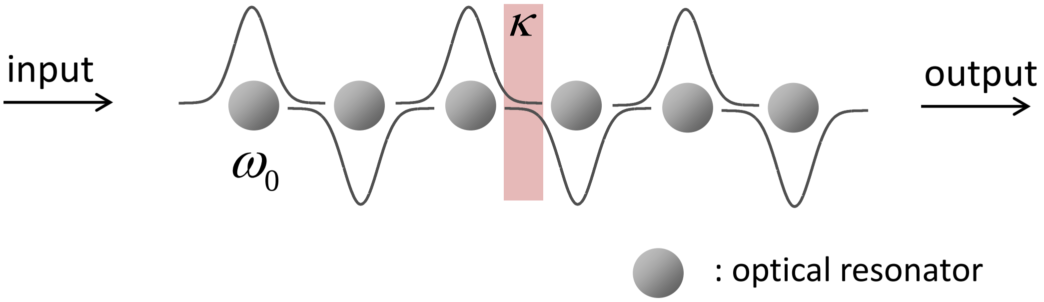

Fig. 1.3. Schematic drawing of a CROW

resonators [7, 20, 21, 24], microdisk resonators [27], and waveguide-grating resonators [22, 28], as shown in Fig. 1.2(c–f).

Since the first proposal of CROWs in 1999, numerous research works in both theory and experiment have been demonstrated, including CROWs based on different types of resonators, CROWs in different materials, CROWs with tunable delay [29], CROWs with tailored coupling coefficients for filter design [30-35], and nonlinear optics in CROWs [14-16]. The major limitation of CROWs has been the transmission losses, including: (i) Intrinsic loss of individual resonators which constitute the CROW. The resonator losses include the theoretical loss from the resonator design, fabrication imperfection such as surface roughness, and material loss. Resonator losses are especially critical for slow-light delay lines, since the total loss is proportional to the group delay. Therefore, improving the quality factor of individual resonators is essential for CROWs. (ii) The discontinuity between the CROW and the input and output waveguides. The discontinuity between the CROW mode and the waveguide mode causes reflection and results in Fabry-Perot-like oscillations in the transmission spectrum so that not every frequency component inside the passband is able to transmit. (iii) Fabrication imperfection which leads to the deviation of resonant frequencies and coupling coefficients from the designed values. The fabrication disorder distorts the transmission spectra of CROWs. These three types of transmission losses due to both design and fabrication lead to practical limitation on the maximum number of resonators in a CROW and the minimum group of velocity that can be achieved with CROWs.

1.5 Motivation and Organization of the Thesis

This thesis presents the theory and experiment of CROWs based on grating resonators in silicon waveguides. While CROWs are most commonly based on ring resonators, waveguide-grating resonators offer a few advantages. First, the implementation of grating CROWs on waveguides is natural and convenient. Grating structures are fabricated on waveguides to change the group velocity of light, without additional design for the coupling between CROWs and waveguides. Second, the footprints of grating resonators are small. Each resonator is only a few microns long in a waveguide due to the strong grating. Third, the control of inter-resonator coupling is via the number of holes and is accurate and convenient for designing CROWs with tailored coupling coefficients. However, grating-defect resonators without special design possess low quality factor which leads to large propagation loss [22, 36]. The design of grating-defect CROWs, including the reduction of propagation loss and the control of coupling coefficients, has not been investigated.

We present systematic design of grating-defect CROWs in this thesis. We address the three sources of transmission losses discussed in Section 1.4 , by tailoring the coupling coefficient along the CROWs and by designing high-*Q* grating resonators. In Chapter 2 and Chapter 3, we focus on the design of coupling coefficients along CROWs, for optimized transmission and group delay spectra. We present a formalism for deriving the coupling coefficients of CROWs which satisfy desired filter responses such as Butterworth and Bessel filters. In particular, Butterworth filters possess maximally flat transmission and are shown to be more robust against fabrication disorder. In Chapter 3, we propose a modified design of CROWs which are based on reflecting and tailored-coupling CROWs. This reflecting CROW possesses constant amplitude in reflection and constant group delay over a prescribed bandwidth and is considered as an “ideal” delay line which is capable of delaying optical signals without any distortion.

In Chapter 4, we introduce grating-defect resonators in silicon waveguides. We start with coupled-mode equations for designing grating-defect CROWs. We discuss the loss mechanism of grating-defect resonators in strong gratings. To reduce the coupling to radiation modes, we taper the holes near the defects. With spatial Fourier analysis, we systematically design the taper profile and optimize the quality factor. We demonstrate in simulation the design of coupling coefficients for controlling the group velocity.

The fabrication and measurement of grating-defect CROWs in silicon waveguides are shown in Chapter 5. We introduce the design and performance of on-chip couplers, such as spot-size converters and grating couplers. We show experimental results of Butterworth filters, CROWs with up to 50 resonators, and a group velocity of c/49. We show in experiment that Butterworth filter design provides more tolerance against fabrication disorder.

In Chapter 6, we introduce another type of high-Q grating resonators which are based on spatial modulation of grating bandgap. These resonators are known to possess higher Q. Because the resonant frequency is near the band edge of the grating band gap, the coupling of resonators for CROWs requires additional coupling sections. Experiment results are reported.

In Chapter 7, we present our earlier work on slow-light grating structures. This work is an optical analogy of electromagnetically induced transparency and is named grating induced transparency (GIT). It consists of two co-spatial gratings on a three-mode waveguide and possesses a Dark mode whose group velocity can be controlled via the ratio of the two grating strengths.

Finally, we summarize our work on slow light and CROWs in this thesis and discuss the future work.

Chapter 2

Tailoring the Coupling Coefficients of CROWs — Filter Design

2.1 Introduction

The first proposal and analysis of CROWs was based on infinite-length chains whose dispersion properties can be derived and are controlled by essentially a single parameter, the coupling coefficient κ [26]. In practice, an infinite-length CROW has to be terminated and coupled to the outside world. The resulting finite-length CROW requires a proper design because the reflection at the two boundaries leads to Fabry-Perot-type oscillations and therefore ripples in the passband of the transmission spectra, resulting in signal distortion. To minimize the reflection, the boundary coupling coefficients should be properly chosen [37]. The coupling coefficients near the boundary can also be apodized to adiabatically transform between the CROW mode and the waveguide modes [38, 39].

A further optimization of CROW delay lines consists of a judicious choice of all the coupling coefficients. Each resonator in a CROW can be considered as a feed-back loop which contributes a pole to the transfer function of the CROW. Therefore, the transfer function of an N-resonator CROW is an N-pole optical filter. The coupling coefficients of CROWs can be chosen to achieve desired properties such as maximally flat transmission (Butterworth filters) or maximally flat group delay (Bessel filters) over a prescribed bandwidth. Optical bandpass filters are important elements in optical signal processing, especially for wavelength-division-multiplexed (WDM) systems [40]. High-order bandpass filters based on coupled ring resonators have been extensively studied and experimentally demonstrated [30-34]. Filters based on coupled-resonator systems can also be realized on grating resonators [22, 28] and photonic crystal defect resonators [19, 35].

A prerequisite for the synthesis of high-order optical filters is a robust and systematic approach to directly relate the desired filter transfer function to the parameters of the CROWs. Several methods have been proposed. For ring or Fabry-Perot resonators, the transfer matrix method (TMM) can be applied to analyze the forward and backward fields inside the resonators. If the cavity lengths are nearly identical, each delay is an integer multiple of a unit delay, and the CROW can be considered as a digital optical filter and analyzed by the Z-transform formalism. [40] and [41] derived extraction procedures to convert digital filter responses to the field coupling coefficients between ring resonators. A simpler method for the analysis of CROWs is the time-domain coupled-mode theory (CMT), which considers the whole field as a superposition of individual resonator modes and is independent of the type of resonators. The derived coupling coefficients are more general but have to be converted to the parameters of the type of resonators used. In [42], coupling coefficients were extracted by direct comparison of the transfer function derived from CMT and the desired filter response. The approach becomes impractical for high-order filters. Another filter design approach is based on equivalent circuits and the techniques of microwave filters. Circuit-based methods for the synthesis of high-order filters have been proposed in [43] and [44].

In this Chapter, we present a filter design formalism based on CMT and the recursive properties of the coupling matrix. Coupling coefficients are extracted using recursive relations. In contrast to [42], this formalism does not need a direct comparison and is robust for high-order filters. These universal coupling coefficients can then be converted to the parameters of the specific type of resonators comprising the CROWs. We propose a method for the conversion of the coupling coefficients. This method utilizes the resonance splitting of two coupled resonators for inter-resonator coupling and the transmission of 2-resonator CROWs for waveguide-resonator coupling. It is more accurate than the approaches proposed in [42]. Another interesting property of this formalism is that the time-domain coupling coefficients are proportional to the bandwidth of the filters. For the same kind of filters, the bandwidth can be changed easily without having to rederive the coupling coefficients. We will first describe the formalism for lossless resonators. In the presence of uniform loss or gain, a predistortion technique is applied. We demonstrate the designs of Butterworth and Bessel CROW filters on ring resonators. Filter design of CROWs based on grating defect resonators will be shown in Chapter 4.

Finally, we analyze the effect of fabrication disorder on CROWs, including CROWs with uniform coupling coefficients and Butterworth CROWs. We discuss the disorder of resonant frequencies and coupling coefficients and their effects on the transmission spectra of CROWs. We simulate the disorder losses for these two kinds of disorder and discuss the maximum number of resonators and maximum group delay in the presence of disorder.

2.2 Coupled-Mode Theory of CROWs

We start with the theory of CROWs using coupled-mode theory. Fig. 2.1(a) illustrates a CROW with an infinite number of identical resonators. The resonant frequency of each resonator is ω_0, and the inter-resonator coupling coefficient is κ. For an input frequency ω, the mode amplitude of the k-th resonator can be written as $a_k(t)\exp[i\omega t]$, where $a_k(t)$

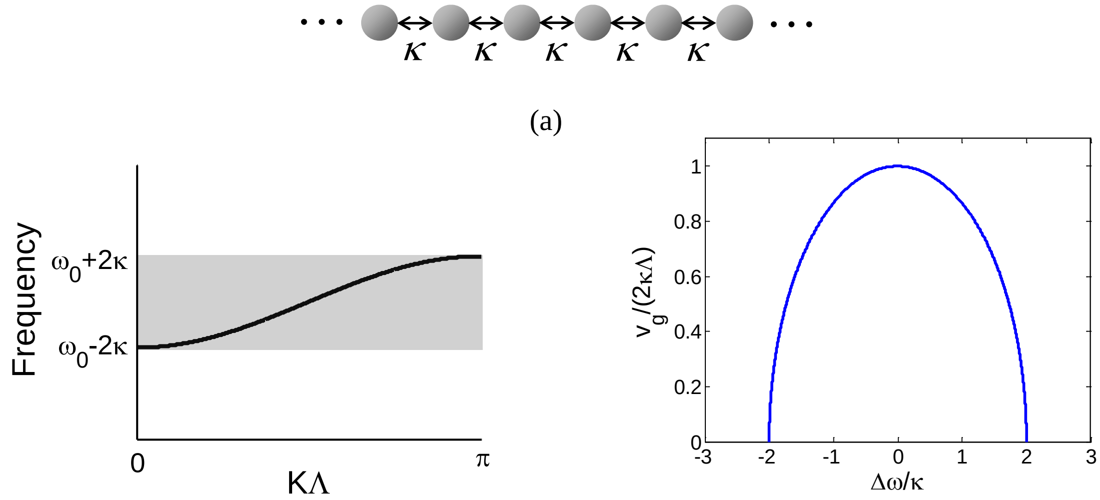

(a)

(b)

(c)

Fig. 2.1. (a) Schematic drawing, (b) dispersion curve, and (c) group velocity versus frequency of an infinite-length CROW

is the slowly-varying amplitude. $|a_k(t)|^2$ represents the energy stored in the resonator. Since the resonators are coupled only to their neighbors, the coupled-mode equation of each resonator, assumed lossless in this section, can be written as [42, 45]

$$\frac{da_k}{dt} = -i\Delta\omega a_k - i\kappa a_{k-1} - i\kappa a_{k+1}, \forall k, \tag{2-1}$$

where $\Delta\omega \equiv \omega - \omega_0$ and κ is a real number. At steady state, $da_k / dt = 0$, and Eq. (2-1) becomes a recursive formula for a_k, $\kappa a_{k+1} + \Delta\omega a_k + \kappa a_{k-1} = 0$. The general solution of this recursive formula is $a_{k+1} = \gamma a_k$, where γ is the solution of $\kappa\gamma^2 + (\Delta\omega)\gamma + \kappa = 0$. For a propagating mode (CROW mode), $\gamma = \exp[-iK\Lambda]$, where K is a wave number and Λ is the distance between adjacent resonators. A CROW mode can be found if $|\Delta\omega| < 2\kappa$, where

$$\gamma = -\frac{\Delta\omega}{2\kappa} \pm i\sqrt{1-(\frac{\Delta\omega}{2\kappa})^2} = e^{-iK\Lambda}. \tag{2-2}$$

The dispersion curve of the CROW is given by

$$\Delta\omega = -2\kappa\cos(K\Lambda), \tag{2-3}$$

as plotted in Fig. 2.1(b). The width of the CROW band is 4κ, and the group velocity of the CROW mode is

$$v_g = 2\kappa\Lambda\sin(K\Lambda) = 2\kappa\Lambda\sqrt{1-\left(\frac{\Delta\omega}{2\kappa}\right)^2}, \tag{2-4}$$

which approaches zero towards the band edges (plotted in Fig. 2.1(c)). Frequencies outside the CROW band are forbidden since K is complex and $|\gamma| \neq 1$.

2.3 Finite-Length CROWs

In practice, an infinite-length CROW has to be terminated and coupled to the outside world. Shown in Fig. 2.2(a), the first and last resonators of a CROW are coupled to the input and output waveguides. The coupling to the waveguides can be modeled as external losses, $1/\tau_e$, of the end resonators. When a CROW mode propagates to the boundary, the discontinuity between the CROW and the waveguide causes reflection, leading to Fabry-Perot-type oscillations. The reflection can be minimized by choosing $1/\tau_e$ properly. Fig.

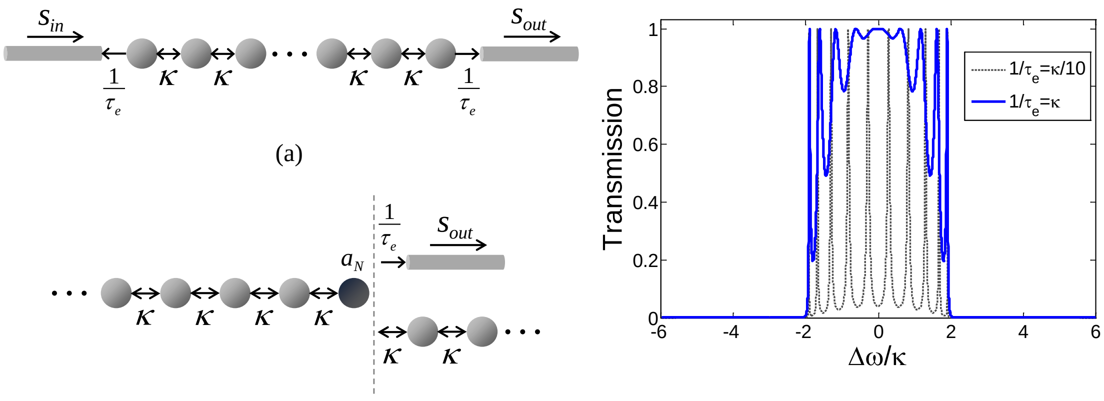

(a)

(b)

(c)

Fig. 2.2. (a) Schematic drawing of a finite-length CROW. (b) Comparison of a finite-length and an infinite-length CROW at the boundary. (e) Transmission spectra of 10-resonator CROWs with $1/\tau_e = \kappa$ and $1/\tau_e = 0.1\kappa$, respectively

2.2(b) illustrates the difference between a finite-length and an infinite-length CROW at the boundary. In the case of a finite CROW, the *N*-th resonator is coupled to the output waveguide, while in the case of an infinite CROW, it is coupled to the next resonator. The differential equations for these two cases are respectively

$$\frac{da_N}{dt} = -i\Delta\omega a_N - i\kappa a_{N-1} - \frac{1}{\tau_e} a_N \tag{2-5a}$$

and

$$\frac{da_N}{dt} = -i\Delta\omega a_N - i\kappa a_{N-1} - i\kappa a_{N+1}. \tag{2-5b}$$

To match the boundary, the right-hand sides of Eqs. (2-5a) and (2-5b) should be equal so that the *N*-th resonator cannot tell the termination of the CROW. Since $a_{N+1} = \gamma a_N$ for a CROW mode, the equality of Eqs. (2-5a) and (2-5b) requires

$$\frac{1}{\tau_e} = i\kappa\gamma. \tag{2-6}$$

For CROW modes, $|\gamma| = 1$. Eq. (2-6) requires $1/\tau_e = \kappa$ and $\gamma = -i$, which corresponds to the center of the CROW band ($\Delta\omega = 0$). Fig. 2.2(c) shows the transmission spectra of 10-resonator CROWs with $1/\tau_e = \kappa$ and $1/\tau_e = 0.1\kappa$, respectively. In the case of $1/\tau_e = \kappa$, the spectrum is flat at the band center. The ripple amplitudes increase at frequencies close to the band edge since the boundary is only matched for $\Delta\omega = 0$. For $1/\tau_e = 0.1\kappa$, the ripples are large over the whole bandwidth. Therefore, the optimal boundary condition $1/\tau_e = \kappa$ leads to maximally-flat transmission spectrum for finite-size CROWs with uniform coupling coefficients. To further reduce the Fabry-Perot oscillations over the whole CROW band, one can taper the coupling coefficients to adiabatically transform between the CROW mode and the waveguide modes [38, 39]. The spectra of transmission and group delay can be further improved by choosing all the coupling coefficients so that the transfer function of the CROW is equal to the transfer function of a desired filter, which will be described in the next section.

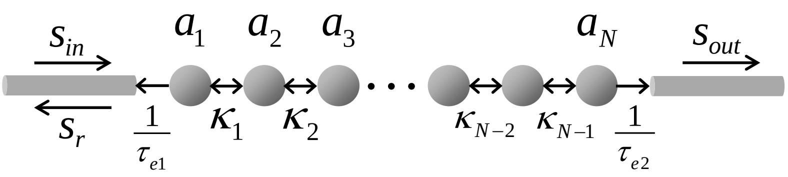

Fig. 2.3. Schematic drawing of a CROW filter

2.4 Synthesis of Bandpass Filters Based on CROWs

Consider a CROW which consists of *N* identical resonators and is coupled to input and output waveguides (Fig. 2.3). All the *N*+1 coupling coefficients are allowed to take on different values. The coupled-mode equations obeyed by the complex amplitudes of the *N* resonators are

$$\begin{aligned}
\frac{da_1}{dt} &= (-i\Delta\omega - \frac{1}{\tau_{e1}})a_1 - i\kappa_1 a_2 - i\mu_1 s_{in} \\
\frac{da_2}{dt} &= -i\Delta\omega a_2 - i\kappa_1 a_1 - i\kappa_2 a_3 \\
&\vdots \\
\frac{da_{N-1}}{dt} &= -i\Delta\omega a_{N-1} - i\kappa_{N-2} a_{N-2} - i\kappa_{N-1} a_N \\
\frac{da_N}{dt} &= (-i\Delta\omega - \frac{1}{\tau_{e2}})a_N - i\kappa_{N-1} a_{N-1}
\end{aligned} \tag{2-7}$$

The right-hand side of each equation consists of a detuning term ($-i\Delta\omega a_k$ for each *k*) and two coupling terms to the neighboring resonators, except for the first and last resonators which have only one neighbor. $1/\tau_{e1}$ and $1/\tau_{e2}$ are external losses of the first and last resonators due to coupling into the waveguides. The input mode with power $|s_{in}|^2$ is coupled into the first resonator via a coupling coefficient μ_1. It can be shown from conservation of energy and time reversal symmetry that $\mu_1 = \sqrt{2/\tau_{e1}}$ [42, 46]. At steady state, the left-hand sides of Eq. (2-7) are all 0. By replacing $i\Delta\omega$ with the Laplace variable *s*, Eq. (2-7) can be rewritten as

$$\mathrm{A}\boldsymbol{a} \equiv \begin{bmatrix} s+\frac{1}{\tau_{e1}} & i\kappa_1 & 0 & 0 & \cdots & 0 \\ i\kappa_1 & s & i\kappa_2 & 0 & \cdots & 0 \\ 0 & i\kappa_2 & s & \cdot & \cdot & \cdot \\ \cdot & \cdot & \cdot & \cdot & \cdot & \cdot \\ \cdot & \cdot & \cdot & \cdot & s & i\kappa_{N-1} \\ \cdot & \cdot & \cdot & \cdot & i\kappa_{N-1} & s+\frac{1}{\tau_{e2}} \end{bmatrix} \begin{bmatrix} a_1 \\ a_2 \\ \cdot \\ \cdot \\ \cdot \\ a_N \end{bmatrix} = \begin{bmatrix} -i\mu_1 s_{in} \\ 0 \\ \cdot \\ \cdot \\ \cdot \\ 0 \end{bmatrix}. \tag{2-8}$$

The $N \times N$ coupling matrix A is a tridiagonal matrix. The vector ***a*** which contains all the mode amplitudes can be solved by inverting A. The transmitted and reflected amplitude, s_{out} and s_r, are given, respectively, by

$$s_{out} = -i\mu_2 a_N = -\mu_1\mu_2 \left[\mathrm{A}^{-1}\right]_{N,1} s_{in} \tag{2-9a}$$

and

$$s_r = s_{in} - i\mu_1 a_1 = (1-\mu_1^{\,2}\left[\mathrm{A}^{-1}\right]_{1,1})s_{in}, \tag{2-9b}$$

where $\mu_2 = \sqrt{2/\tau_{e2}}$. The amplitude transmission, which is defined as $T \equiv s_{out}/s_{in}$, can be shown as

$$T(s) = -\frac{(-i)^{N-1}\mu_1\mu_2\kappa_1\kappa_2\cdots\kappa_{N-1}}{\det(\mathrm{A})}, \tag{2-10}$$

where det(A) is the determinant of A and is a polynomial in s with a leading term s^N. Therefore, $T(s)$ is an all-pole function with N poles.

2.4.1 *N*-th-Order All-Pole Bandpass Filters

The transfer function of an all-pole low-pass filter with N poles can be written as

$$T(s) = \frac{k}{s^N + b_{N-1}s^{N-1} + \cdots + b_1 s + b_0}, \tag{2-11}$$

where $k, b_{N-1}, \cdots, b_0$ are constants. Typical examples of all-pole filters are Butterworth, Chebyshev, and Bessel filters. We substitute s with $i(\omega-\omega_0)/B$, where B is a bandwidth parameter, $T(s)$ then describes a bandpass filter which is centered at ω_0 and of

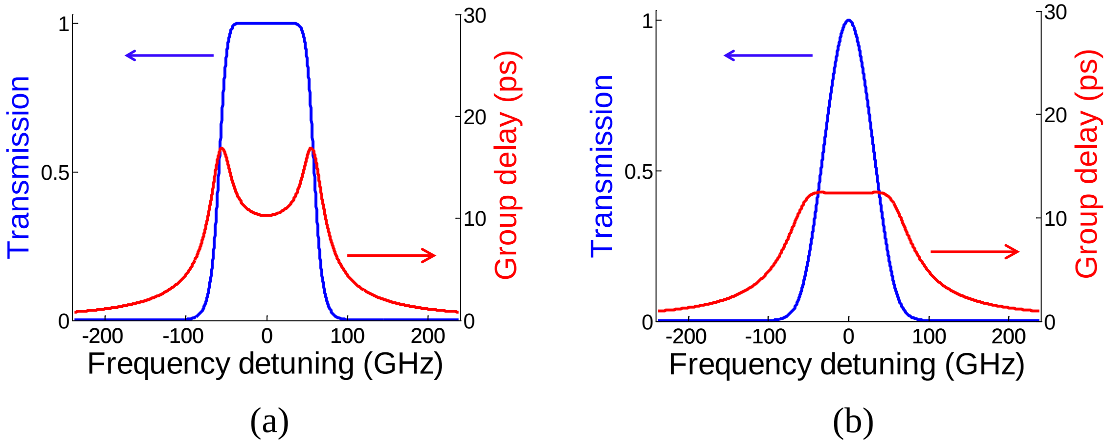

Fig. 2.4. Spectra of transmission and group delay of (a) a tenth-order Butterworth filter and (b) a tenth-order Bessel filter

bandwidth scaled by *B*. Fig. 2.4 shows the transmission and group delay spectra of a Butterworth filter and a Bessel filter which feature maximally flat transmission and maximally flat group delay, respectively.

Since the amplitude transmission of an *N*-resonator CROW (Eq. (2-10)) and the transfer function of an *N*-th-order all-pole low-pass filter (Eq. (2-11)) are both all-pole functions with *N* poles, we present in what follows a formalism for designing the coupling coefficients of CROWs so that the amplitude transmission of the CROW is equal to the desired $T(s)$.

2.4.2 Extraction of Coupling Coefficients for a Desired Filter Response

The tridiagonal matrix A in Eq. (2-8) has the following recursive properties of the polynomials p_1 through p_N:

$$\begin{aligned} p_N &= (s+\frac{1}{\tau_{e1}})p_{N-1}+{\kappa_1}^2 p_{N-2} \\ p_{N-1} &= sp_{N-2}+{\kappa_2}^2 p_{N-3} \\ &\vdots \\ p_3 &= sp_2+{\kappa_{N-2}}^2 p_1 \\ p_2 &= sp_1+{\kappa_{N-1}}^2 \\ p_1 &= s+\frac{1}{\tau_{e2}} \end{aligned} \quad , \tag{2-12}$$

where p_k is the determinant of the bottom-right $k\times k$ submatrix of A (a principal minor of A). For example, p_N is the determinant of A, and p_1 = $\mathrm{A}_{N,N}$. Each p_k is a polynomial in s with a leading term s^k. Once we know both p_N and p_{N-1}, all the coupling coefficients $(1/\tau_{e1},\kappa_1,\kappa_2,\cdots,\kappa_{N-1},1/\tau_{e2})$ can be extracted step by step, using Eq. (2-12). For example, when dividing p_N by p_{N-1}, the quotient is $s+1/\tau_{e1}$, and the remainder is ${\kappa_1}^2 p_{N-2}$. Then we can continue to divide p_{N-1} by p_{N-2}.

p_N and p_{N-1} can be obtained from the transmission and reflection of the CROW. The amplitude transmission $T\equiv s_{out}/s_{in}$ and reflection $R\equiv s_r/s_{in}$ can be shown from Eqs. (2-9a) and (2-9b) as

$$T(s)=\frac{k}{p_N} \tag{2-13a}$$

and

$$R(s)=\frac{p_N-{\mu_1}^2 p_{N-1}}{p_N}, \tag{2-13b}$$

where k is a constant. Given a desired $T(s)$, p_N is already known. To find p_{N-1}, $R(s)$ is also required and can be related to $T(s)$ using conservation of energy, $\left|T(i\omega)\right|^2+\left|R(i\omega)\right|^2=1$, for a lossless system. We perform power spectral factorization to obtain $R(s)$ from $\left|R(i\omega)\right|^2$, which can result in at most 2^N choices of the numerator of $R(s)$, each of which will correspond to different coupling coefficients. In what follows we describe the determination of $R(s)$.

2.4.3 Power Spectral Factorization for Determining R(s)

The following formalism for determining the transfer function $R(s)$ is similar to the z-domain digital filter design described in [40, 41].

Assuming the CROW is lossless, $T(s)$ and $R(s)$ are related by $|T(i\omega)|^2 + |R(i\omega)|^2 = 1$. For an all-pole filter of order *N*, $T(s)$ can be written as

$$T(s) = \frac{k}{(s-q_1)(s-q_2)\cdots(s-q_N)}, \tag{2-14}$$

where q_1 through q_N are the poles and *k* is a constant. All the filter responses $T(s)$ we consider in this thesis are real functions, so the poles come in complex conjugate pairs. Therefore,

$$|T(i\omega)|^2 = \frac{k^2}{(\omega^2+q_1{}^2)(\omega^2+q_2{}^2)\cdots(\omega^2+q_N{}^2)} \tag{2-15}$$

and

$$|R(i\omega)|^2 = 1-|T(i\omega)|^2 = \frac{(\omega^2+q_1{}^2)(\omega^2+q_2{}^2)\cdots(\omega^2+q_N{}^2)-k^2}{(\omega^2+q_1{}^2)(\omega^2+q_2{}^2)\cdots(\omega^2+q_N{}^2)}. \tag{2-16}$$

The denominators of $T(s)$ and $R(s)$ are the same, as can be seen in Eqs. (2-13a) and (2-13b). We assume that the numerator of $R(s)$ is $p(s) = (s-z_1)(s-z_2)\cdots(s-z_N)$, where z_1 through z_N are the zeros of $R(s)$. The goal is to find these zeros so that $|p(i\omega)|^2 =$ $(\omega^2+q_1{}^2)(\omega^2+q_2{}^2)\cdots(\omega^2+q_N{}^2)-k^2$. This step is called power spectral factorization. Each zero z_i is selected from a pair $(z,-z^*)$, where *z* is a complex number, so there are at most 2^N combinations of zeros. In general, $p(s)$, and thus p_{N-1}, are not real. For a filter with a complex p_{N-1}, the resonant frequencies of the resonators have to be different, and Eq. (2-8) is modified as

$$\mathrm{A}\boldsymbol{a} \equiv \begin{bmatrix} s-i\delta_1+\dfrac{1}{\tau_{e1}} & i\kappa_1 & 0 & 0 & \cdots & 0 \\ i\kappa_1 & s-i\delta_2 & i\kappa_2 & 0 & \cdots & 0 \\ 0 & i\kappa_2 & s-i\delta_3 & \cdot & \cdot & \cdot \\ \cdot & \cdot & \cdot & \cdot & \cdot & \cdot \\ \cdot & \cdot & \cdot & \cdot & s-i\delta_{N-1} & i\kappa_{N-1} \\ \cdot & \cdot & \cdot & \cdot & i\kappa_{N-1} & s-i\delta_N+\dfrac{1}{\tau_{e2}} \end{bmatrix} \begin{bmatrix} a_1 \\ a_2 \\ \cdot \\ \cdot \\ \cdot \\ a_N \end{bmatrix} = \begin{bmatrix} -i\mu_1 s_{in} \\ 0 \\ \cdot \\ \cdot \\ \cdot \\ 0 \end{bmatrix}, \quad (2\text{-}17)$$

where $\delta_i \equiv \omega_i - \omega_0$ is the frequency detuning of each resonator from ω_0. Eq. (2-12) is also modified by replacing s with $s-i\delta_i$, so δ_i can be extracted during the extracting process.

The zeros of $R(s)$ can be chosen so that p_{N-1} is real. Fig. 2.5 shows three different choices of zeros for an N=7 Bessel filter. The corresponding coupling coefficients κ and

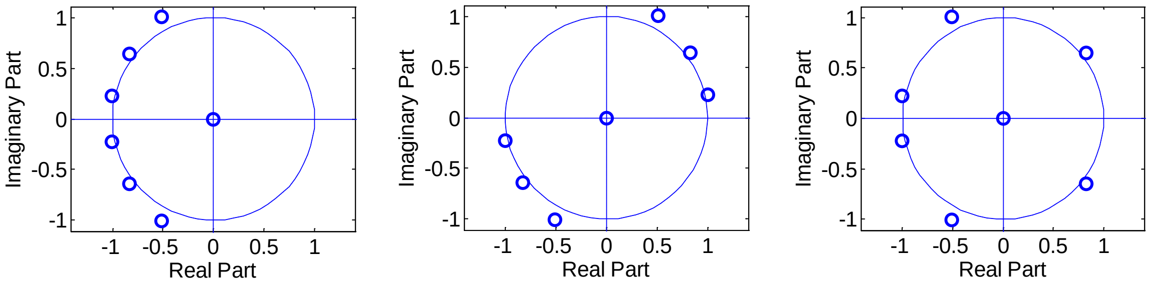

(a) (b) (c)

Fig. 2.5. Choices of zeros for R(s). (a) Minimum phase. (b) 1st and 3rd quadrants. (c) Nearly uniform distribution.

Table 2.1. Coupling coefficients of N=7 Bessel CROW filters with different choices of zeros

Choice of zeros	$\overline{\kappa} = (1/\tau_{e1}, \kappa_1, \kappa_2, \cdots, \kappa_{N-1}, 1/\tau_{e2})/B,\ \overline{\delta} = (\delta_1, \delta_2, \cdots, \delta_N)/B$
Minimum phase	$\overline{\kappa}$ = (0.241, 0.345, 0.557, 0.699, 0.899, 1.320, 2.876, 4.937) $\overline{\delta}$ = (0, 0, 0, 0, 0, 0, 0)
1st and 3rd quadrants	$\overline{\kappa}$ = (2.589, 1.460, 0.619, 0.486, 0.486, 0.619, 1.460, 2.589) $\overline{\delta}$ = (0.495, 0.514, 0.461, 0.000, –0.461, –0.514, –0.495)
Nearly uniform distribution	$\overline{\kappa}$ = (1.898, 1.174, 0.390, 0.357, 0.684, 0.932, 1.926, 3.280) $\overline{\delta}$ = (0, 0, 0, 0, 0, 0, 0)

frequency detuning δ are listed in Table 2.1. The first one is often referred to as "minimum phase", where all zeros are located inside the left-half s-plane (Fig. 2.5(a)). It corresponds to zero frequency detuning and monotonically increasing κ. In the second one, the zeros are all located at the first and third quadrants (Fig. 2.5(b)). The resulting values of κ are symmetric, but the frequency detuning is nonzero since p_{N-1} is complex. In our CROW filter design, we prefer a nearly symmetric κ without frequency detuning. Consequently, we choose the zeros that are the most uniformly distributed around the origin and are complex conjugate pairs, as shown in Fig. 2.5(c). Although the three CROW filters in Table 2.1 are very different, they correspond to the same $T(s)$ and $|R(i\omega)|^2$, except that the phase of $R(s)$ is different.

2.4.4 Coupling Coefficients of Butterworth and Bessel CROWs

Here we use an N=4 Butterworth filter to demonstrate the extraction of coupling coefficients. The transfer function $T(s) = 1/(s^4 + 2.613s^3 + 3.414s^2 + 2.613s + 1)$. The steps are listed in Table 2.2. For Butterworth filters, the power spectral factorization for solving $R(s)$ is unique and simple. The numerator of $R(s)$ is s^N. Table 2.3 lists the extracted coupling coefficients for Butterworth and Bessel filters of N = 6 and 10. Note that the extracted coefficients are normalized by the bandwidth parameter B, which can be selected to control the bandwidth of the CROW filter.

The coupling coefficients of Butterworth CROWs are symmetric. At the center of the CROW, the coupling coefficient is about 0.5, which corresponds to a CROW band from $\Delta\omega = -1$ to 1. The coupling coefficients gradually increase toward the two ends of the CROW. This adiabatic transition of the coupling coefficients reduces the reflection at the boundary, and Butterworth CROWs are one of the optimal designs which remove the oscillations in the transmission spectra. Bessel CROWs, which possess maximally flat

Table 2.2. Extraction of coupling coefficients for an *N*=4 Butterworth filter.

$$T(s)=\frac{1}{s^4+2.613s^3+3.414s^2+2.613s+1}=\frac{1}{p_4}$$

$$\Rightarrow\ \left|T(i\omega)\right|^2=\frac{1}{\omega^8+1}\Rightarrow\left|R(i\omega)\right|^2=\frac{\omega^8}{\omega^8+1}$$

$$\Rightarrow R(s)=\frac{s^4}{s^4+2.613s^3+3.414s^2+2.613s+1}=\frac{p_4-\mu_1{}^2p_3}{p_4}$$

$$\Rightarrow p_3=s^3+1.307s^2+s+0.383$$

Divide p_4 by $p_3 \Rightarrow p_2=s^2+1.307s+0.707,\ \frac{1}{\tau_{e1}}=1.307,\ \kappa_1=0.841$

Divide p_3 by $p_2 \Rightarrow p_1=s+1.307,\ \kappa_2=0.541.$

Divide p_2 by $p_1 \Rightarrow \kappa_3=0.841,\ \frac{1}{\tau_{e2}}=1.307$

Table 2.3. Extracted coupling coefficients of Butterworth and Bessel CROW filters

Filter type	$(1/\tau_{e1},\kappa_1,\kappa_2,\cdots,\kappa_{N-1},1/\tau_{e2})/B$
N=6 Butterworth	(1.932, 1.169, 0.605, 0.518, 0.605, 1.169, 1.932)
N=10 Butterworth	(3.196, 1.876, 0.883, 0.630, 0.533, 0.506, 0.533, 0.630, 0.883, 1.876, 3.196)
N=6 Bessel	(2.068, 1.198, 0.393, 0.397, 0.803, 1.486, 2.427)
N=10 Bessel	(3.478, 2.030, 0.932, 0.613, 0.305, 0.333, 0.652, 0.772, 1.056, 2.209, 3.745)

delay, do not have symmetric coupling coefficients. With the proper choice of the zeros of $R(s)$ in nearly symmetric distribution, the coefficients are nearly symmetric.

Fig. 2.6 shows the transmission spectra of Butterworth CROWs with *N* = 6, 10 and 20, respectively. As the order increases, the transmission spectra become flatter in the passband and the roll-off at the band edges is steeper.

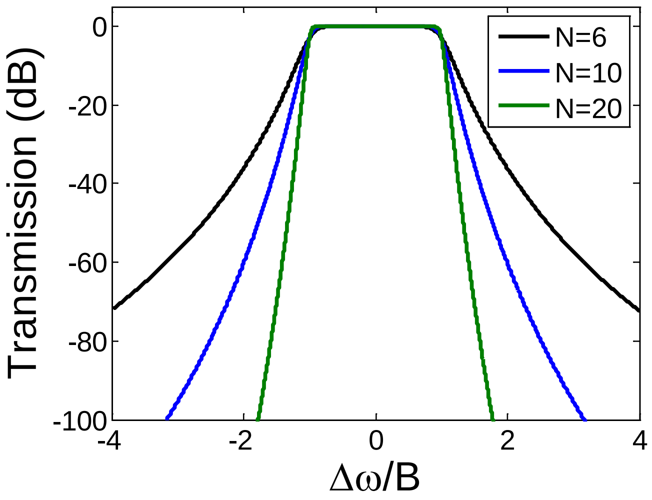

Fig. 2.6. Transmission spectra of Butterworth CROWs with 6, 10, and 20 resonators

2.5 CROWs in the Presence of Loss or Gain

The filter design formalism described above assumes that the resonators are lossless. In practice, there are loss mechanisms, including intrinsic radiation loss of the resonator design, absorption loss of the material, and scattering loss due to imperfection of the fabrication. The modal loss can be modeled with a loss rate of the resonators, $1/\tau_i$, which is related to the quality factor Q of the resonators by $Q=\omega\tau_i/2$. The differential equation of the *k*-th resonator, Eq. (2-7), is rewritten as

$$\frac{da_k}{dt}=(-i\Delta\omega-\frac{1}{\tau_i})a_k-i\kappa_{k-1}a_{k-1}-i\kappa_k a_{k+1}. \tag{2-18}$$

If the loss rates of all the resonators are identical, the coupling matrix in Eq. (2-8) is modified by replacing s with $s+1/\tau_i$. Therefore, for an all-pole filter response $T(s)$ designed for lossless resonators, the transmission in the presence of loss is given by $T'(s)=T(s+1/\tau_i)$, whose poles are shifted to the left by $1/\tau_i$.

Table 2.4. Coupling coefficients of predistorted N=10 Butterworth CROWs.

Resonator loss/gain	$(1/\tau_{e1}, \kappa_1, \kappa_2, \cdots, \kappa_{N-1}, 1/\tau_{e2})\,/\,B$
$1/\tau_i = 0.05B$	(2.597, 1.575, 0.787, 0.637, 0.412, 0.674, 0.467, 0.588, 0.873, 1.912, 3.296)
$1/\tau_i = -0.05B$	(3.403, 1.988, 0.921, 0.635, 0.452, 0.474, 0.605, 0.679, 0.955, 2.044, 3.490)

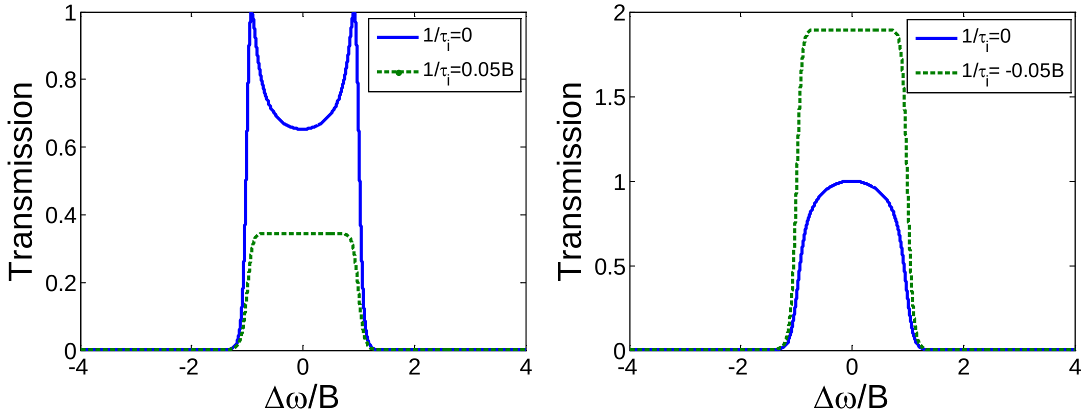

(a) (b)

Fig. 2.7. Transmission spectra of predistorted N=10 Butterworth CROWs with and without loss/gain for (a) $1/\tau_i = 0.05B$ (loss) and (b) $1/\tau_i = -0.05B$ (gain)

To obtain the desired filter response in the presence of loss, we can shift the poles to the right by $1/\tau_i$ in the design to pre-compensate for the left shift due to the loss. This technique is called predistortion of the filters [47]. First, the poles of the desired function $T(s)$ in Eq. (2-11) are shifted to the right by $1/\tau_i$. The constant in the numerator has to be decreased so that the magnitude of the new transfer function $T_0(s)$ is always smaller than or equal to 1. As a result, $T_0(s) = \alpha T(s - 1/\tau_i)$, where α is a constant and is smaller than 1. In the presence of a resonator loss $1/\tau_i$, the transfer function is $T'(s) = T_0(s + 1/\tau_i) = \alpha T(s)$, which is recovered to the same desired response except for an attenuation factor α.

If the CROW is pumped with a uniform gain, the amplifying CROW can be modeled with a negative $1/\tau_i$. The factor α is greater than 1 and is an amplification factor. Table 2.4 lists the predistorted design for N=10 Butterworth CROWs with $1/\tau_i = 0.05B$ (lossy) and $-0.05B$ (amplifying), respectively. Their transmission spectra with and without loss/gain are plotted in Fig. 2.7(a) and Fig. 2.7(b), respectively. Since the group delay is greater at the band edge, frequencies near the band edge experience larger loss and gain. Consequently, the amplitude response is predistorted accordingly before the loss or gain. For Bessel filters, since the group delay is almost constant over the bandwidth, the characteristics of the filters remain the same in the presence of small gain or loss.

2.6 CROW Filters Based on Ring Resonators

A microring CROW consists of a chain of coupled ring resonators (Fig. 2.8(a)). Light is coupled in and out of the CROW via the input and output waveguides. Assuming the coupling region is sufficiently long compared to the wavelength, only light circulating in one direction in the ring is phase-matched to the input and is excited. The coupling between two adjacent rings can be analyzed, using the notation in Fig. 2.8(b), by

$$\begin{bmatrix} c_1 \\ c_2 \end{bmatrix} = \begin{bmatrix} t & i\eta \\ i\eta & t \end{bmatrix} \begin{bmatrix} b_1 \\ b_2 \end{bmatrix}, \tag{2-19}$$

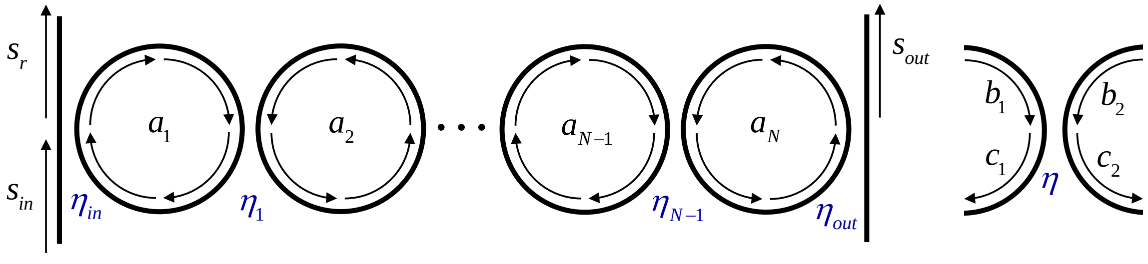

(a) (b)

Fig. 2.8. Schematic drawings of (a) a microring CROW filter and (b) the coupling of two adjacent rings

where η and t are the dimensionless coupling and transmission coefficients over the coupling region, respectively. Assuming the coupling is lossless, $\eta^2 + t^2 = 1$. The transmission and reflection of microring CROWs can be analyzed using transfer matrix formalism [48].

The field coupling coefficient η at the coupling region is related to the time-domain coupling coefficient κ between two rings. In [42], these relations were derived: $\eta = \kappa / f_{FSR}$ for inter-resonator coupling and $\eta_{in,out} = \sqrt{2/(\tau_e f_{FSR})}$ for waveguide-resonator coupling, where $f_{FSR} = v_g / 2\pi R$ is the free spectral range of the ring resonators. However, these formulas are only valid when the coupling is sufficiently weak, because the field inside the ring is not uniform when η is not much smaller than one [33]. In what follows, we describe a method which is valid for any reasonable coupling.

Inter-resonator coupling: Consider two identical resonators coupled to each other with a coupling coefficient κ (Fig. 2.9(a)). The resonant frequencies of the two eigenmodes are $\omega_0 \pm \kappa$. Fig. 2.9(b) illustrates the corresponding case for ring resonators. The field coupling coefficient is η. The fields $b_{1,2}$ and $c_{1,2}$ are related by the coupling (Eq. (2-19)), and propagation along the rings leads to

$$\begin{bmatrix} b_1 \\ b_2 \end{bmatrix} = e^{i\theta(\Delta\omega)} \begin{bmatrix} c_1 \\ c_2 \end{bmatrix}, \tag{2-20}$$

where $\theta(\Delta\omega)$ is the round-trip phase of the rings at $\omega = \omega_0 + \Delta\omega$ and is equal to $-\Delta\omega / f_{FSR}$. Combining Eqs. (2-19) and (2-20), $\exp[-i\theta(\Delta\omega)]$ is equal to the eigenvalue of the coupling matrix in Eq. (2-19), which leads to $\theta(\Delta\omega) = \pm \sin^{-1}\eta$. Therefore, the frequency splitting, which is equal to the coupling coefficient κ, is $\Delta\omega = \pm f_{FSR} \sin^{-1}(\eta)$. As a result,

$$\eta = \sin(\frac{\kappa}{f_{FSR}}). \tag{2-21}$$

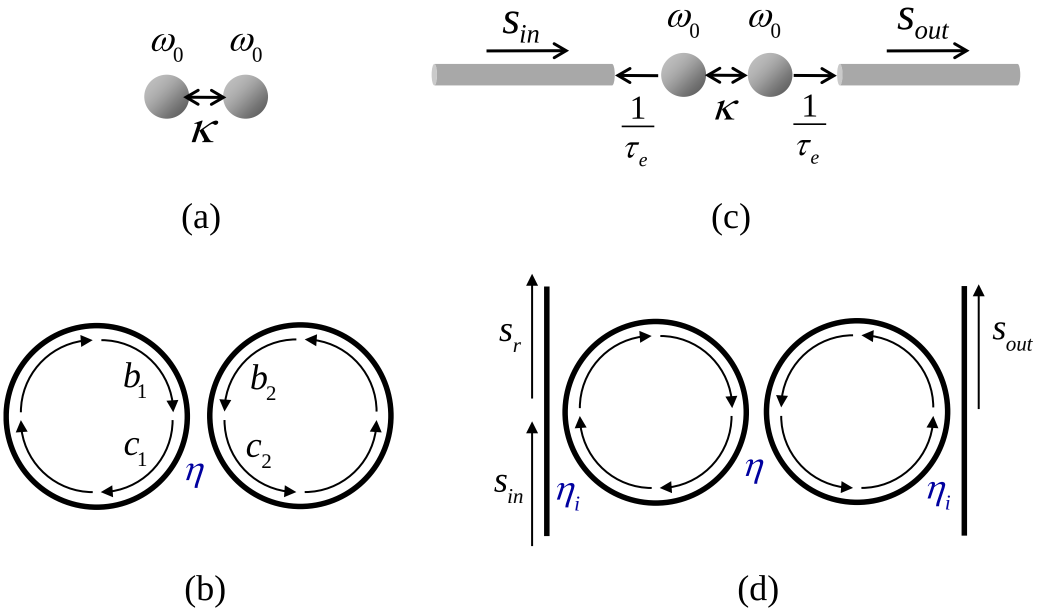

Fig. 2.9. Schematic drawings of the structures for the derivation of (a) inter-resonator coupling and (c) waveguide-resonator coupling. (b,d) The corresponding structures for microring resonators

Waveguide-resonator coupling: In Fig. 2.9(c), the two resonators in Fig. 2.9(a) are both coupled to an output waveguide with an external loss, $1/\tau_e$. Solving the steady-state solution of the coupled-mode equations of the two resonators at $\omega = \omega_0$ leads to amplitude transmission s_{out}/s_{in} given by $(2\kappa/\tau_e)/(1/\tau_e{}^2 + \kappa^2)$, which is equal to one only when the boundary condition $1/\tau_e = \kappa$ is satisfied. We can use this structure to derive the relation between $1/\tau_e$ and the field coupling coefficient of ring resonators. Fig. 2.9(d) illustrates the corresponding structure for ring resonators. The condition that the transmission is unity at $\omega = \omega_0$ can be derived as

$$\eta_i = \sqrt{\frac{2\eta}{1+\eta}}. \tag{2-22}$$

For a given $1/\tau_e$, we first use Eq. (2-21) to find an inter-resonator coupling η which corresponds to a coupling coefficient $\kappa = 1/\tau_e$, and then use Eq. (2-22) to obtain η_i.

Table 2.5. Coupling coefficients of microring CROW filters

Filter type	Bandwidth	$(\eta_{in}, \eta_1, \eta_2, \cdots, \eta_5, \eta_{out})$
N=6 Butterworth	$B = \omega_{FSR} \cdot 0.005$	(0.338, 0.0367, 0.0190, 0.0163, 0.0190, 0.0367, 0.338)
	$B = \omega_{FSR} \cdot 0.05$	(0.852, 0.359, 0.189, 0.162, 0.189, 0.359, 0.852)
N=6 Bessel	$B = \omega_{FSR} \cdot 0.005$	(0.349, 0.0376, 0.0123, 0.0125, 0.0252, 0.0467, 0.376)
	$B = \omega_{FSR} \cdot 0.05$	(0.868, 0.368, 0.123, 0.124, 0.250, 0.450, 0.904)

With Eqs. (2-21) and (2-22), we are ready to convert the coupling coefficients κ in Table 2.3 to the microring couplings η. The only constraint is that κ does not exceed $(\pi/2) f_{FSR}$, or $\omega_{FSR}/4$, which is the maximal coupling which ring resonators with a free spectral range f_{FSR} can achieve (see Eq. (2-21). We consider examples of silicon microring CROWs. The mode index and group index of the silicon waveguides are 2.4 and 4, respectively. The ring radius is 30 μm so that one resonant wavelength is at 1570.8 nm, and the free spectral range f_{FSR} is 398 GHz. The bandwidth of the filters can be chosen by setting the bandwidth parameter B. For example, the bandwidth of Butterworth filters is 2B (Fig. 2.4(a)). If we choose $B = \omega_{FSR} \cdot 0.005$, where $\omega_{FSR} = 2\pi f_{FSR}$, the bandwidth is $2 \cdot 398\ \text{GHz} \cdot 0.005 = 3.98\ \text{GHz}$. The converted η for Butterworth and Bessel filters with $B = \omega_{FSR} \cdot 0.005$ and $B = \omega_{FSR} \cdot 0.05$ are listed in Table 2.5.

The transmission spectra of the microring CROWs in Table 2.5 were calculated using the transfer matrix formalism and were compared with the original transmission spectra calculated from the κ in Table 2.3, calculated using CMT. Fig. 2.10(a) shows the transmission spectra of Butterworth filters with $B = \omega_{FSR} \cdot 0.005$. Since η are sufficiently weak (the largest η is 0.338), the two spectra are nearly identical. Fig. 2.10(b) shows the spectra for $B = \omega_{FSR} \cdot 0.05$, corresponding to stronger coupling. Although there are small passband ripples whose amplitude is about 0.0002, the spectrum closely agrees with the

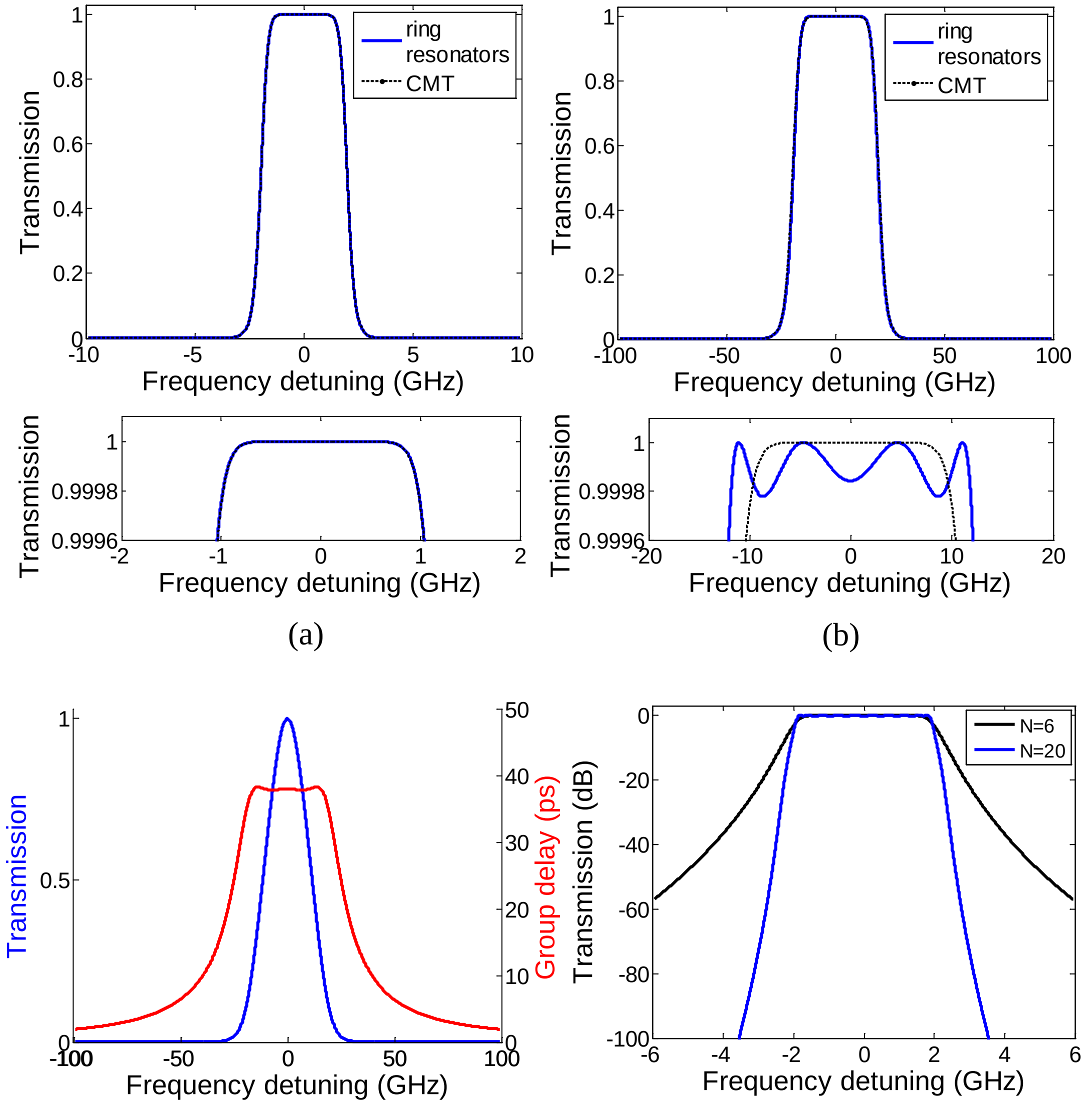

(a)

(b)

(c)

(d)

Fig. 2.10. (a–b) Transmission spectra and their close-ups of microring Butterworth CROWs with (a) $B = \omega_{FSR} \cdot 0.005$ and (b) $B = \omega_{FSR} \cdot 0.05$. (c) Transmission and group delay of an N=6 Bessel microring CROW. (d) Transmission spectra of Butterworth microring CROWs with 6 and 20 resonators respectively

desired response. Therefore, the conversion is valid with η as high as 0.852, whereas the same κ would be converted to η = 1.102 using the formula proposed in [42]. Note that for a bigger bandwidth or higher filter order, κ at the boundary will increase and eventually exceed the upper limit of κ, $(\pi/2)f_{FSR}$. Therefore, resonators with large f_{FSR} are beneficial. However, for ring resonators with small radii, say less than 5 μm, the assumption of the transfer matrix formalism that the coupling region is sufficiently long compared to the wavelength is no long valid, and the coupling of modes will be complicated since modes in the opposite direction will also be excited. In Fig. 2.10(c), we show the spectra of transmission and group delay for an N=6 Bessel CROW with $B = \omega_{FSR} \cdot 0.05$. Fig. 2.10(d) shows the transmission spectra of Butterworth CROWs with 6 and 20 rings.

2.7 Effect of Disorder on CROWs and CROW Filters

The major limitation in the experiment of CROWs has been the unavoidable fabrication imperfection which leads to disorder in the resonant frequencies of individual resonators and the coupling coefficients. The disorder distorts the CROW response, and the yield of CROWs drops as the number of resonators is increased or as the CROW bandwidth is decreased. The effect of disorder on CROWs has been investigated in the literature [49, 50].

In this section we analyze the disorder effect on CROWs. We add random variables to the resonant frequencies and coupling coefficients in the coupled-mode equations (Eq. (2-8)). The deviation of resonant frequencies is modeled as Gaussian-distributed random variables with a standard deviation $\delta\omega$. $\delta\omega$ is the same for all resonators constituting the CROW and does not depend on the coupling coefficients we choose. On the other hand, the standard deviation of coupling coefficients, $\delta\kappa$, is assumed to be proportional to κ, since for the case of evanescent coupling in both ring resonators and grating resonators, κ is an exponential function of the physical dimension (the gap between adjacent rings, the number of holes between adjacent defects). Therefore, we analyze the disorder effect as a function of $\delta\kappa/\kappa$. Since both the coupling coefficients and the frequency detuning are normalized with the bandwidth parameter *B* in Eq. (2-8), the disorder effect depends on $\delta\omega / B$ and $\delta\kappa / B$. Therefore, the effect of disorder in resonant frequencies is bandwidth-dependent. The larger *B* we choose, the smaller the disorder effect is. On the other hand, the effect of disorder in coupling coefficients does not depend on *B*, since $\delta\kappa$

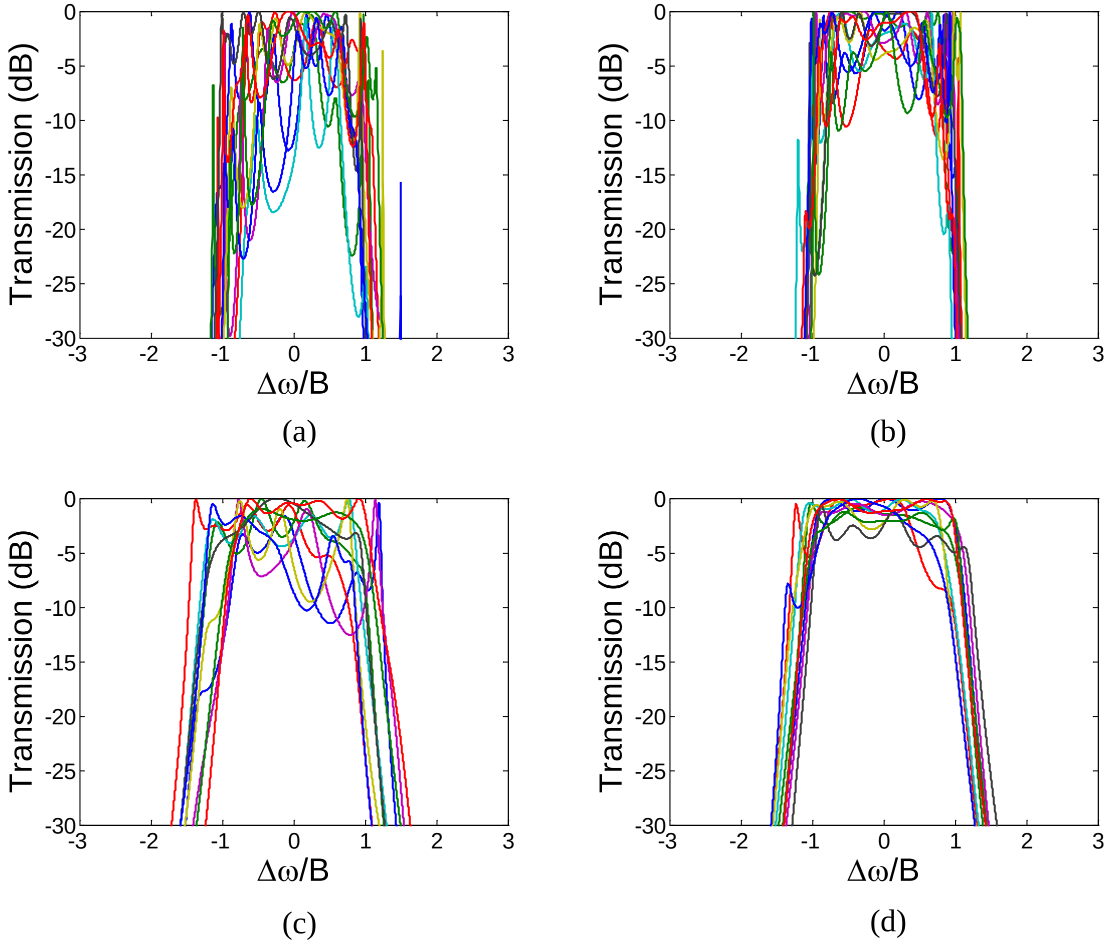

(a)

(b)

(c)

(d)

Fig. 2.11. Simulated transmission spectra of 10-resonator CROWs with disorder in resonant frequencies. (a,b) Uniform coupling coefficients. (c,d) Butterworth filters. (a,c) $\delta\omega = 0.4B$. (b,d) $\delta\omega = 0.2B$

is proportional to κ and thus proportion to *B*.

Fig. 2.11(a) and Fig. 2.11(b) show the simulated transmission spectra of *N*=10 CROWs with uniform coupling coefficient and with $\delta\omega$ equal to 0.4*B* and 0.2*B*, respectively. The disorder leads to oscillations in the passband. Fig. 2.11(c) and Fig. 2.11(d) show the transmission spectra of *N*=10 Butterworth CROWs. The oscillation amplitudes of Butterworth CROWs are smaller than those of uniform CROWs. Therefore, we found that Butterworth CROWs exhibit better tolerance against disorder in resonant frequencies. Disorder in a CROW is a perturbation to an ideal CROW and can be taken as scatterers in a waveguide. For CROWs with uniform coupling coefficient, the boundaries between the CROW and the waveguides cause reflection and form a cavity. Disorder in uniform CROWs can be thought of as scatterers in a cavity which can cause multiple cavities and thus larger oscillations. For a Butterworth CROW, the coupling coefficients are tailored to adiabatically transform between the CROW and the waveguides, thereby removing the cavity and reducing the amplitude of oscillations.

To quantify the disorder loss, we take the average of the transmission over the center half of the CROW band. Fig. 2.12(a) shows the disorder loss as a function of $\delta\omega / B$ for *N*=10 CROWs with uniform coupling coefficients and Butterworth filter design, respectively. The disorder loss of Butterworth CROWs is approximately 60% of the disorder loss of uniform CROWs. Fig. 2.12(b) shows the disorder loss for disorder in coupling coefficients, where the disorder loss of Butterworth CROWs does not differ from the disorder loss of uniform CROWs. The reason is that the coupling coefficients at the end of Butterworth CROWs are large, leading to larger $\delta\kappa$. Therefore, Butterworth filters are more robust only in the case of disorder in resonant frequencies.

Fig. 2.12(c) shows the disorder losses as functions of *N* for CROWs with $\delta\omega / B = 0.2$ and $\delta\kappa/\kappa = 0.2$, respectively, and for the two kinds of CROWs. As the number of resonator increases, the increase of losses is approximately linear. As we couple more resonators, the disorder loss increases and the yield of CROWs drops. At some N, the loss becomes too large that the CROWs are no longer useful. Therefore, we define the maximum number of resonators, $N_{\max}$, as the maximum N with disorder loss smaller than 5 dB. With $N_{\max}$, we can determine the maximum achievable group delay, which is proportional to $N_{\max}/B$. Fig. 2.12(d) shows the maximum delay versus the bandwidth of the CROWs. For disorder in resonant frequency $\delta\omega$, $N_{\max}$ increases with the bandwdidth, and the resulting maximum delay increases with the bandwidth. On the other hand, the effect of disorder in coupling coefficients is bandwidth-independent, so $N_{\max}$ is constant and the maximum delay is inversely proportional to the bandwidth. The curves for the two kinds of disorder are shown respectively, and the green curve shows the maximum group delay in the presence of both disorders. The achievable delay is maximum when the two disorder effects are equally strong and is flat over a wide range of bandwidth. In conclusion, in the presence of disorder, the achievable delay of CROWs has an upper limit, no matter how we choose the bandwidth.

2.8 Summary

In this Chapter, we demonstrated a formalism for deriving the coupling coefficients of CROWs to achieve desired filter responses such as maximally flat transmission (Butterworth filters) and maximally flat group delay (Bessel filters). The formalism is based on CMT and the recursive relations of the coupling matrix to extract the coupling coefficients. Compared to TMM, the design using CMT is simpler since the field in each resonator is represented by only one variable. The universal coupling coefficients can be applied to any type of resonators or even the coupling of different types of resonators. The bandwidth of the filters can be changed easily by selecting the bandwidth parameter

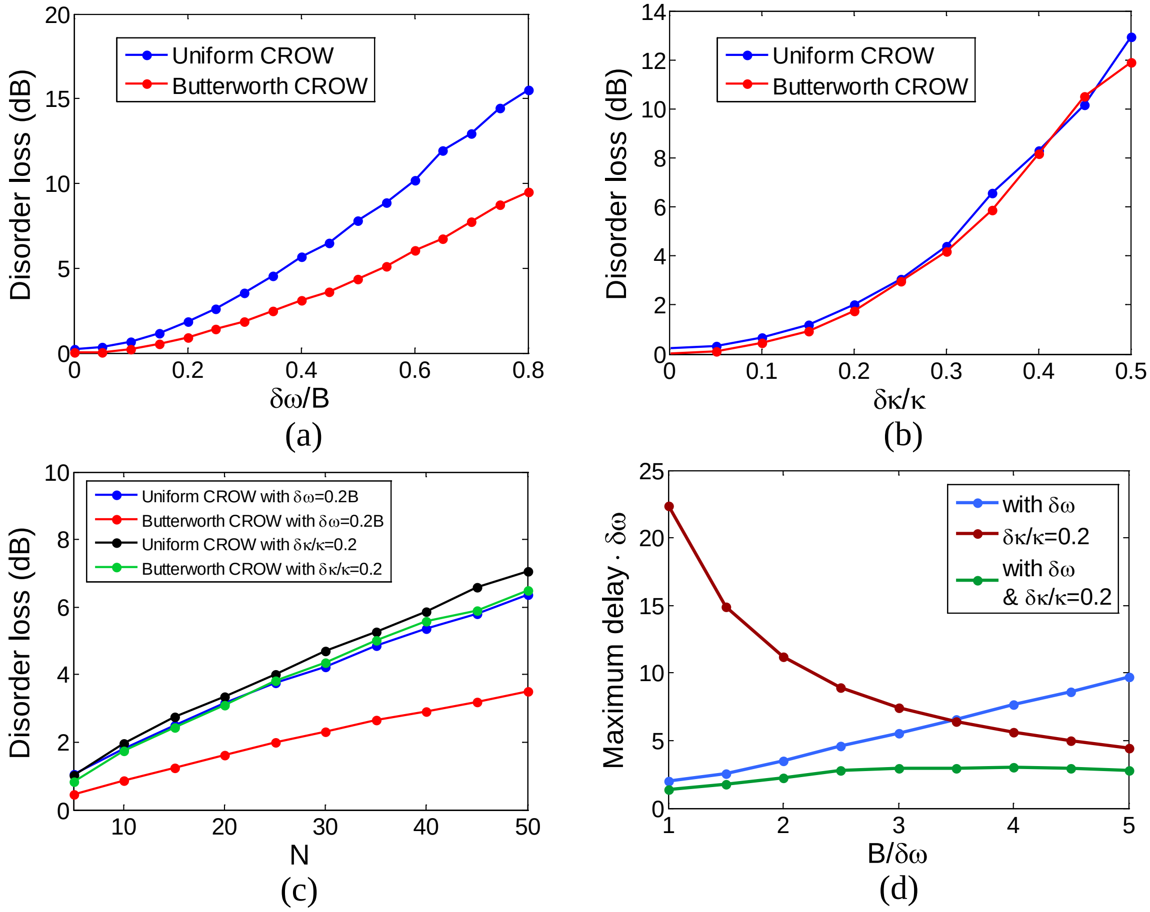

Fig. 2.12. Disorder loss of *N*=10 uniform CROWs and *N*=10 Butterworth CROWs for disorder in (a) resonant frequencies and (b) coupling coefficients. (c) Disorder loss versus *N* for uniform CROWs and Butterworth CROWs and for disorder in resonant frequencies and coupling coefficients, respectively. (d) Maximum achievable delay versus the bandwidth of CROWs

B. Furthermore, predistortion techniques can be applied for the design of lossy or amplifying CROW filters.

The disadvantage of CMT is that it assumes weak coupling between the resonators and that the field distribution in each resonator remains unchanged. It is less accurate than TMM, which directly analyzes the fields inside the resonators. The time-domain coupling coefficients of CMT have to be converted to the parameters of the type of resonators comprising the CROWs. We have demonstrated the conversion to the field coupling coefficients for microring resonators and the lengths of grating sections for grating defect resonators. The formulas for the conversion are valid for any reasonable coupling.

In the disorder analysis we simulated the disorder loss and showed it as a function of deviation in the resonant frequency, deviation in the coupling coefficient, and the number of resonators. We showed that Butterworth CROWs are more robust against disorder in resonant frequencies compared to CROWs with uniform coupling coefficients. For a given type of resonators and a given fabrication technology, an estimate of $\delta\omega$ and $\delta\kappa/\kappa$ will be useful in determining the practical bandwidth, number of resonators, and the achievable delay.

Chapter 3

"Ideal" Optical Delay Lines

3.1 Introduction

An "ideal" optical delay line is capable of delaying an optical signal without any distortion. It should possess constant transmission and constant group delay over a prescribed bandwidth. The original proposal of CROWs [26] was based on uniform coupling coefficient κ which leads to a dispersion curve and a group velocity dictated by the coupling coefficient. If the coupling coefficients are allowed to vary along the CROW, the dispersive properties can be further optimized. In Chapter 2, we described a filter design formalism for deriving the coupling coefficients which satisfy a desired filter response. The formalism results the design of Butterworth and Bessel CROWs which exhibit maximally-flat transmission and group delay respectively. However, constant amplitude and group delay cannot be achieved by any one of these filters simultaneously, since the amplitude and the phase of all-pole functions are related to each other.

Therefore, designing a CROW which satisfies the criterion of an "ideal" delay line is the ultimate goal of the CROW theory. In this chapter, we present an ideal delay line based on the reflection of a CROW, whose coupling coefficients are tailored to realize an all-pass Bessel filter. The design of all-pass Bessel filters has been explored using microwave equivalent circuit methods [43]. In what follows, we utilize the formalism in Chapter 2 to design the reflection CROWs and interpret the physics behind the idea.

3.2 All-Pass Filters Based on the Reflection of CROWs

As shown in Chapter 2, the transfer function of an N-resonator transmitting CROW is an all-pole function $T(s)=k/p(s)$, where $p(s)$ is an N-th-order polynomial . An all-pass function $[p(s)]^*/p(s)$ possesses a constant amplitude of one and a phase which is twice the phase of $T(s)$. As a result, an all-pass Bessel filter whose $p(s)$ is a Bessel polynomial possesses constant amplitude and maximally flat group delay over a prescribed bandwidth, as shown in Fig. 3.1. The higher-order dispersion is zero up to the order of N. As shown in Eq. (2-13b), the numerator of the reflection $R(s)$ of a CROW is given by $p_N-\mu_1{}^2 p_{N-1}$, which is a polynomial in s with a leading term s^N. Equating $p_N-\mu_1{}^2 p_{N-1}$ with $p_N{}^*$ can lead to an all-pass function.

We consider a 6th-order all-pass Bessel filter as an example. $p(s)=s^6+4.495s^5+9.622s^4+12.358s^3+9.92s^2+4.672s+1$ is a Bessel polynomial. Comparing $[p(s)]^*/p(s)$ with $R(s)$ in Eq. (2-13b) leads to $p_6=p(s)$ and $p_6-\mu_1{}^2 p_5=[p(s)]^*$. Since the coefficients of $p(s)$ are all real, $[p(s)]^*=p(-s)$. Therefore, $\mu_1{}^2 p_5=p(s)-p(-s)$, which leads to $p_5=s^5+2.749s^3+1.039s$ and $\mu_1{}^2=8.990$. With p_6 and p_5, all the coupling coefficients can be extracted step by step, using Eq. (2-12).

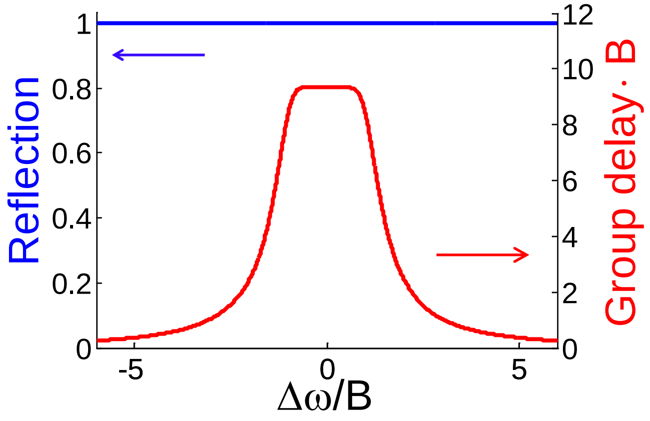

Fig. 3.1. Spectra of reflection and group delay of an all-pass Bessel filter

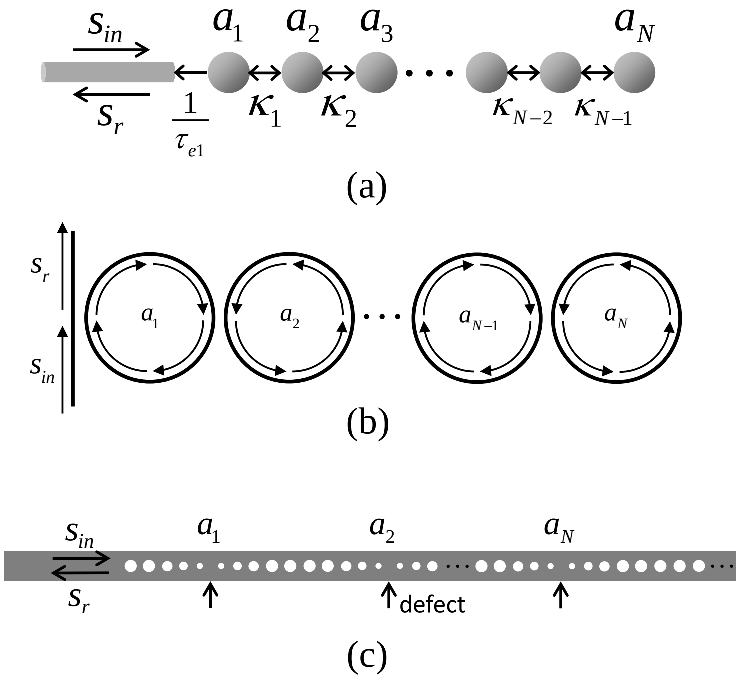

Fig. 3.2. Schematic drawings of (a) a reflecting CROW filter, (b) a reflecting microring CROW, and (c) a reflecting grating-defect CROW

The extracted coefficients are $(1/\tau_{e1}, \kappa_1, \kappa_2, \kappa_3, \kappa_4, \kappa_5, 1/\tau_{e1}) =$ (4.495, 2.622, 1.207, 0.824, 0.632, 0.463, 0), which decrease monotonically from the input. Finally, we multiply the coefficients by a bandwidth parameter B to choose the bandwidth, which leads to maximally flat delay between $\Delta\omega = -B$ and B. The group delay is inversely proportional to B. The spectra of reflection and group delay are shown in Fig. 3.1. Note that the extraction procedure always leads to $1/\tau_{e2} = 0$. From the conservation of energy, since the reflected power $|R(j\omega)|^2$ is one for all frequencies, the transmitted power has to be zero. In other words, there is no coupling to the output waveguide. The input energy coupling into the CROW is eventually coupled back to the input waveguide.

Fig. 3.2(a) shows a reflecting CROW filter. Like transmitting CROWs shown in Chapter 2, reflecting CROWs can be realized with various types of resonators, as shown in Fig. 3.2(b) and Fig. 3.2(c). The output s_r is at the through port of microring CROWs and at the reflection of grating CROWs.

To understand the physics behind reflecting Bessel CROWs, we plot a CROW propagation band as a function of distance. CROWs with uniform coupling coefficient κ form a constant-height band between $\omega_0 - 2\kappa$ and $\omega_0 + 2\kappa$. Frequencies within the CROW band propagate freely while those outside evanesce exponentially with distance.

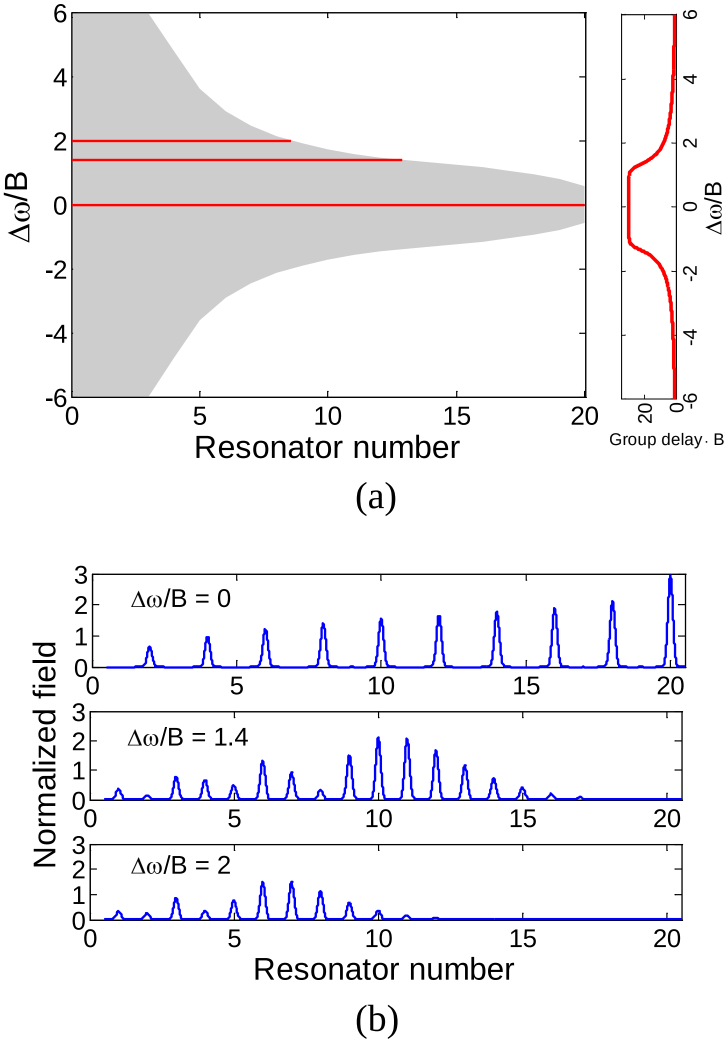

Fig. 3.3. (a) (left) CROW propagation band as a function of distance of an N=20 reflecting Bessel CROW. Red lines: Propagation distance for $\Delta\omega/B$ = 0, 1.4, and 2. (right) Group delay spectrum. (b) Field distribution along the CROW for $\Delta\omega/B$ = 0, 1.4, and 2

CROWs with tailored coupling coefficients correspond to a distance-dependent CROW band whose thickness is $4\kappa(z)$, where $\kappa(z)$ is the local coupling coefficient. Fig. 3.3(a) shows the modulated CROW band of an N=20 reflecting Bessel CROW, whose bandwidth decreases monotonically from the input. An input signal at a given frequency propagates into the CROW until it reaches the band edge where it is reflected back. The red lines in Fig. 3.3(a) indicate the propagating distances at $\Delta\omega/B$= 0, 1.4, and 2. Fig. 3.3(b) plots the field distribution at these frequencies. At $\Delta\omega$=0, light propagates to the last resonator. As the frequency moves away from the resonant frequency, the propagating distance decreases. The dependence of the propagating distance on frequency compensates for the group velocity dispersion of CROWs, whose group delay increases monotonically from the band center to the band edge, and results in a constant group delay.

3.3 Reflecting Bessel CROWs Based on Ring Resonators

To realize reflecting Bessel CROWs in ring resonators, we convert the time-domain coupling coefficients to the field coupling coefficients in the coupling regions. The conversion is based on the formalism in Section 2.6 . We consider silicon ring resonators as an example. The mode index and group index of the Si waveguides are 2.4 and 4, respectively. The radii of the rings are selected as 20 μm so that one resonant wavelength is 1570.8 nm and the free spectral range f_{FSR} is 597 GHz. We choose $B=\omega_{FSR}\cdot 0.003$ and $B=\omega_{FSR}\cdot 0.03$, which lead to field coupling coefficients of (0.395, 0.0494, 0.0228, 0.0155, 0.0119, 0.0087) and (0.926, 0.474, 0.226, 0.155, 0.119, 0.087), respectively. The spectra of reflection and group delay are shown in Fig. 3.5(a) and Fig. 3.5(b). The spectra are ideal for weaker coupling coefficients when $B=\omega_{FSR}\cdot 0.003$. For the case of $B=\omega_{FSR}\cdot 0.03$,

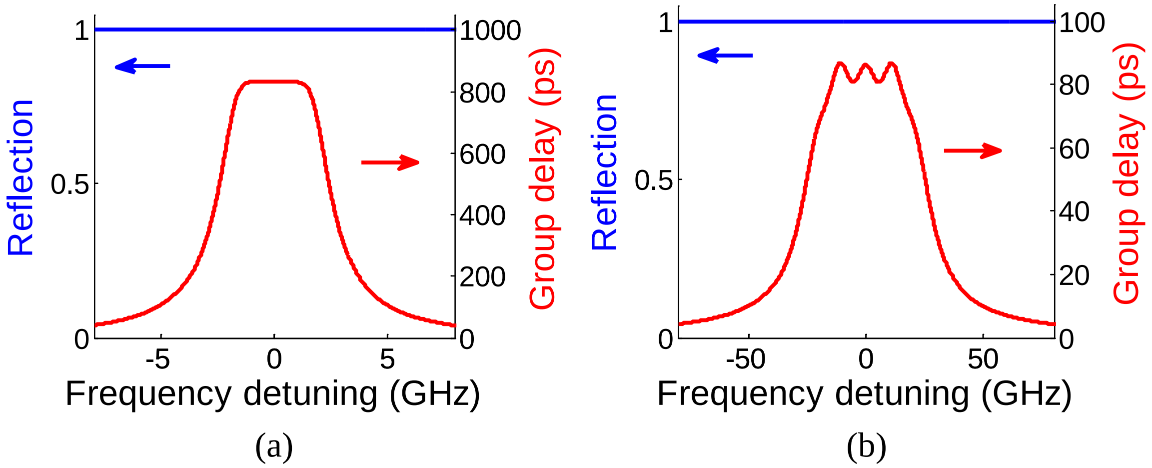

Fig. 3.4. Spectra of reflection and group delay of N=6 reflecting Bessel CROWs based on ring resonators. (a) $B = \omega_{FSR} \cdot 0.003$. (b) $B = \omega_{FSR} \cdot 0.03$

there are oscillations in the group delay spectrum since the coupling coefficient at the input is close to the maximal coupling coefficient of the ring resonators, $\omega_{FSR}/4$.

3.4 Properties of Reflecting Bessel CROWs

3.4.1 Reflecting Bessel CROWs in the Presence of Loss or Gain

Up to this point we have considered only lossless resonators. For lossy resonators with constant loss rates, the total loss is proportional to the group delay. Since the group delay is flat, the loss is also flat within the bandwidth, and the definition of ideal delay lines is still satisfied. Fig. 3.5(a) shows the spectra of the same microring CROW in Fig. 3.4(a) with a propagation loss of 1 dB/cm. On the other hand, if the resonators are pumped with uniform gain, the amplification is proportional to the group delay and is also flat, as shown in Fig. 3.5(d). The enhanced reflection gain by slow light results in efficient and dispersion-less amplifiers.

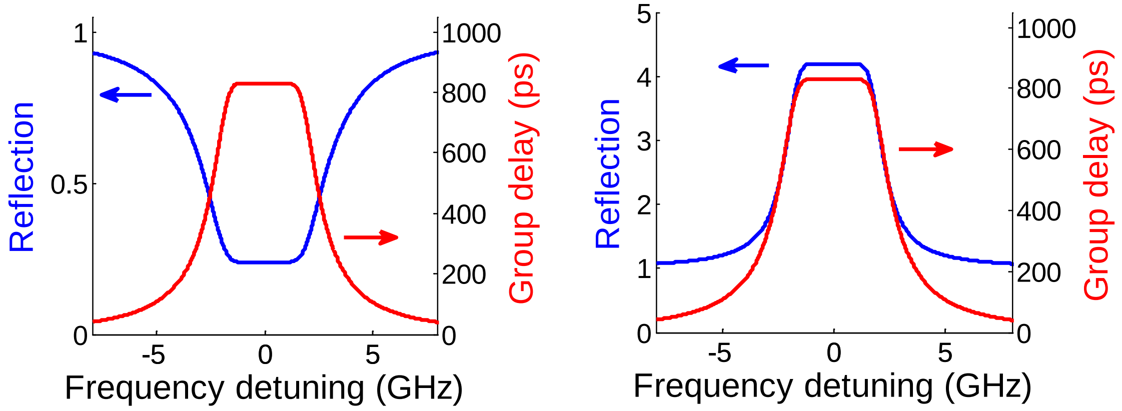

(a) (b)

Fig. 3.5. Spectra of reflection and group delay of *N*=6 reflecting microring Bessel CROWs with (a) uniform loss and (b) uniform gain of 1 dB/cm

3.4.2 Delay-Bandwidth Product of Reflecting CROWs

One important parameter of optical delay lines is the delay-bandwidth product (DBP), $\Delta f\cdot\tau$, which represents the number of bits that can be stored. The group delay τ is equal to $-d\phi/d\omega$, where ϕ is the phase of the transfer function. Therefore, assuming ω_1 and ω_2 are the starting and ending frequencies of the bandwidth,

$$\Delta\omega\cdot\tau=(\omega_2-\omega_1)\cdot\frac{d\phi}{d\omega}\approx\int_{\omega_1}^{\omega_2}\frac{d\phi}{d\omega}d\omega=\phi(\omega_2)-\phi(\omega_1), \qquad (3\text{-}1)$$

provided that τ varies very little over the bandwidth. For coupled-resonator structures, the DBP that can be provided by each resonator has an upper bound. For transmitting CROWs, each resonator provides a pole to the transfer function, leading to a phase shift of π across the resonance. From Eq. (3-1), $\Delta\omega\cdot\tau$ is smaller than π for each resonator in a transmitting CROW. Therefore, the upper bound of $\Delta f\cdot\tau$ is $0.5N$ for transmitting CROWs, where N is the number of resonators. Reflecting CROWs, on the other hand, possess both poles and zeros. Each resonator contributes a pole and a zero to the transfer function, and the upper bound of $\Delta f\cdot\tau$ is N for reflecting CROWs. Since light takes a round trip in a reflecting CROW, the larger DBP of reflecting CROWs makes sense.

The DBP of reflecting Bessel CROWs is approximately 0.5 per resonator, as can be evaluated in Fig. 3.1, Fig. 3.3(a), and Fig. 3.5. Therefore, the DBP per resonator of reflecting Bessel CROWs is larger than that of any kind of transmitting CROW. For example, the DBP per resonator of a transmitting CROW with uniform coupling coefficient is $1/\pi$, considering the center half of the CROW band as the bandwidth.

3.4.3 Effect of Disorder on Reflecting Bessel CROWs

Although the delay capability of reflecting CROWs is larger, reflecting CROWs are more sensitive to fabrication disorder of coupling coefficients and resonant frequencies. Any imperfection in a reflecting CROW scatters light twice as it takes a round trip. The cavity between the imperfection and the end of the CROW causes Fabry-Perot-type oscillations, as shown in Fig. 3.6(a). Fig. 3.6(b) shows the spectra of 10 different N=10 reflecting Bessel CROWs under disorder of coupling coefficients. The modified coupling coefficients are given by $\kappa_i' = r_i \kappa_i$, where r_i is a Gaussian-distributed random variable with a standard deviation of 0.03. The effect of disorder in resonant frequencies is similar. Under disorder, the average of the delay spectra is still optimally flat among all kinds of

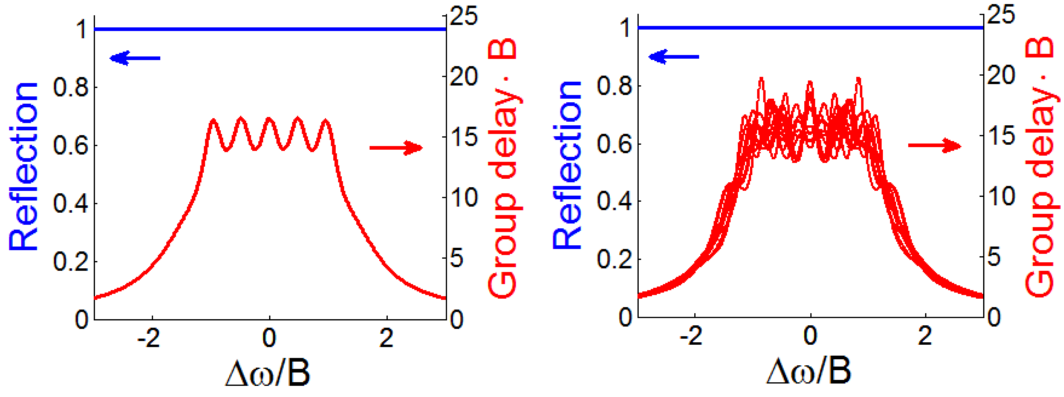

(a) (b)

Fig. 3.6. Spectra of reflection and group delay of N=10 reflecting Bessel CROWs with disorder of coupling coefficients. (a) $\kappa_4' = 1.05\kappa_4$. (b) $\kappa_i' = r_i \kappa_i$ for all i

reflecting CROWs.

Chapter 4

Designing CROWs Based on High-Q Grating-Defect Resonators

4.1 Introduction

CROWs can be realized with various types of resonators, such as microrings [7, 20, 21, 24], photonic crystal resonators [9, 19], and waveguide-grating resonators [22, 28]. While CROWs are most commonly based on ring resonators, CROWs based on waveguide-grating resonators are attractive for their natural implementation in waveguides. Grating structures are defined on waveguides to change the group velocity of light, requiring no additional design for the coupling between waveguides and CROWs. The building block of grating CROWs is a grating resonator. One type of grating resonators is a defect resonator where an artificial defect is introduced in a waveguide grating. The defect cavity supports a mode with a resonant frequency inside the grating band gap. The modal field is centered at the defect and evanesces exponentially in the grating. A grating CROW consists of a sequence of defects where adjacent resonators couple to each other via the evanescent field in the intervening grating. The coupling strength depends on the product of the grating strength and the spacing between adjacent defects. Grating CROWs based on the approximation of weak gratings can be analyzed with coupled-mode equations where two counter-propagating modes are connected by the grating [28].

When the grating is strong, such as periodic air holes in a silicon waveguide, the length of each grating-defect resonator can be as short as a few microns. High density of resonators is important for optical buffers since the delay-bandwidth product is proportional to the number of resonators. CROWs based on such small resonators have been experimentally demonstrated in silicon waveguides [22]. However, the major limitation was the intrinsic propagation loss due to radiation [36]. Highly confined modes lead to large spatial Fourier components which are phase-matched with the lossy radiation modes. The resulting low quality factor of the resonators (Q<1000) leads to power decay time constant of approximately 1 picosecond, limiting applications such as optical delay lines. Because of the coupling to the higher-order (radiation) modes, coupled-mode equations which consider only forward and backward guided modes are no longer valid. Consequently, the design of grating resonators based on strong gratings usually relies on three-dimensional simulation of the entire structures.

In this Chapter, we reduce the propagation loss of grating-defect CROWs by designing high-Q grating-defect resonators as the building blocks. High-Q grating resonators have been demonstrated both theoretically and experimentally. Two major approaches are respectively based on tapering the grating near the defect [51, 52] and spatially modulating the grating (period or hole radius) without a physical defect section [53, 54]. Both approaches aim to define a smooth modal field. Gaussian field distributions are well-known functions which greatly reduce the coupling to radiation modes [54, 55]. We present a systematic design of high-Q tapered grating-defect resonators where 4 or 6 periods on each side of the defect are tapered. We start with a numerical characterization of gratings with different hole radii. For a given taper profile, we can determine the modal field based on the calculated grating strength as a function of hole radius and perform spatial Fourier transform of the mode. We determine the optimal taper profile which minimizes the coupling to radiation modes and confirm the results with numerical simulation of quality factor.

When CROWs are based on high-Q resonators, the coupling to radiation modes is negligible, so the coupled-mode equations are valid. In Section 4.2 , We present a coupled-mode formalism for the analysis and design of grating-defect resonators and CROWs. We show systematic design of high-Q tapered resonators in Section 4.3 and demonstrate the control of inter-resonator coupling for CROWs in Section 4.4 Filter design based on tailoring the coupling coefficients along a CROW is shown in Section 0. The coupling coefficients derived in Chapter 2 are converted to the numbers of holes between adjacent defects. Filter design not only optimizes the transmission and dispersive properties of CROWs but also improves the tolerance of CROWs against fabrication disorder, as will be discussed in Section 6. Finally, it is worth mentioning that we design the resonators and CROWs to resonate at the Bragg wavelength of the grating in order to ensure that the resonant wavelength will not change with the number of holes. If the resonant wavelength is not at the Bragg wavelength, especially near the band edge, an extra phase section will be required when cascading resonators for CROWs.

4.2 Coupled-Mode Formalism for Grating-Defect CROWs

A Bragg grating is a periodic perturbation to a waveguide. A grating with a period Λ couples counter-propagating modes with a propagation constant β if the phase-matching condition is satisfied, i.e., $2\pi/\Lambda = 2\beta$. The coupled-mode equations relating the amplitudes of the forward mode a and the backward mode b are given by [56]

$$\begin{aligned}\frac{da}{dz} &= -i\delta a + i\kappa_g{}^*(z)b \\ \frac{db}{dz} &= i\delta b - i\kappa_g(z)a\end{aligned}, \qquad (4\text{-}1)$$

where $\delta \equiv \beta - \beta_B$ is the detuning from the Bragg condition, $\beta_B \equiv \pi/\Lambda$, and $\kappa_g(z)$ is the coupling coefficient of the grating. The absolute value and phase of $\kappa_g(z)$ represent the strength and phase of the grating respectively. $\kappa_g(z)$ is a constant for a uniform grating. If the grating strength is tapered, $|\kappa_g(z)|$ varies along the grating. For a grating structure distributed between $z=0$ and $z=L_g$ and an input $a(0)=1$ from $z=-\infty$, the general approach of solving the transmission and the field distribution is as follows: (i) Set the boundary condition at the output as $a(L_g)=1$ and $b(L_g)=0$ (no input from $z=\infty$). (ii) Propagate a and b from $z=L_g$ back to $z=0$ analytically or numerically, using Eq. (1). (iii) Divide the resulting $a(z)$ and $b(z)$ by $a(0)$ to recover the input amplitude $a(0)=1$.

A grating-defect resonator is formed by inserting an artificial defect section in a

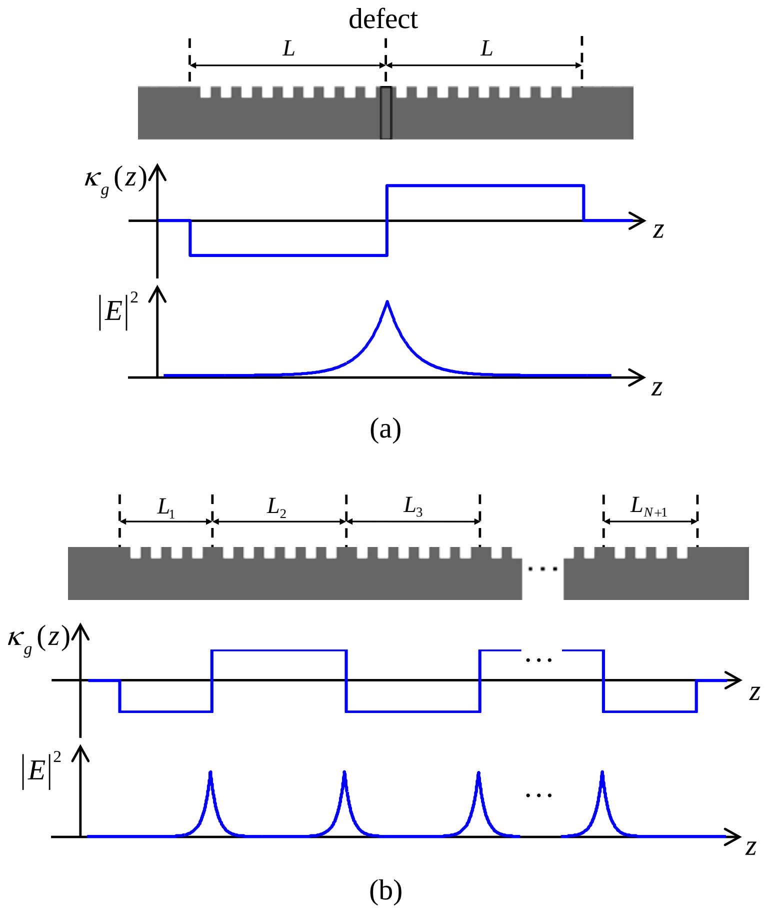

Fig. 4.1. Schematic drawings, coupling coefficients, and field intensity of (a) a grating-defect resonator and (b) a grating-defect CROW

grating, as shown in Fig. 4.1(a). The defect section is a cavity where light is longitudinally confined by the Bragg gratings at frequencies inside the band gap ($|\delta|<\kappa_g$). If the defect length is $\lambda/(4n)$ (a quarter-wave-shifted (QWS) defect; n is the effective index of the waveguide mode), the phase of $\kappa_g(z)$ is shifted by π, and the defect mode resonates at the Bragg frequency (δ=0). The distribution of the modal energy, $|a|^2+|b|^2$, is centered at the defect and evanesces exponentially in the grating, as shown in Fig. 4.1(a). The modal fields (a and b) are proportional to $\exp(-\kappa_g\Delta z)$, where Δz is the distance from the defect.

A grating-defect CROW consists of a sequence of defects, where adjacent defect modes interact with each other via their evanescent fields, as shown in Fig. 4.1(b). $\kappa_g(z)$ alternates between κ_g and $-\kappa_g$. The inter-resonator coupling is determined by the spacing between defects, denoted as L. For a grating structure consisting of only QWS defects (i.e. a real $\kappa_g(z)$), the field distribution at δ=0 for an input $a(0)$=1 can be derived as

$$a(z)=a(L_g)\cosh\left(\int_z^{L_g}\kappa_g(z')dz'\right) \tag{4-2a}$$

and

$$b(z)=-ia(L_g)\sinh\left(\int_z^{L_g}\kappa_g(z')dz'\right), \tag{4-2b}$$

where $a(L_g)=1\Big/\cosh\left(\int_0^{L_g}\kappa_g(z')dz'\right)$ is the transmitted amplitude. Since the sign of $\kappa_g(z)$ alternates along the grating, both $a(z)$ and $b(z)$ alternate between exponential growing and exponential decay. We consider an inter-defect spacing L and $L_1=L_{N+1}=L/2$ at the boundary, which guarantees $\cosh\left(\int_0^{L_g}\kappa_g(z')dz'\right)=1$ and thus unity transmission $a(L_g)$=1. The energy stored in the grating, $E_{stored}=\int_0^{L_g}(|a|^2+|b|^2)dz/v_g$, can be derived as $L_g\left[\sinh(\kappa_g L)/\kappa_g L\right]/v_g$, where v_g is the group velocity of the waveguide mode. Since the input power $|a(0)|^2$ is 1, the group velocity in the grating-defect CROW is given by

$$v_{g,CROW}=\frac{L_g}{E_{stored}}=v_g\cdot\frac{\kappa_g L}{\sinh(\kappa_g L)}. \tag{4-3}$$

The slowing factor is a function of $\kappa_g L$.

The inter-resonator coupling and waveguide-resonator coupling for grating-defect resonators can be derived the same way as in Section 2.6 Fig. 4.2 shows the grating structures which corresponds to the structures in Fig. 2.9. The inter-resonator coupling κ can be obtained from the splitting of resonance in two coupled resonators (Fig. 4.2(a)). It can be shown that under the assumption of $\exp(-\kappa_g L) \ll 1$, the splitting is given by $\Delta\omega = \pm\kappa_g v_g \exp(-\kappa_g L)$, where v_g is the group velocity of the waveguide mode. Therefore,

$$\kappa = \kappa_g v_g \exp(-\kappa_g L). \tag{4-4}$$

The group velocity of CROWs at resonant frequency is thus $v_{g,CROW} = 2\kappa L = v_g \left[2\kappa_g L / \exp(\kappa_g L) \right]$, which, in the limit of $\exp(-\kappa_g L) \ll 1$, is the same

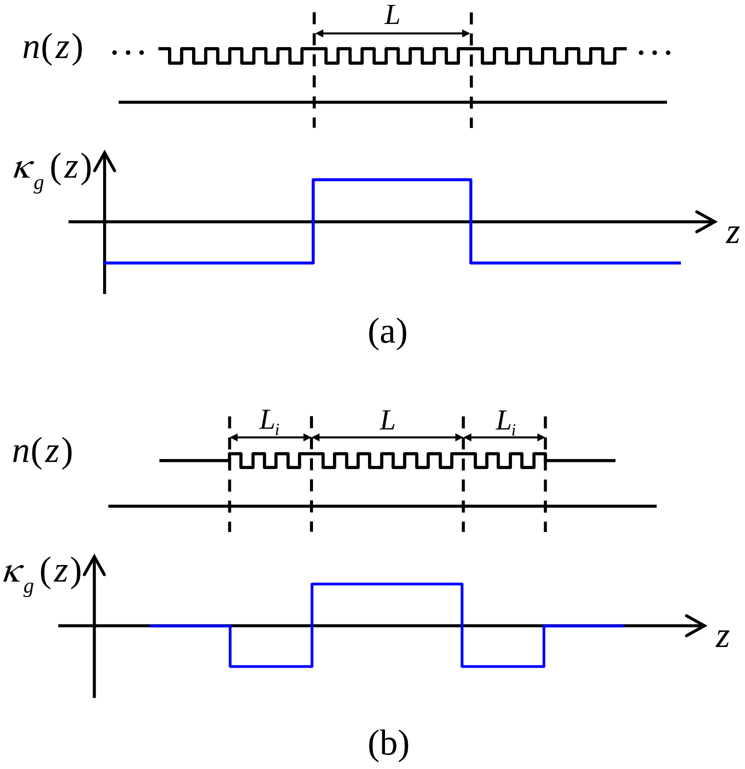

Fig. 4.2. Distribution of refractive index and coupling coefficient for (a) two coupled defect resonators and (b) two coupled defect resonators with external coupling to the waveguides

as Eq. (4-3). The external loss $1/\tau_e$ from the end resonator into the waveguide is a function of grating length as well and can be derived using the structure in Fig. 4.2(b). At the Bragg wavelength, the condition that the transmission is unity is $L_i = L/2$. According to the formalism described in Section 2.6 ,

$$\frac{1}{\tau_e} = \kappa_g v_g \exp(-2\kappa_g L_i). \tag{4-5}$$

For a single grating-defect resonator shown in Fig. 4.1(a), the total loss rate is $1/\tau = 2/\tau_e$, and the quality factor of the resonator is

$$Q = \frac{1}{2}\omega\tau = \frac{\omega \cdot \exp(2\kappa_g L)}{4\kappa_g v_g}. \tag{4-6}$$

Q is an exponential function of L.

Fig. 4.3(a) and Fig. 4.3(b) show the spectra of transmission and group delay of 10-resonator grating-defect CROWs with L=200 μm and L=300 μm, respectively, calculated with the coupled-mode equations in Eq. (4-1). We choose a group index of 4 and a weak grating with κ_g=0.01/μm. The lengths of the first and last grating sections, L_1 and L_{N+1}, are chosen to be L/2 to match the CROW section to the waveguides. According to Eq.

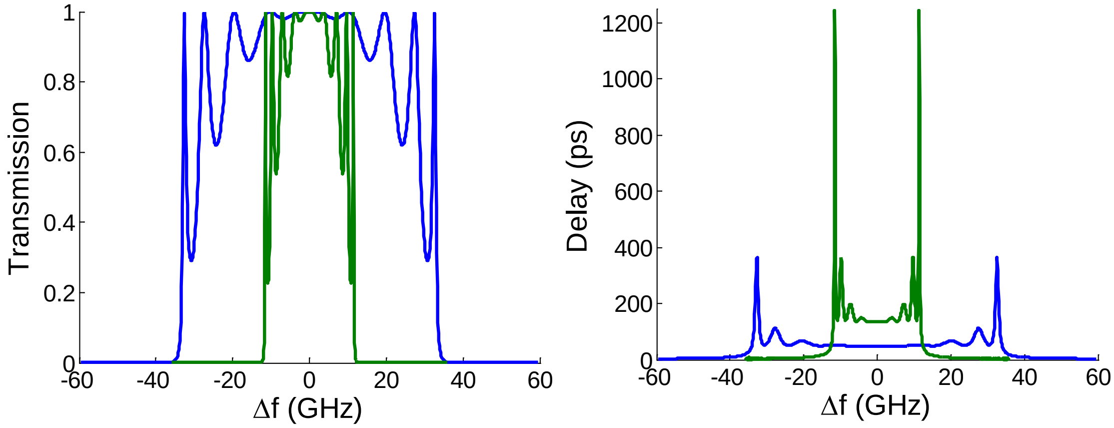

(a) (b)

Fig. 4.3. Spectra of (a) transmission and (b) group delay of N=10 grating-defect CROWs with inter-defect spacing L=200 μm (blue) and L=300 μm (green). $\kappa_g = 0.01/\mu\text{m}$.

(4-4), the coupling coefficients of the two CROWs differ by a factor of exp($\kappa_g \Delta L$)=e, which agrees with the bandwidths and the group delay shown in Fig. 4.3.

4.3 High-Q Tapered Grating-Defect Resonators

4.3.1 Numerical Characterization of Strong Gratings

Fig. 4.4(a) shows a Bragg grating in a single-mode silicon-on-insulator waveguide which is 490 nm wide and 220 nm thick. The refractive indices of silicon and silicon oxide are 3.48 and 1.46 respectively. We consider the transverse electric (TE) mode throughout this thesis, and the effective mode index is 2.4. The grating is composed of periodic air holes, which are etched through the silicon layer. For weak gratings, the evaluation of κ_g is usually based on perturbation theory – An overlap integral of the perturbation $\Delta\varepsilon(x,y)$ and the modal fields $E(x,y)$ [56]. However, this method is not accurate for strong gratings, where the modal fields are strongly perturbed. The propagation constant of the waveguide mode is also strongly perturbed by the grating. Therefore, for each hole radius r, the grating period Λ needs to be determined for a given

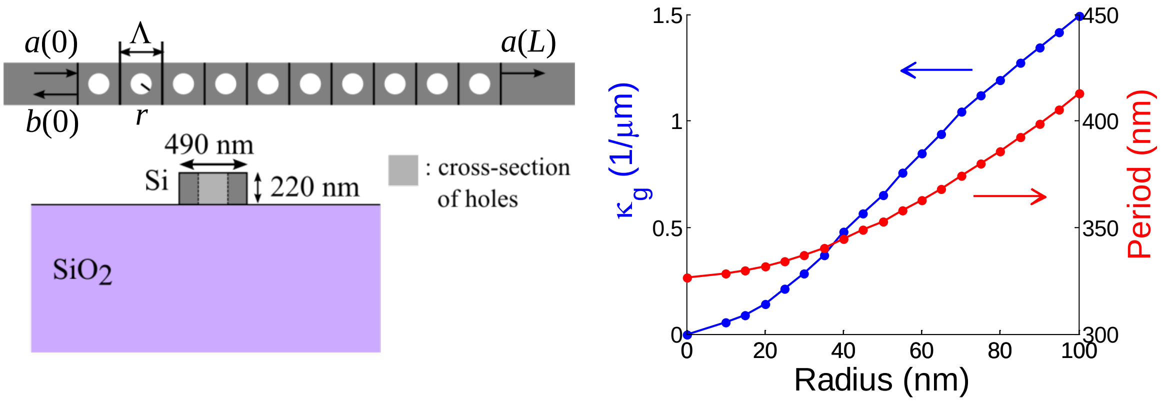

(a) (b)

Fig. 4.4. (a) Schematic drawing of a strong grating in a silicon waveguide and its cross-section. (b) Simulated κ_g and grating period as functions of hole radius

Bragg wavelength (1570 nm throughout this chapter). We design grating-defect resonators and CROWs to resonate at the Bragg wavelength for three reasons. First, the analysis based on coupled-mode equations is the simplest (δ=0 in Eq. (4-1)). Second, the grating strength is maximal at the Bragg wavelength, which enables the shortest possible device length. Last, when cascading resonators for CROWs, additional waveguide sections between adjacent resonators will be required if the resonant frequency is not at the Bragg frequency. The details of the coupling waveguide sections will be described in Chapter 5, where we introduce CROWs based on bandgap-modulated resonators.

Given a grating with a hole radius r and a period Λ, we can determine its Bragg wavelength and κ_g by simulating the transmission and reflection of the grating. For a grating with a constant κ_g between $z=0$ and $z=L$ and an input $a(0)=1$, the phase of the reflected mode $b(0)$ can be derived from Eq. (4-1) as $\theta_r=-\pi/2-\sin^{-1}(\delta/\kappa_g)$ if L is sufficiently long. The Bragg wavelength (δ=0) can be obtained at the condition $\theta_r=-\pi/2$. κ_g can be determined from the transmitted power at Bragg wavelength, $|a(L)|^2=1/\cosh^2(\kappa_g L)$.

We simulate grating structures in silicon waveguides using a 3D mode-matching method (MMM) [57]. Air holes are divided into longitudinal z-invariant sections. In each section, the total field is expressed as a superposition of the local eigen-modes (both forward and backward modes), which are solved using a finite-difference full-vectorial mode solver. Fields in adjacent sections are related by a scattering matrix which obeys continuity of the tangential components of electric and magnetic fields. The scattering matrix of the entire grating structure is obtained by cascading the scattering matrix of each section. MMMs are especially efficient for periodic structures. Once the scattering matrix of one unit cell is obtained, the entire grating structure can be constructed quickly. One major difference between our simulation and conventional MMMs is that in order to account for every component of radiation loss when simulating high-Q resonators, we use a complete set of modes. Therefore, we have to find a balance between accuracy and computation cost. This method is efficient compared to other simulation methods, especially when the grating structure is long.

Fig. 4.4(b) shows the calculated $\kappa_g(r)$ and $\Lambda(r)$ for a Bragg wavelength of 1570 nm. Since the area of holes is proportional to r^2, $\kappa_g(r)$ is quadratic at small radii. At larger radii, $\kappa_g(r)$ becomes linear and the slope starts decreasing, since κ_g corresponds to the first-order Fourier component of the grating. On the other hand, the perturbation of the propagation constant corresponds to the constant term of the Fourier components, so $\Lambda(r)$ is nearly a quadratic curve. Note that for a hole radius of 100 nm, κ_g is 1.49/μm, which is 16% of the propagation constant and thus corresponds to a very strong grating.

4.3.2 Design of High-Q Tapered Grating-Defect Resonators

Grating-defect resonators in strong gratings inevitably incur radiation losses. Although the resonant mode consists of only forward and backward waveguide modes, a and b, the spatial Fourier components which are phase-matched and thus couple to the radiation modes lead to radiation loss. Fig. 4.6(a) shows the modal field of a QWS resonator. The amplitude oscillation is from the interference between the forward and backward modes, and the envelope decays exponentially with the distance from the defect (at $z=0$). As a result, the spatial Fourier transform consists of two Lorentzian functions which are centered at the propagation constants of the forward and backward modes, as shown in Fig. 4.6(b). The Fourier components whose frequencies lie within the continuum of radiation modes ($-n_{clad} < k_z/k_0 < n_{clad}$) lead to radiation loss. The loss associated with a highly localized mode is especially large, since the Lorentzian functions are broad.

To reduce the radiation loss, we can engineer the modal field so as to minimize its spatial Fourier components within the radiation continuum. For example, if the envelope

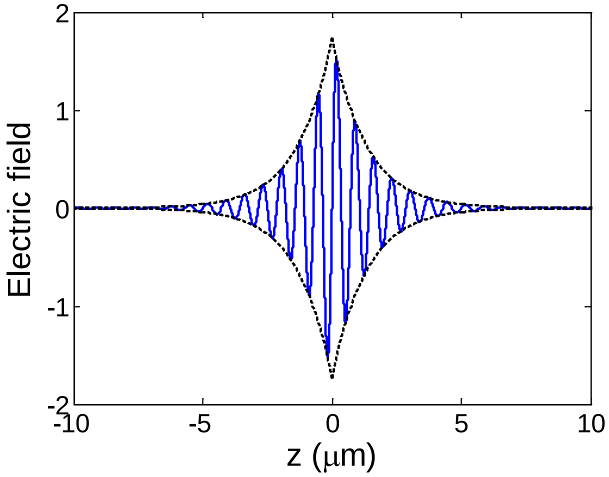

(a)

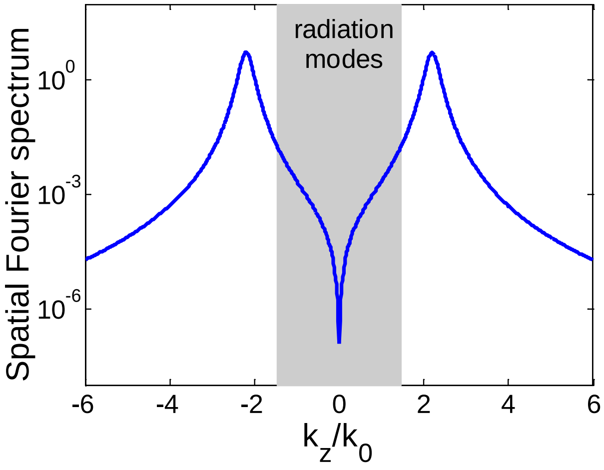

(b)

Fig. 4.5. (a) Field distribution of a QWS resonator mode. $\kappa_g = 0.75/\mu\text{m}$.
(b) Spatial Fourier transform of the QWS resonator mode

of the field is a Gaussian function, the Fourier transform consists of two Gaussian functions, which decay much faster than Lorentzian functions. In other words, the smoother Gaussian envelope leads to narrower functions in the spatial frequency domain. The modal field is controlled by the grating strength $\kappa_g(z)$, since the envelope is proportional to $\exp\left[-\int_0^{\Delta z}\kappa_g(\Delta z')d(\Delta z')\right]$, where Δz is the distance from the defect. If Gaussian distribution is desired, $\kappa_g(\Delta z)$ should be linear.

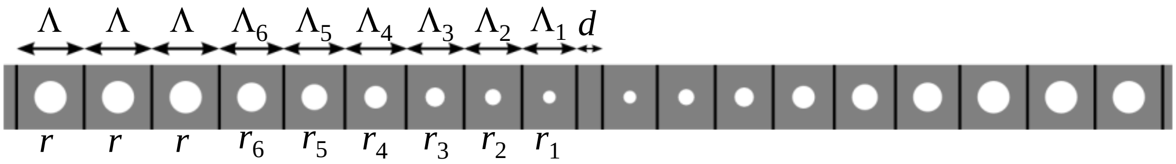

Fig. 4.6. Schematic drawing of a tapered grating-defect resonator with 6 tapered holes

A given profile of grating strength $\kappa_g(z)$ can be realized by the choice of the hole radii. Fig. 4.6 shows a tapered grating-defect resonator where the 6 nearest unit cells on each side of the defect are tapered. Both the radii and the periods are varied to ensure the same Bragg wavelength, 1570 nm. The defect length d is chosen to be $\lambda/(4n_{eff})$=162.5 nm, where n_{eff} is the effective index of the waveguide mode. We choose r=100 nm for the regular holes, which corresponds to Λ=413 nm and κ_g=1.49/μm according to Fig. 4.4(b). For the tapered grating, the grating strength assigned for the i-th hole is

$$\kappa_{g,i} = \kappa_g \left(\frac{i}{n_t + 1} \right)^{\alpha}, \tag{4-7}$$

where n_t is the number of tapered holes. The radius r_i and period Λ_i of each unit cell are determined based on the curves in Fig. 4.4(b). $\kappa_g(z)$ is a step function which is constant within each unit cell. If α=1, $\kappa_g(z)$ is approximately linear and leads to a Gaussian field distribution.

We consider grating-defect resonators with 4 and 6 tapered holes respectively. The objective is to find an α which minimizes the radiation loss. Fig. 4.7(a) shows the field distribution on one side of the defect for α=0, 0.55, and 1 based on their $\kappa_g(z)$. To estimate the radiation loss, we integrate the spatial Fourier spectrum over the radiation continuum. Fig. 4.7(b) shows the portion of energy in the radiation continuum, η_{rad}, as a function of α for 4 and 6 tapered holes, respectively. Tapering the grating reduces η_{rad} by more than 3 orders of magnitude. The effect of 6 tapered holes is better than that of 4

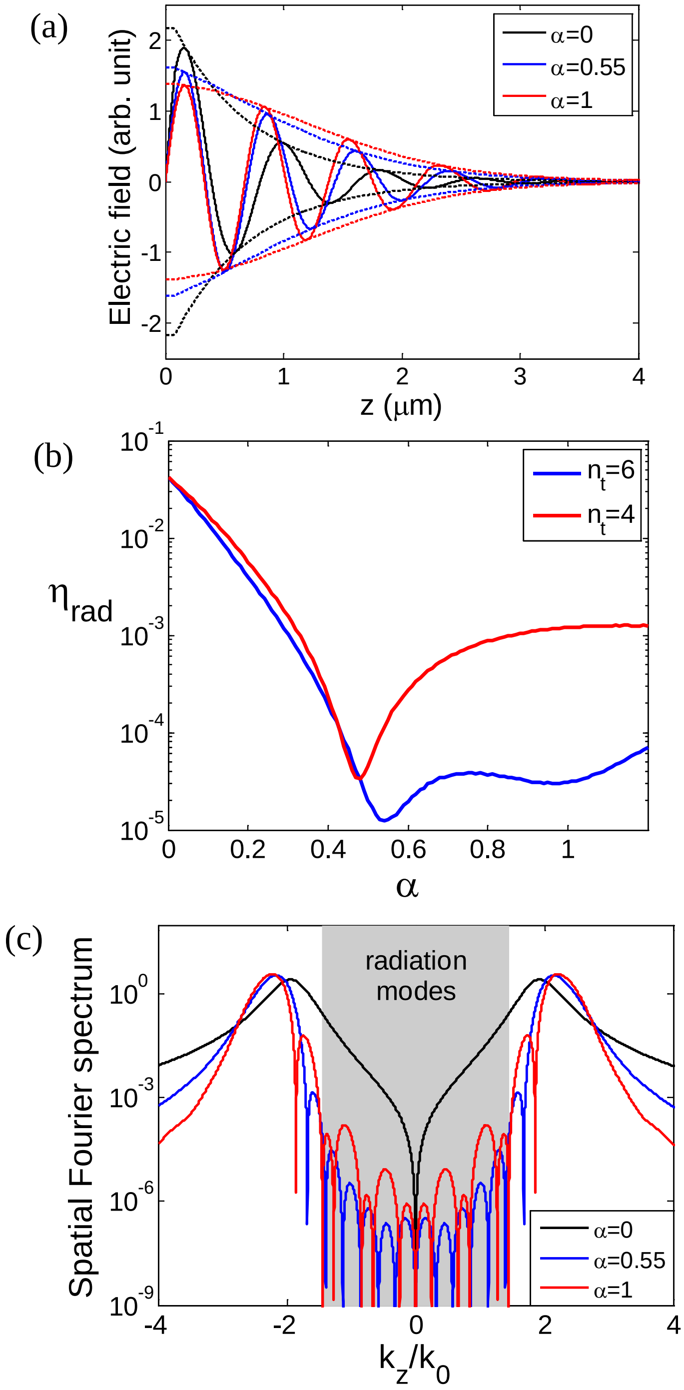

Fig. 4.7. (a) Field distribution (one side of the defect) of tapered grating-defect resonators with α =0, 0.55, and 1, respectively. (b) Energy portion in the continuum of radiation modes of grating-defect resonators as a function of α . (c) Spatial Fourier spectra of the modal fields for α =0, 0.55, and 1

tapered holes. The minimum of η_{rad} occurs at α=0.48 and 0.55 for 4 and 6 tapered holes respectively. This result shows that tapered gratings with α~0.5, corresponding to a field distribution of approximately $\exp[-(\Delta z)^{3/2}]$, are better than linear tapers with Gaussian distribution. Their field distributions are shown in Fig. 4.7(a), and the spatial Fourier spectra are shown in Fig. 4.7(c). Compared to α=1, while the spectrum of α=0.55 is larger at higher frequencies, it is an order of magnitude smaller within the radiation continuum. As a result, the taper profile with α=0.55 constitutes an optimal design.

To verify the results obtained from the Fourier analysis, we simulated resonators with various α using 3D MMMs. The quality factor Q was obtained from the linewidth of resonance in the transmission spectrum. Q consists of external Q (Q_e) due to the coupling to waveguides and intrinsic Q (Q_i) due to radiation loss:

$$\frac{1}{Q} = \frac{1}{Q_e(n)} + \frac{1}{Q_i}, \tag{4-8}$$

where n is the number of holes on one side of the defect. In order to find Q_i, we increase n until Q is saturated at Q_i, as shown in Fig. 4.8. The quality factor as a function of α for 4 and 6 tapered holes is plotted in Fig. 4.9. We plot η_{rad}^{-1} (multiplied by a constant so that it is equal to Q at α=0) on the same figure for comparison. The curves of Q agree

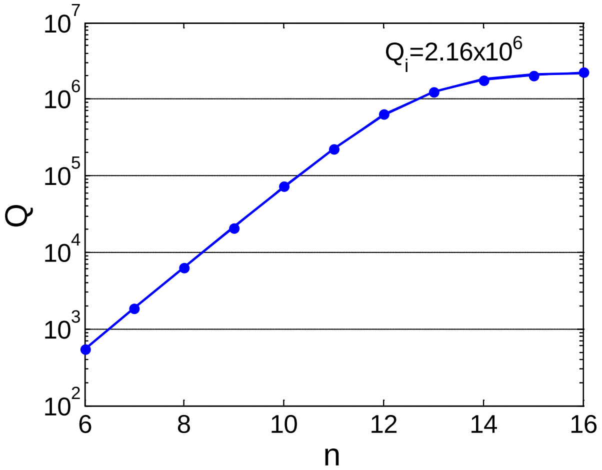

Fig. 4.8. Quality factor as a function of number of holes on each side of the defect. α =0.55, n_t=6

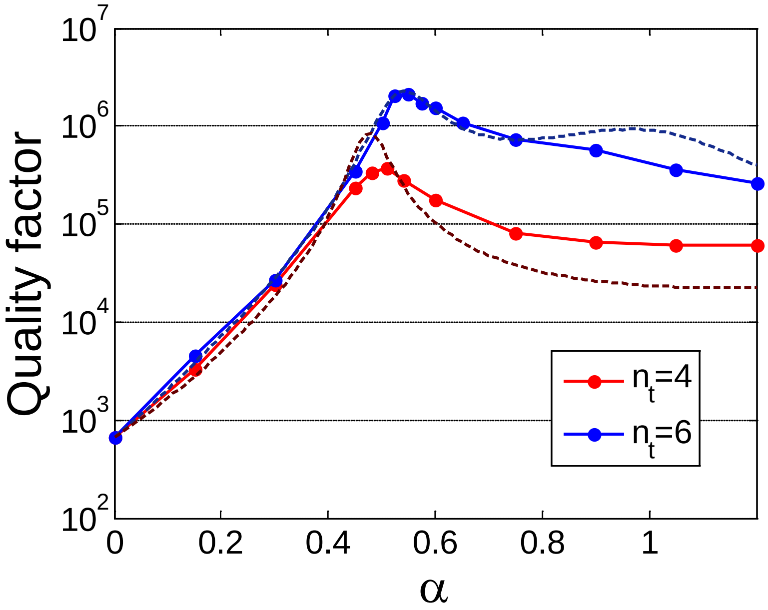

Fig. 4.9. Simulated quality factor as a function of α for grating-defect resonators with 4 and 6 tapered holes, respectively. Dashed lines show the corresponding η_{rad}^{-1}.

closely with η_{rad}^{-1}. The maximum of Q occurs at α=0.51 and 0.55 for 4 and 6 tapered holes, respectively. The highest Q for 6 tapered holes is 2.16×10^6 at α=0.55. It is an order of magnitude higher than the theoretical Q of grating-defect resonators designed in the literature [51, 52]. The radii of the tapered holes are 41.5, 54.6, 64.8, 72.9, 82.9, 92.1 nm, and the periods are 346.3, 357.7, 367.9, 378.3, 389.7, 401.3 nm. The modal volume is $0.38\cdot(\lambda/n_{\mathrm{Si}})^3$ (simulated using COMSOL multiphysics), which is smaller than those of 1D photonic crystal resonators resonating at frequencies near the grating band edge [53, 54]. Further increasing the number of tapered holes will result in a higher Q. However, the resulting smaller holes may not be practical.

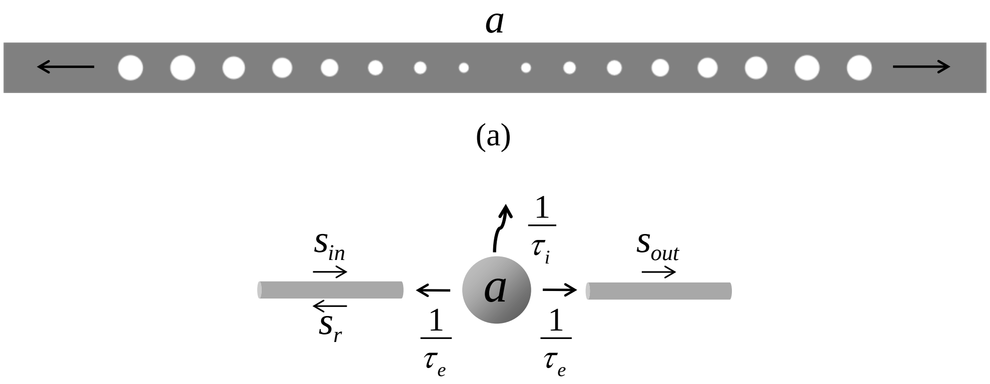

(a)

(b)

Fig. 4.10. (a) Schematic drawing of a symmetric grating-defect resonator. (b) The corresponding coupled-mode diagram

4.4 Inline Coupling of Resonators

Inline resonators are, by definition, fabricated, cascaded, and coupled in a single waveguide. The objective of this section is to derive the inter-resonator coupling coefficient as a function of individual quality factors.

Fig. 4.10 shows a symmetric inline resonator, i.e., the coupling to the waveguides is equally strong on both sides. In a symmetric grating-defect resonator, the number of holes on both sides of the defect is equal. The time-domain coupled-mode equations are given by

$$\begin{gathered} \frac{da}{dt} = (i\omega - \frac{1}{\tau_i} - \frac{2}{\tau_e})a - i\mu s_{in} \\ s_{out} = -i\mu a \qquad , \\ s_r = s_{in} - i\mu a \end{gathered} \tag{4-9}$$

where a is the resonator mode amplitude, s_{in}, s_r, and s_{out} are the input, reflected, and transmitted mode amplitudes, respectively, ω is the resonant frequency, $1/\tau_i$ and $1/\tau_e$ are the intrinsic loss and the external loss to each waveguide respectively, and μ is the waveguide-resonator coupling. It can be shown that $\mu = \sqrt{2/\tau_e}$ using conservation of energy. The quality factor of the resonator is given by $Q=\omega\tau/2$, where $1/\tau=1/\tau_i+2/\tau_e$ is the total loss rate. In the regime where intrinsic loss is negligible (the linear region in Fig. 4.8), $Q=\omega\tau_e/4$. Therefore, we obtain $1/\tau_e=\omega/(4Q)$ if Q is given.

In Fig. 4.11, we consider two inline resonators cascaded in a waveguide. The inter-resonator coupling is via the coupling waveguide of length d. The coupled-mode equations of the two resonators and the coupling waveguide are given by

$$\begin{aligned} \frac{da_1}{dt} &= (i\omega_1 - \frac{1}{\tau_{e1}})a_1 - i\mu_1 s_- e^{i\theta} \\ \frac{da_2}{dt} &= (i\omega_2 - \frac{1}{\tau_{e2}})a_2 - i\mu_2 s_+ e^{i\theta} \,. \\ s_+ &= s_- e^{i\theta} - i\mu_1 a_1 \\ s_- &= s_+ e^{i\theta} - i\mu_2 a_2 \end{aligned} \qquad (4\text{-}10)$$

The notations are shown in Fig. 4.11(b). θ is the phase accumulated in the propagation. The resonant frequencies and the external losses of the two resonators can be different in general. The intrinsic losses and the coupling to the other resonators or waveguides have been ignored and can be added to the equations. Combining the last two equations of Eq. (4-14), s_+ and s_- can be expressed as linear combinations of a_1 and a_2, and Eq. (4-14) can

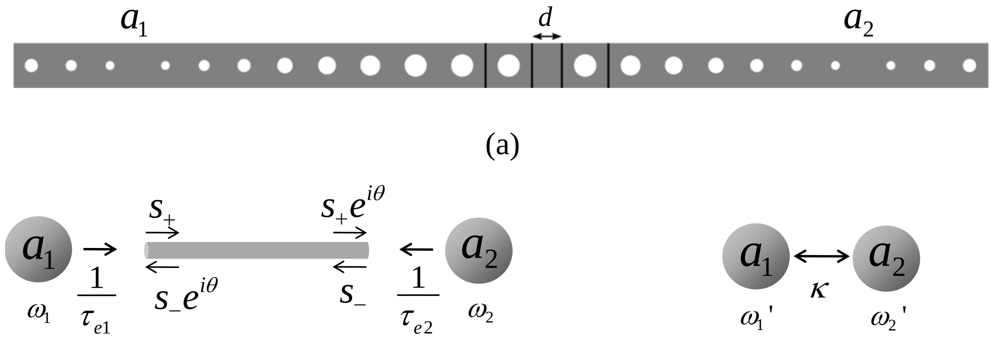

(a)

(b)

(c)

Fig. 4.11. (a) Schematic drawing of the inline coupling of two grating-defect resonators. (b) The coupled-mode diagram of two resonators coupled via a waveguide. (c) The coupled-mode diagram of two directly coupled resonators

be rewritten as coupled-mode equations of two directly coupled resonators (shown in Fig. 4.11(c)):

$$\begin{aligned}\frac{da_1}{dt} &= i(\omega_1 - \frac{\cot\theta}{\tau_{e1}})a_1 - i\frac{\csc\theta}{\sqrt{\tau_{e1}\tau_{e2}}}a_2 \\ \frac{da_2}{dt} &= i(\omega_2 - \frac{\cot\theta}{\tau_{e2}})a_2 - i\frac{\csc\theta}{\sqrt{\tau_{e1}\tau_{e2}}}a_1\end{aligned}. \tag{4-11}$$

The inline coupling leads to detuning of resonant frequencies and a coupling coefficient which depend on the round-trip phase of the coupling waveguide cavity, 2θ:

$$\begin{aligned}\Delta\omega_{1,2} &= -\frac{\cot\theta}{\tau_{e1,2}} \\ \kappa &= \frac{\csc\theta}{\sqrt{\tau_{e1}\tau_{e2}}}\end{aligned}. \tag{4-12}$$

When designing CROWs, we require identical resonant frequencies. If the frequency detuning $\Delta\omega$ is nonzero, the resonators along the CROW may experience different frequency detuning. For example, the frequencies of the first and last resonators are less detuned since they only couple to one resonator, while the other resonators have two neighbors. Therefore, we require $\Delta\omega$=0, which corresponds to $2\theta=\pi$, a totally destructive interference in the coupling cavity. $2\theta=\pi$ also leads to a minimal coupling coefficient. The cavity round-trip phase includes the phase of reflection from the grating and the propagation phase in the cavity. At the Bragg wavelength, the reflection phase $\theta_r = -\pi/2 - \sin^{-1}(\delta/\kappa_g)$ is $-\pi/2$. Therefore, the round-trip phase with d=0 is already π. This is an important reason why we choose to work at the Bragg wavelength. If the resonance is near the band edge, an additional phase section of length d is required to satisfy a round-trip phase of π. In Chapter 6, we will show the design of CROWs based on grating band-edge modes. We will show how important the phase sections are for the transmission spectra of CROWs.

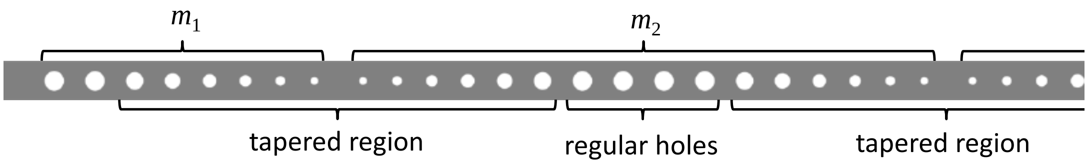

Fig. 4.12. Schematic drawing of the first two resonators of a grating-defect CROW

4.5 Grating-Defect CROWs with Uniform Coupling Coefficient

Grating CROWs are formed by cascading the high-Q grating-defect resonators designed in Section 4.3 . Fig. 4.12 shows the first two resonators of a grating CROW. The inter-resonator coupling is controlled via the number of holes between neighboring defects, denoted as m. m includes the number of tapered holes ($2n_t$) and the number of regular holes (n_{reg}). When cascading two symmetric grating resonators with external quality factors Q_1 and Q_2 respectively, the coupling coefficient can be derived from Eq. (4-16) as

$$\kappa = \frac{\omega}{4\sqrt{Q_1 Q_2}}. \tag{4-13}$$

If the resonant frequency is not at the Bragg wavelength, an additional phase section between two resonators is required for appropriate coupling in CROWs, as will be shown in Chapter 5. We have shown in Eq. (4-6) that Q is proportional to $\exp(2\kappa_g L)$. For a tapered resonator, the relation is modified as

$$Q \propto \exp\left[2\int_0^L \kappa_g(z)dz\right] = \exp\left[2\sum_{i=1}^{n}\kappa_{g,i}\Lambda_i\right] = \exp\left[2\sum_{i=1}^{n_t}\kappa_{g,i}\Lambda_i\right]\cdot\exp\left[2n_{reg}\kappa_g\Lambda\right], \tag{4-14}$$

which breaks down into the contribution of each hole in the tapered region and the regular grating, respectively. Therefore, Q can be written as

$$Q = Q_0 \cdot a^{2n_{reg}}, \tag{4-15}$$

where Q_0 is the quality factor of a resonator with only the tapered region (no regular hole) and $a \equiv \exp(\kappa_g \Lambda)=1.849$. We fit the curve in Fig. 4.8 (α=0.55, n_t=6) with Eq. (4-15) and obtain Q_0=548 and a=1.848. If we cascade two resonators with $n_{reg,1}$ and $n_{reg,2}$ respectively, we obtain the inter-resonator coupling coefficient given by

$$\kappa = \frac{\omega}{4\sqrt{Q_1 Q_2}} = \frac{\omega}{4Q_0} a^{-n_{reg}}, \qquad (4\text{-}16)$$

where $n_{reg} = n_{reg,1} + n_{reg,2}$ is the total number of regular holes between two defects. For the first or last resonators, the external loss rate to the waveguides is given

$$\frac{1}{\tau_e} = \frac{\omega}{4Q} = \frac{\omega}{4Q_0} a^{-2n_{reg}}, \qquad (4\text{-}17)$$

where n_{reg} is the number of regular holes in the first or last grating section. To match between the CROW and the waveguides, we require $\kappa=1/\tau_e$ [58]. Therefore, the number of holes in the first and last sections is one half of the number of holes in the middle sections, i.e., $m_1=m_{N+1}=m/2$.

Fig. 4.13(a) and Fig. 4.13(b) show the spectra of transmission and group delay of N=10 CROWs for m=12, 14, and 16, respectively (n_{reg}=0, 2, and 4). The band center is

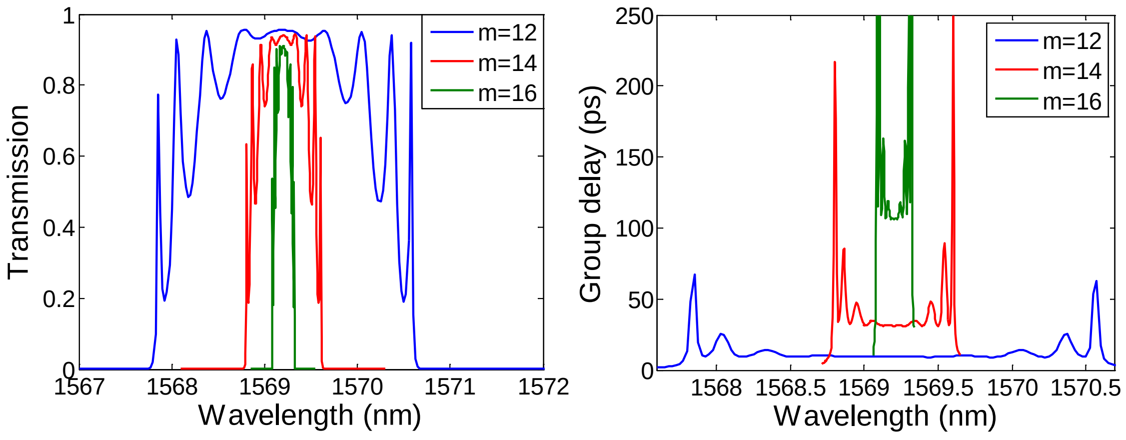

(a) (b)

Fig. 4.13. Spectra of (a) transmission and (b) group delay of 10-resonator grating-defect CROWs with m=12, 14, and 16, respectively

at 1569.2 nm. Both the bandwidth and the group delay are dictated by *m*. The bandwidth is equal to 4κ and the group delay at the band center is given by $N/(2\kappa)$. Adding two holes between defects results in a factor of a^2=3.415 in κ. Note that the maximal transmission for m=12 is only 0.955. This is due to the strong index contrast between the waveguide and the grating section, which scatters light to the radiation modes. The strong index contrast can be reduced by tapering the grating at the input [52]. For larger *m*, the radiation loss increases due to the longer delay. The transmitted power can be written as $\exp(-\omega\tau/Q_i)$, where τ is the group delay. The delay for m=16 is 106.3 ps, which leads to a transmitted power of 0.943. Including the scattering loss at the input, the transmission drops to about 0.9, which agrees with the simulation.

4.6 Filter Design Based on Grating-Defect CROWs

High-order bandpass filters with optimized transmission and dispersive properties can be realized in CROWs if the coupling coefficients are allowed to take on different values. For example, Butterworth filters exhibit maximally flat transmission, while Bessel filters possess maximally flat group delay. In Chapter 2, we showed that for a desired filter response, the coupling coefficients which determine the transfer function of CROWs can be derived. The coupling coefficients of N=10 Butterworth and Bessel filters were listed in Table 2.3. These coupling coefficients are normalized to a chosen bandwidth parameter *B*.

In grating-defect CROWs, the coupling coefficients are translated to the numbers of holes based on Eqs. (4-16) and (4-17). However, these numbers of holes are in general non-integers. Table 4.1 lists the numbers of regular holes corresponding to the two filters in Table 2.3. The bandwidth parameter *B* is chosen as $2\cdot\kappa(n_{reg}=4)$ so that its bandwidth is equal to those of CROWs with uniform coupling and n_{reg}=4 (m=16 in Fig. 4.13). Since

Table 4.1. Numbers of regular holes of N=10 Butterworth and Bessel CROWs.

Filter type	n_{reg}
N=10 Butterworth	(0.495, 1.854, 3.078, 3.625, 3.896, 3.980, 3.896, 3.625, 3.078, 1.854, 0.495)
N=10 Bessel	(0.426, 1.726, 2.990, 3.670, 4.802, 4.659, 3.568, 3.295, 2.787, 1.589, 0.366)

κ is an exponential function of n_{reg}, we can add an arbitrary Δn_{reg} in order to change the bandwidth without having to rederive all the n_{reg}. A non-integer n_{reg} can be realized by an integer number $n_{int} = \lceil n_{reg} \rceil$ of identical holes which are equivalent to a fraction $\gamma = n_{reg}/\lceil n_{reg} \rceil$ of a regular hole. For example, 3.6 regular holes are equivalent to 4×0.9 holes. This can be seen in

$$a^{n_{reg}} = \exp\left[n_{reg}\kappa_g\Lambda\right] = \exp\left[n_{\text{int}}\kappa_g(r)\Lambda(r)\right]. \tag{4-18}$$

Therefore, we need to determine the hole radius r whose $\kappa_g(r)\Lambda(r)$ is equal to $\gamma\kappa_g\Lambda$. This can be done by interpolating the curve of $\kappa_g\Lambda$ versus r. For example, the radius of a γ=0.9 hole is 90.1 nm. If n_{reg} is negative, we can reduce the hole sizes starting from the outermost tapered holes. An alternative way is to choose a resonator with fewer tapered

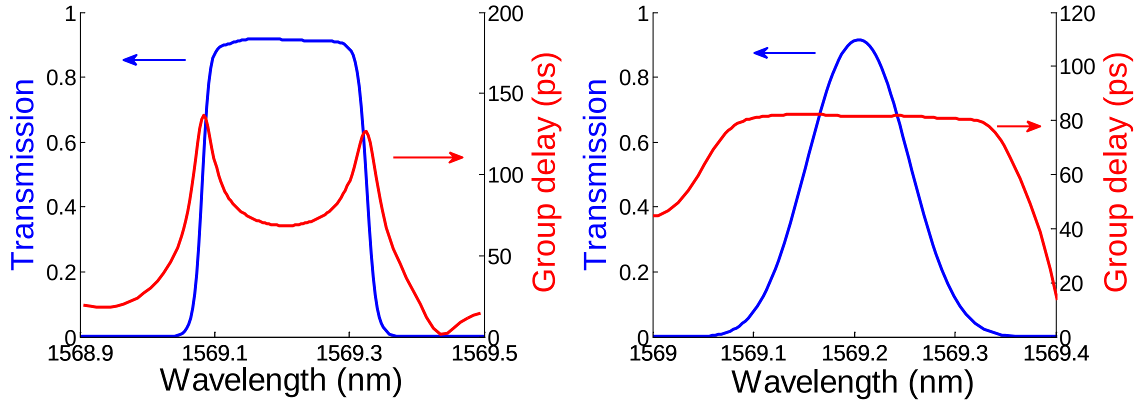

(a) (b)

Fig. 4.14. Spectra of transmission and group delay of (a) an N=10 Butterworth grating CROW and (b) an N=10 Bessel grating CROW

holes, such as the resonators with n_t=4 designed in Section 4.3 .

Fig. 4.14(a) and Fig. 4.14(b) show the spectra of transmission and group delay of an *N*=10 Butterworth CROW and an *N*=10 Bessel CROW, respectively. The values of transmission at the band center are both 0.916, indicating a small intrinsic loss due to the large group delay in addition to the scattering loss at the input. Substracting the scattering loss which corresponds to a transmission of 0.955, the intrinsic Q can be obtained from the intrinsic loss and the group delay and is determined to be 2.34×10^6 and 1.97×10^6 for Butterworth and Bessel CROWs, respectively. Therefore, the tailoring of coupling coefficients does not degrade the *Q* of the resonators. In practice, the *Q* of the resonators may degrade due to imperfection of fabrication. With larger intrinsic loss, the transmission spectrum of Butterworth CROWs may be distorted since the loss is proportional to the group delay. The predistortion technique introduced in Section 2.5 can be applied to pre-compensate for the distortion provided that the *Q* can be estimated and is uniform over the CROW. Since the group delay of Bessel CROWs is flat within the bandwidth, the transmission spectrum is not distorted by uniform resonator loss.

4.7 Effect of Fabrication Disorder on Grating-Defect CROWs

The fabrication disorder in the resonant frequency of each resonator and the coupling coefficients has been the major limitation of CROWs. In Section 2.7 we have investigate the disorder effect of $\delta\omega / B$, $\delta\kappa / \kappa$, and *N*, which is general for all kinds of resonators. In this section we investigate how variation of the hole radii affect the resonant frequency and the coupling coefficient.

Due to the ultra-small modal volume of the grating-defect resonators designed to resonate at the Bragg wavelength, the shift of resonant wavelength due to deviation of hole radii is relatively large. Fig. 4.15 shows the wavelength shift corresponding to 1 nm change of radius for each hole starting from the one nearest to the defect. Since the mode is concentrated near the defect, the resonant wavelength is more sensitive to the deviation of the first three holes. If the standard deviation of each hole radius is $\delta r = 1$ nm, the standard deviation of the resonant wavelength, considering holes on both sides of the defect, is $\delta\lambda = 0.8$ nm. Depending on the fabrication quality (δr), the standard deviation of the resonant wavelength is $\delta\lambda = 0.8 \cdot \delta r$.

The deviation of coupling coefficients due to change of radius can be estimated using the function $\kappa_g(r)$ in Fig. 4.4(b). Considering the regular hole whose radius is 100 nm, 1 nm change of radius leads to $\Delta\kappa_g = 0.016$, which corresponds to $\Delta\kappa/\kappa = \exp(\Delta\kappa_g \cdot \Lambda) =$ 0.66%. We consider 14 holes between adjacent defects (*m*=14), $\delta\kappa/\kappa = 2.5\%$ for δr = 1 nm. We can look up the disorder effect for $\delta\lambda$ and $\delta\kappa/\kappa$ in Fig. 2.12. For typical bandwidth (B corresponding to <20 nm in wavelength), the disorder effect in coupling coefficient is much smaller than the disorder in resonant wavelength. Therefore, disorder in resonant wavelength is the major source of loss.

Because of the higher wavelength sensitivity of grating-defect resonators compared to

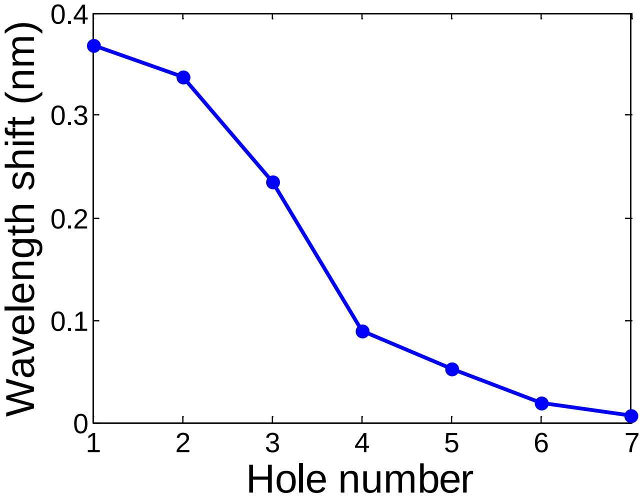

Fig. 4.15. Shift of resonant wavelength due to 1 nm change of radius for each hole starting from the one nearest to the defect

those of larger resonators such as ring resonators, grating-defect CROWs designed in this paper are more practical for larger bandwidth applications. Although larger bandwidth corresponds to smaller delay, the group velocity is still small considering the length of grating-defect resonators. If the grating is chosen to be weaker, such as shallower holes, the wavelength sensitivity will become smaller due to the larger modal size. Therefore, the length of each resonator and the wavelength sensitivity appear to a trade-off in the design of grating-defect CROWs.

4.8 Summary

We have demonstrated a systematic approach to design high-Q tapered grating-defect resonators, control the inter-resonator coupling, and design high-order grating CROW filters. The formalism based on coupled-mode theory is valid in strong gratings, with the help of 3D simulations for the characterization of gratings. The optimized Q of 2.16×10^6 is an order of magnitude higher than the theoretical Q of grating-defect resonators designed in the literature. Based on these high-Q resonators, CROWs which are shorter than 60 μm exhibit a group delay of more than 100 ps while maintaining a transmission of 0.9. The control of inter-resonator coupling via the number of holes provides a convenient way of designing coupled-resonator structures. Furthermore, we demonstrated the design of tenth-order Butterworth and Bessel filters which possess maximally flat transmission and group delay, respectively. Besides flat transmission, Butterworth CROWs are more robust against fabrication disorder compared to CROWs with uniform coupling coefficient.

The grating-defect CROWs designed in this chapter are attractive for their small footprints, high quality factors, and their natural coupling to input and output waveguides. The coupled-mode formalism developed in this work can be further applied to other types of strong grating structures to minimize the coupling to radiation modes and reliably calculate the transfer function of grating structures when the coupling to radiation modes is negligible.

Chapter 5

Experiment of Grating-Defect CROWs

5.1 Fiber-to-Chip Coupling

The cross-section of the silicon waveguides designed in Chapter 4 is 490 nm wide and 220 nm thick, as shown in Fig. 5.1(a). To couple light at a wavelength of 1570 nm into a waveguide, we can focus light into a small spot with a lens. However, even if we choose an objective with a high numerical aperture (NA), say NA = 0.65, the minimum beam diameter is given by $d = 2\lambda/(\pi \cdot NA) = 1.54\ \mu\text{m}$. The mismatch between the spot size and the mode size leads to a large coupling loss. Besides, the large index difference between silicon and air at the facet causes a large reflection, which leads to Fabry-Perot oscillations and distorts the measured spectra of transmission and group delay of CROWs.

To overcome the coupling loss and the reflection at the facets, we have worked on spot-size converters (SSCs) for maximizing the modal match and grating couplers which utilize the Fourier component of a grating to couple light out in the vertical direction. The fabrication of SSCs involves the deposition and patterning of an upper cladding. On the other hand, the fabrication of grating couplers does not require extra steps. Besides, the steps of lapping and cleaving for edge coupling can be removed with grating couplers, which reduces the possibility of contamination and enables further processing after measurement. The drawback of grating couplers is the limited bandwidth. In what follows we describe the design of both couplers.

5.1.1 Spot-Size Converters (SSCs)

The idea of spot-size converters is to convert adiabatically the small waveguide mode to a much larger mode which matches with the focused beam spot [59, 60]. As we reduce the width of the waveguide with a taper, the mode is less confined and becomes larger. An upper cladding is required to make the cladding symmetric so that the mode can still be guided. Since the lower cladding is silicon oxide, the optimal material for the upper cladding is silicon oxide, which can be deposited by plasma-enhanced chemical vapor deposition (PECVD).

Fig. 5.1(b) shows a SSC with 2 μm thick SiO_2 layer on top of a-160-nm wide silicon waveguide. The modal field is shown in Fig. 5.2(a), simulated with COMSOL multiphysics. The diameter of the mode increases as we decrease the width of the silicon

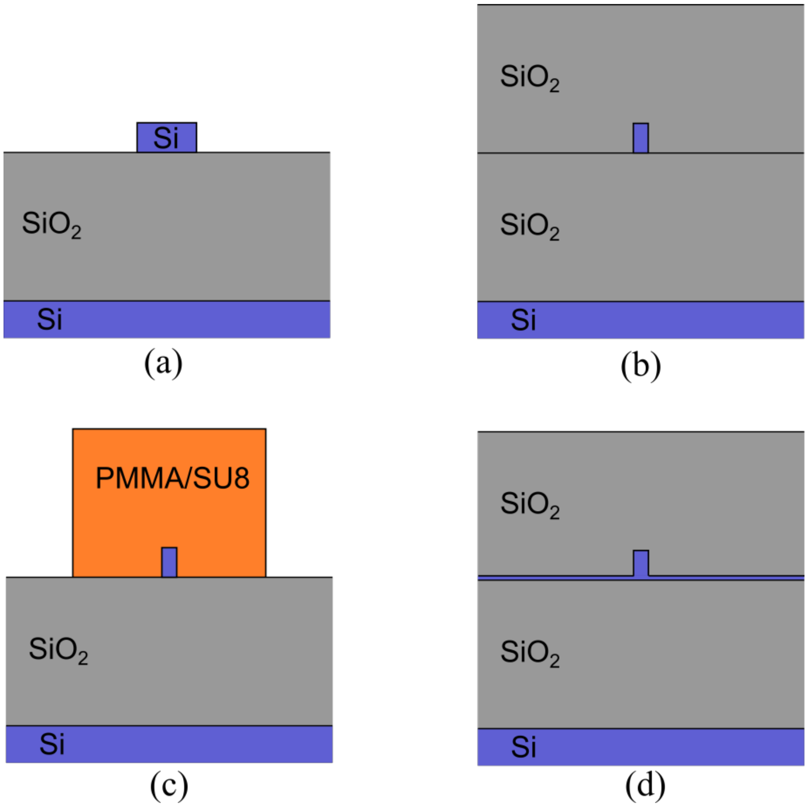

Fig. 5.1. Schematic drawings of (a) a single-mode silicon waveguide, (b) a SiO_2 SSC, (c) a PMMA or SU8 SSC, and (d) a SiO_2 SSC with a thin under-etched silicon slab

waveguide. To find out an optimal width which matches with a given input spot size, we perform an overlap integral of the input beam and the SSC mode, which is given by

$$\Gamma = \frac{\int E_{SSC} E_{input} dxdy}{\sqrt{\int E_{SSC}{}^{2} dxdy} \cdot \sqrt{\int E_{input}{}^{2} dxdy}}, \tag{5-1}$$

where E_{SSC} and E_{input} are the x component of the electric fields of the SSC mode and the input beam respectively, and E_{input} is assumed as a Gaussian. The relative positions of the two modes have been chosen to maximize Γ. We take an input beam diameter of 3 μm, and the function of Γ versus waveguide width is plotted in Fig. 5.2(b). The maximum is at a width of 160 nm. We also show in Fig. 5.2(b) the overlap integral when the input beam is tilted at 6° in the horizontal direction, which we consider as the worst case in the setup. Γ drops by 10% with the tilted input.

The deposited SiO_2 on top of the grating resonators and CROWs has to be removed, since the design of CROWs in Chapter 4 is for air cladding, and the PECVD oxide may not fill the air holes fully and uniformly. However, the buried oxide beneath the silicon

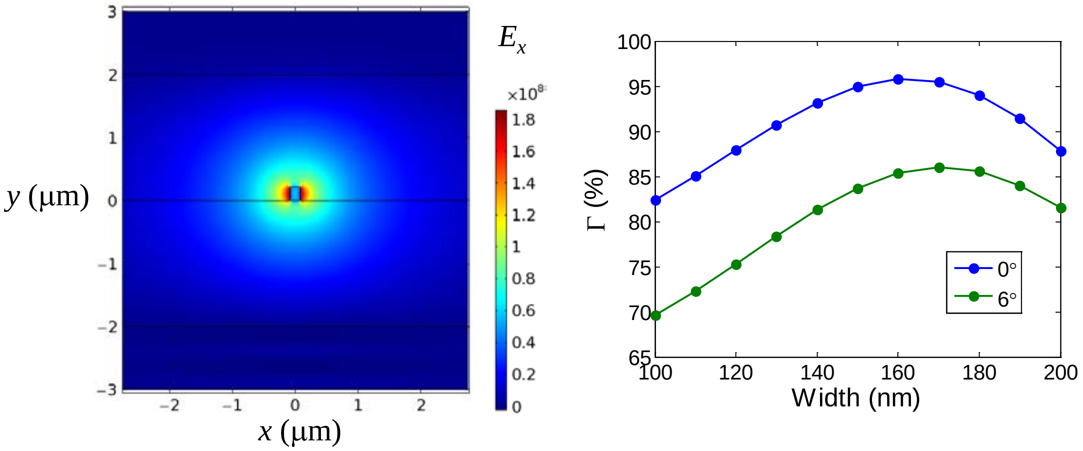

(a) (b)

Fig. 5.2. (a) Field distribution of the mode of a SSC with a silicon width of 160 nm. (b) Overlap integral of the SSC mode and the input beam as a function of the silicon waveguide width. Blue line is for normal incidence (0°); green line is for a tilted input at 6° in the x-z plane

waveguide makes the timing of the SiO_2 back etch difficult. A little over-etch may suspend the whole waveguide, thereby bending and breaking the devices. As alternatives we have used e-beam resists, including PMMA (n=1.49) and SU8 (n=1.568), as the upper cladding. PMMA is a positive e-beam resist, while SU8 is a negative e-beam resist. After development, the e-beam resist on top of the grating resonators will be removed. Fig. 5.3(a) shows the modal field of a SSC with a 2-μm-thick SU8 layer and a 120-nm-wide Si waveguide. Since the refractive index of SU8 is different form the index of SiO_2, the mode becomes unguided easily. Therefore, a patterning of the upper cladding is necessary, as shown in Fig. 5.1(c). Fig. 5.3(b) shows the mode of a SSC with a 2.5 μm wide SU8 waveguide. Since the SU8 is a waveguide by itself, the silicon waveguide can be removed totally, and the SSC is an adiabatic transition from a Si waveguide to a SU8 waveguide. Fig. 5.4(a) shows a SEM image of a 3-μm-wide fabricated PMMA SSC waveguide on top of a Si waveguide.

However, although the idea of SSCs with e-beam resist seems to work well, and we have measured a very low coupling loss of 2.2 dB per coupler, we have observed resist residue at the edges of waveguides or holes, as shown in Fig. 5.4(b). The residue can

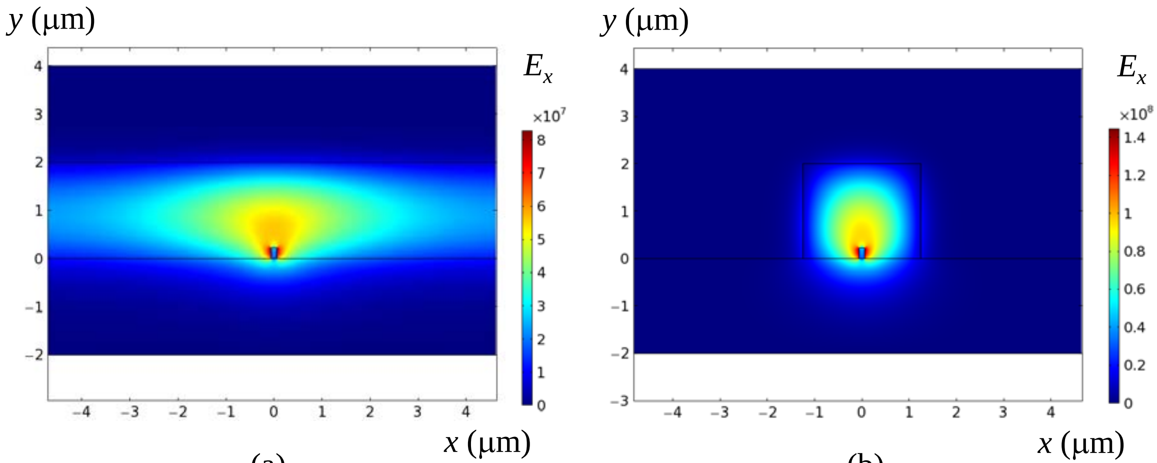

(a) (b)

Fig. 5.3. Field distribution of the mode of (a) a SSC with a SU8 slab and (b) a SSC with a 2.5-μm-wide SU8 waveguide

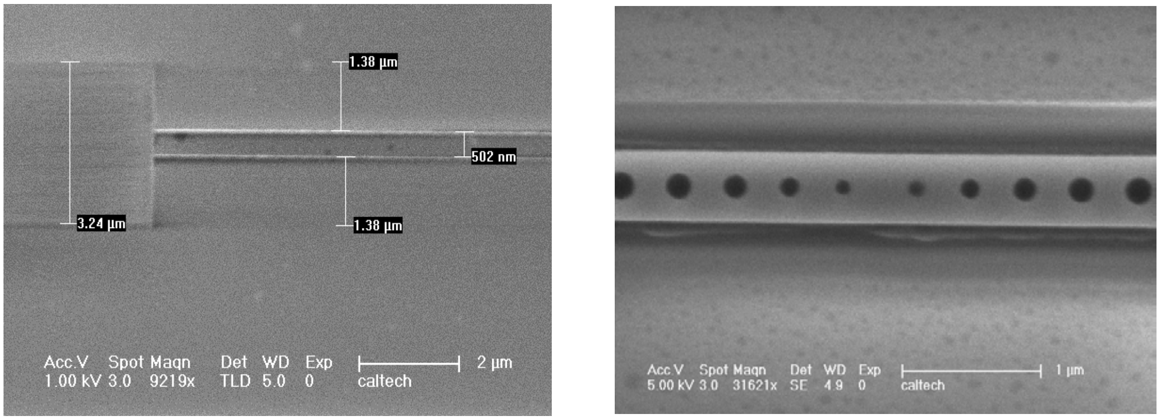

(a) (b)

Fig. 5.4. (a) A SEM image of a PMMA SSC. (b) Resist residue on a grating resonator after developing PMMA for PMMA SSCs

degrade the quality of the resonators and cause deviation of resonant frequency and coupling coefficient of CROWs. Moreover, cleaving samples with PMMA or SU8 waveguides breaks the waveguides easily, and thus the yield of the devices is often not good with PMMA or SU8 SSCs.

Our final solution for SSCs is a modified SiO_2 SSC, as shown in Fig. 5.1(d). During the Si dry etch, we intentionally leave a very thin Si layer which is 5 to 15 nm thick. With a very careful calibration of etch rate, the thickness can be controlled accurately. Due to the thin Si layer as the etch stop, we were able to etch back the deposited SiO_2 layer on top of the devices without having to timing the oxide etch. This silicon under-etch results in shallower trenches and air holes, which changes the strength of the grating and slightly degrades the quality factor. Consequently, we redesigned the resonators based on the hole depth.

5.1.2 Grating Couplers

Grating couplers utilize the Fourier component of a surface grating to couple a guided mode to a radiation mode which emits at an angle and is collected by a fiber. A side view of a grating coupler is shown in Fig. 5.5(a). The phase matching condition is given by

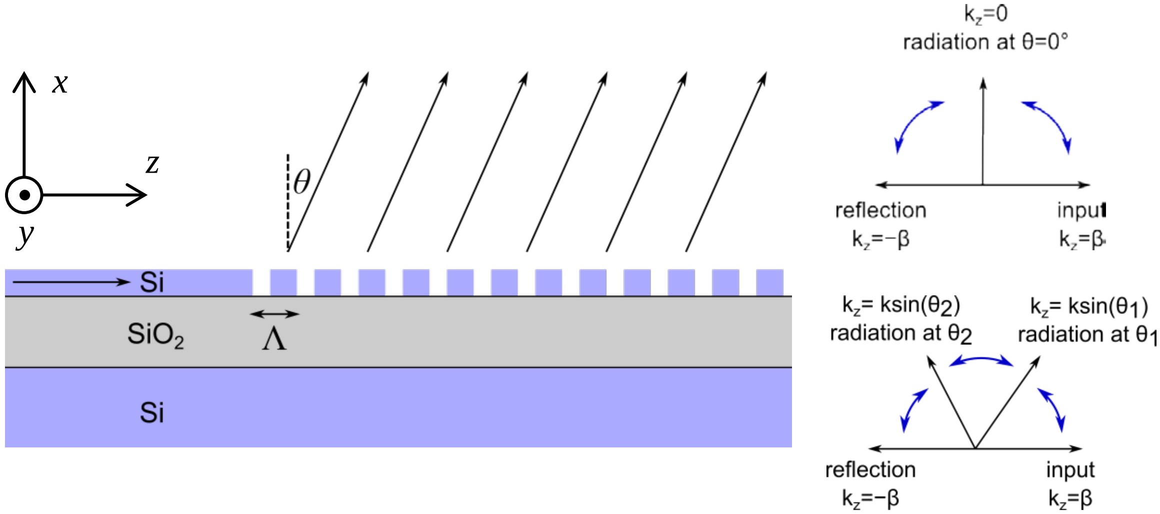

(a) (b)

Fig. 5.5. (a) Schematic drawing of a grating coupler. (b) Phase matching condition for some emitting angles that should be avoided

$$\frac{2\pi}{\Lambda} = \beta - k\sin\theta , \tag{5-2}$$

where Λ is the period of the grating, β is the propagation constant of the waveguide mode with grating, $k = 2\pi/\lambda$, and θ is the emitting angle. Note that β depends on the duty cycle and the etch depth of the grating and is smaller than the propagation constant of the Si waveguide mode. The emitted field is collected by a single-mode fiber directly above the grating or a fiber focuser which focuses light at the grating. The design of the grating concentrates on matching the emitted profile with the fiber mode, which is assumed to be a Gaussian beam with a diameter of 8.5 μm. First, the width of the grating

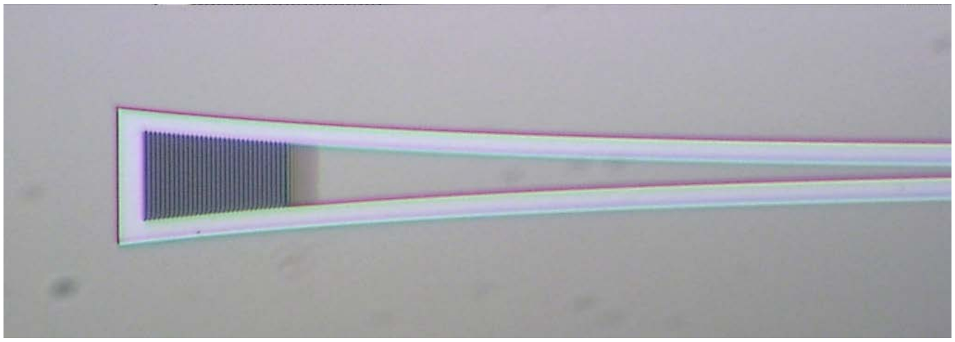

Fig. 5.6. A microscope image of a grating coupler and the exponential taper

pad is selected as 9 μm to match with the width of the Gaussian beam. We used a taper with an exponentially growing width to convert from a 490-nm-wide single-mode waveguide to the 9-μm-wide grating pad. Fig. 5.6 shows an image of a grating coupler and the exponential taper. Since the width of the grating pad is large enough, we can assume that the structure is invariant in the *y* direction and simplify the problem to a two-dimensional structure as shown in Fig. 5.5(a). We take the indices of Si and SiO_2 directly as the effective indices.

There are two emitting angles we should avoid using. They are shown in Fig. 5.5(b). One is at 0° with respect to the vertical (*x*) axis. As the first-order Fourier component ($2\pi/\Lambda$) emits light vertically, the second-order Fourier component ($4\pi/\Lambda$) couples the forward mode to the backward mode and thus causes reflection. Likewise for an angle around 60° where the third-order Fourier component causes reflection.

To maximize the mode match with a Gaussian beam, we design the grating strength as a function of *z* by varying the duty cycle. The coupling between the guided mode and the radiation mode induces propagation loss of the guided mode. The propagation of the guided mode in a grating can be described as

$$\frac{du}{dz} = -\alpha(z)u, \tag{5-3}$$

where u is the mode amplitude and $\alpha(z)$ is the loss coefficient. The power loss per unit length is given by

$$-\frac{du^2}{dz} = -2u\frac{du}{dz} = 2\alpha(z)u^2. \tag{5-4}$$

The grating couples light to both upward and downward radiation modes. The ratio of upward and downward power depends on round-trip phase in the buried oxide layer and thus on the emitting angle and the thickness of the buried oxide. For the given emitting angle we can assume the ratio is fixed and that the upward power, ${u_{rad}}^2$, is proportional to the power loss of the guided mode. The targeted emitting profile is $u_{rad} \propto \exp(-z^2/w^2)$, where w is the waist of the Gaussian function. Therefore,

$$\frac{du^2}{dz} \propto u_{rad}{}^2 \propto \exp(-2z^2/w^2). \tag{5-5}$$

Considering an input power $u^2(-\infty)=1$ and $u^2(\infty)=0$, u^2 and $\alpha(z)$ can be solved as

$$u^2 = \frac{1}{2}\operatorname{erfc}(\frac{\sqrt{2}z}{w}) \tag{5-6}$$

and

$$\alpha(z) = -\frac{\frac{du^2}{dz}}{2u^2} = \frac{\exp(-\frac{2z^2}{w^2})}{\operatorname{erfc}(\frac{\sqrt{2}z}{w})}, \tag{5-7}$$

where erfc denotes the complementary error function. Fig. 5.7 shows the profiles of the u^2, $\alpha(z)$, and the emitting profiles αu^2, respectively. The grating strength increases monotonically from the beginning of the grating coupler.

The next step is to determine the relation between the width of the air grooves, w_{air},

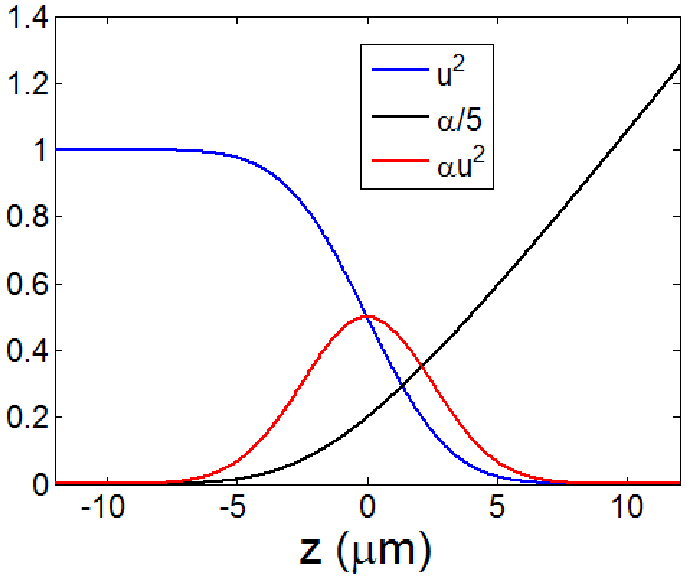

Fig. 5.7. Design of grating couplers for Gaussian emitting profile. (blue) power of the guided mode; (black) grating loss coefficient; (red) emitting profile

and $\alpha(z)$. As we increase w_{air}, the period of the grating has to change, since the propagation constant of the guided mode depends on the duty cycle of the grating. We performed a 2D mode-matching method (MMM) for the x-z plane while taking the y direction as invariant. The 2D MMM is similar to the 3D MMM described in Section 4.3.1 . However, since we need the entire field in the simulation region to monitor the emitting profile, we connect all the fields at different z as linear equations and solve the entire field with a generalized minimum residual method. This method is more time-consuming than a scattering matrix method. We determine the $\alpha(z)$ for a given w_{air} by simulating a uniform grating and plotting the power of the guided mode as it propagates. With the determined $\alpha(z)$, we design a tapered grating coupler based on Eq. (5-7).

We designed the emitting angle at 30° for a wavelength of 1570 nm. The air grooves

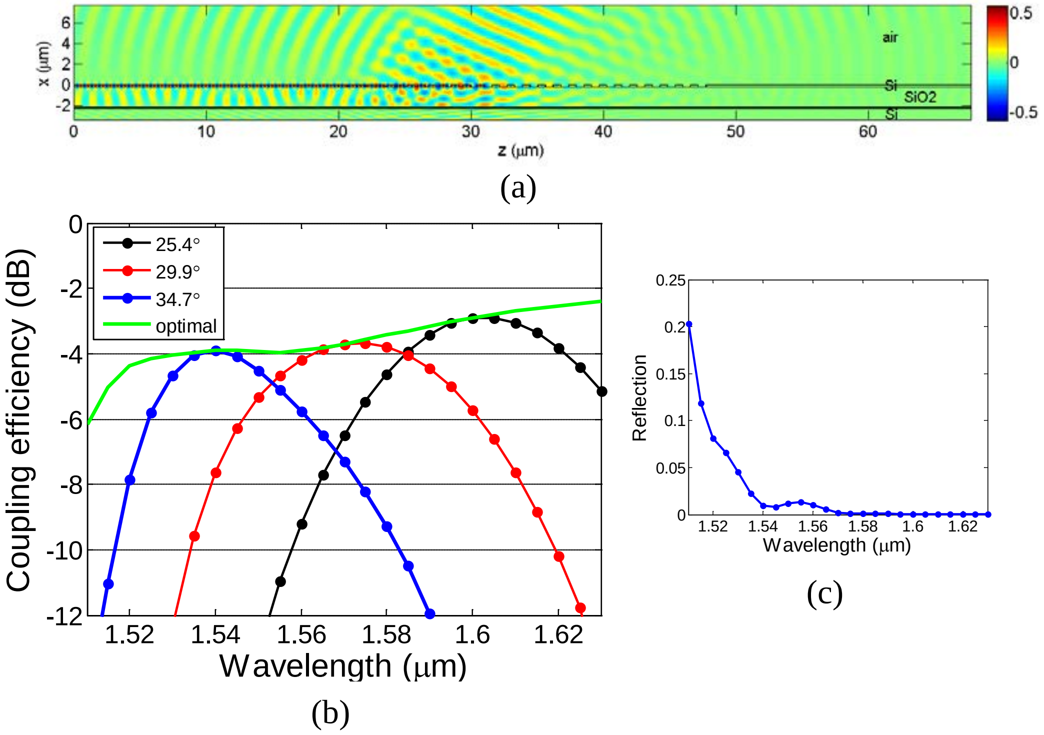

(a)

(b)

(c)

Fig. 5.8. Design of a grating coupler emitting light at 30°. (a) Field distribution. (b) Coupling efficiency to a fiber mode. (c) Reflection as a function of wavelength

are fully etched through the silicon layer. The chosen w_{air} increase monotonically and are 6.8, 12.8, 22.7, 38.6, 74.4, 104.6, 128.8, 149.6, 179.1, 195.4, 220.8, 244.2, 298.7, 422.4 nm, respectively, followed by a uniform grating with $w_{air} = 577\ \text{nm}$. The corresponding periods are 676.2, 681.0, 687.9, 699.0, 724.6, 746.5, 765.0, 781.7, 804.3, 817.3, 838.5, 858.9, 907.8, 1018.2 nm, respectively, followed by a uniform period 1154.0 nm. The field distribution is shown in Fig. 5.8(a) with the input waveguide mode from the left. We monitor the emitting profile at x=3.5 μm. We adjust the position and angle of the fiber mode to obtain maximum coupling between the emitting profile and the fiber mode. The green line in Fig. 5.8(b) shows the optimized coupling efficiency for each wavelength. The maximum coupling efficiency is between −2 and −4 dB except for wavelength around 1510 nm where the third-order grating starts to reflect the mode back. The blue, red, and black lines show the coupling efficiency when the position and angle are fixed at an optimal position for one wavelength. The 1-dB and 3-dB bandwidths are 38 nm and 62 nm, respectively. The emitting angle increases at shorter wavelength, which agrees with Eq. (5-2). Near the shortest wavelength, 1510 nm, the coupling efficiency drops, and the reflection increases, as shown in Fig. 5.8(c). This is because the emitting angle is about

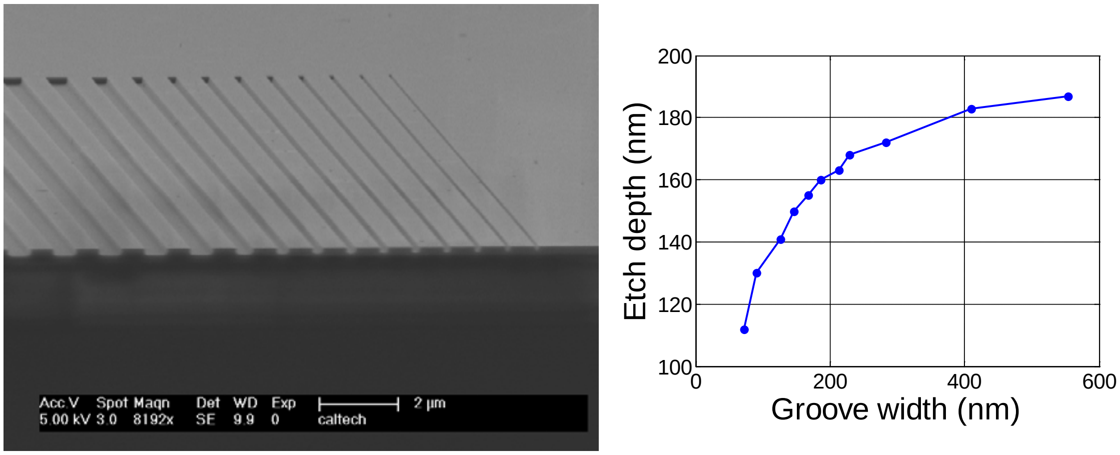

(a) (b)

Fig. 5.9. (a) SEM image of the cross-section of a tapered grating. (b) The measured depths of the grooves versus the widths of the grooves

40° and is a little close to the condition where the third-order Fourier component of the grating reflects the guided mode back.

In the fabrication of the grating couplers, the etching depths of the grooves depend on the aspect ratio. Fig. 5.9(a) shows the SEM image of the cross-section of a cleaved grating. The narrower grooves on the right are shallower than the wider grooves. Fig. 5.9(b) shows the measured groove depth versus w_{air}. As a result, the variable depth as we taper w_{air} has been taken into account. In the modified design, the widths of the grooves are 75, 100, 125, 150, 200, 250, and 300 nm, respectively, each of which is for a group of 6 periods. The w_{air} of the uniform region is 350 nm. The periods are 623, 611, 600, 593, 577, 561, and 545 nm, respectively, for the tapered grating and 526 nm for the uniform grating. The simulation of modified design is shown in Fig. 5.10. The design is for emission at 30° at the wavelength of 1570 nm as well. Due to the shallower grating, the

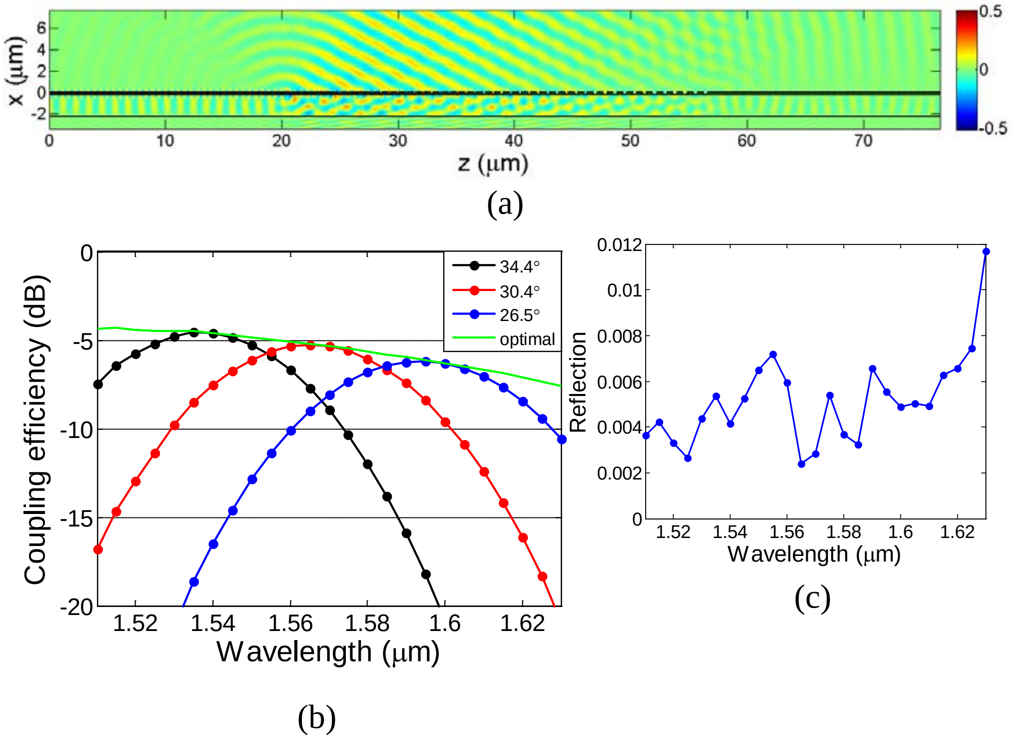

(a)

(b)

(c)

Fig. 5.10. Modified design of grating couplers for aspect-ratio-dependent etching depth. (a) Field distribution. (b) Coupling efficiency to a fiber mode. (c) Reflection as a function of wavelength

emitted field is wider in the longitudinal direction, leading to a lower coupling efficiency of around 5 dB.

Fig. 5.11 shows the transmission spectrum of a reference waveguide with input and output grating couplers. The total insertion loss is about 13.5 dB, corresponding to a coupling loss of 6.75 dB per grating coupler. A slight larger angle with respect to the vertical axis was used, which explained the deviation of the peak wavelength. Shown in the inset is the close-up near the peak of the spectrum. The oscillation amplitude is as low as 0.3 dB. There are also oscillations with a period of approximately 4 nm. The reason is unknown at this point and could be from some kind of multi-mode beating.

5.2 Fabrication of Grating CROWs on Silicon Waveguides

We fabricated grating-defect resonators and CROWs on silicon-on insulator (SOI) wafer, which features a 220-nm-thick silicon layer on top of a 2.0-μm-thick buried oxide layer (BOX). The process flow is shown in Fig. 5.12. Samples were first cleaned in PG

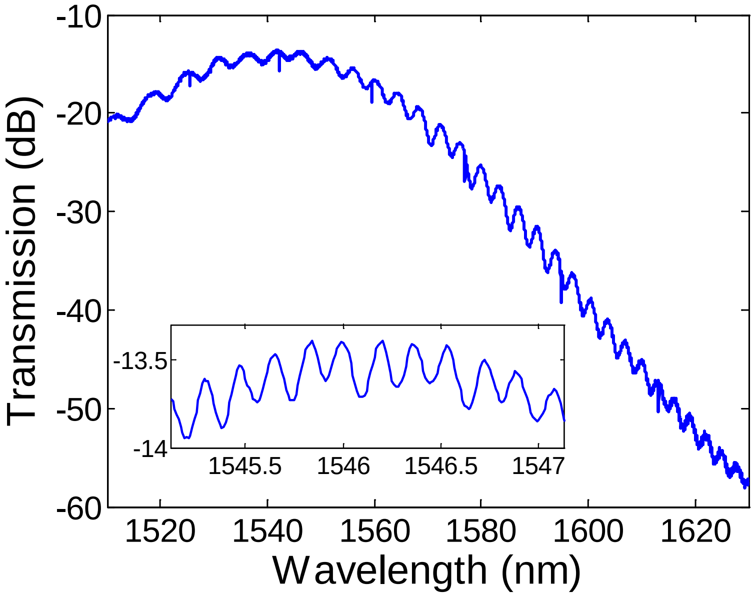

Fig. 5.11. Transmission spectrum of a waveguide with input and output grating couplers. Inset: Close-up of the transmission spectrum

remover at 70 ~ 80℃ for 30 minutes followed by piranha solution (H_2SO_4:H_2O_2 = 3:1) for 10 ~ 15 minutes and a dip in buffered HF for 10 ~ 15 seconds. We spun on e-beam resist ZEP520A at 5000 RPM, which produces a resist thickness of 350 ~ 370 nm. The samples with resist were baked on a hot plate at 180℃ for 10 minutes.

We used a Vistec/Leica EBGP 5000+ e-beam lithography tool at 100 kV. The resolution was 1.25 nm, and the beam step size was 2.5 nm, corresponding to a main field of 160 μm. A current of 300 pA and a e-beam dose of 280 $\mu C/cm^2$ were applied to the holes and a small part of the trench which is 1 μm around the waveguide. The major part of the trench (5 μm wide) was written with a current of 1.6 nA and a dose of 250 $\mu C/cm^2$ to reduce the total writing time (a bulk-sleeve method). The holes and the waveguides were over-exposed with the dose, which leads to larger holes and narrower waveguides. We chose to do over-exposure for obtaining smoother sidewalls. As a result, a negative bias of the hole radii and a positive bias of the waveguide width were applied to compensate for the over-exposure. The holes in the mask were 80% of the targeted values, and the waveguide width is 90 ~ 100 nm larger than the targeted width.

The developed samples were then dry etched using inductively-coupled-plasma reactive ion etching (ICP RIE) with a SF_6/C_4F_8 chemistry. Prior to the dry etch, a 5-second oxygen etch was performed to smooth the sidewall of the resist. The flow rates of SF_6 and C_4F_8 were chosen as 35 and 45 sccms, respectively, for slightly isotropic etch and thereby reduction of line-edge roughness on the sidewall. The ICP power was 1200 W, and the RF forward power was as low as 7 W, corresponding to a DC bias of 35 ~ 40 V. The low DC bias voltage reduces the chance of mask erosion. The combination of smallest beam step size, over-exposure, oxygen etch, optimized flow-rate ratio, and low DC bias leads to smooth sidewall of holes and waveguides and is important of high-Q resonators. The etch rate was approximately 350 nm per minute. To enable the selective

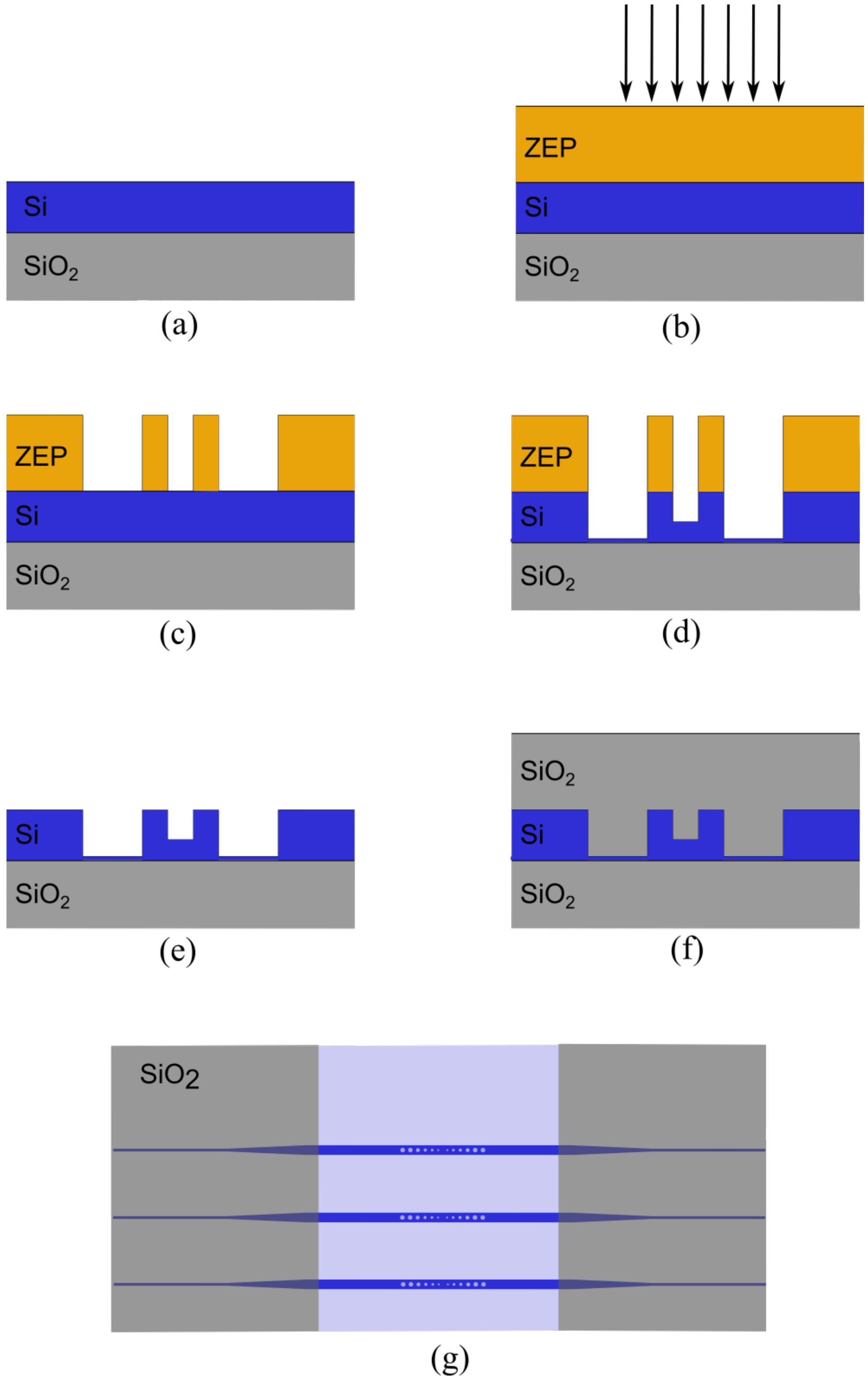

Fig. 5.12. Process flow of the fabrication of grating CROWs on SOI wafers. (a) Original wafer structure. (b) Resist spin-on and e-beam exposure. (c) Development of resist. (d) Si dry etch. (e) Removal of resist. (f) Deposition of SiO_2. (g) A top view of the final device

back-etch as described in Section 5.1.1 and shown in Fig. 5.1(d), the targeted etch depth was 205 ~ 215 nm.

After the dry etch, a 2-μm-thick SiO_2 layer was deposited using plasma-enhanced chemical vapor deposition (PECVD) for spot-size converters. Photo-lithography with two layers of resists (LOR 5B followed by S1813) was performed to selectively remove the oxide on top of the devices, as shown in Fig. 5.12(g). A top image of the final device is shown in Fig. 5.13(a) where the oxide in the center region has been removed. Fig. 5.13(b) and Fig. 5.13(c) show the microscope and SEM images of the boundary of the oxide etch respectively. There are "tunnels" at the waveguide and at the boundary of the trenches. The tunnels are due to unfilled gaps at the boundaries during the deposition of the oxide, which lead to faster etch.

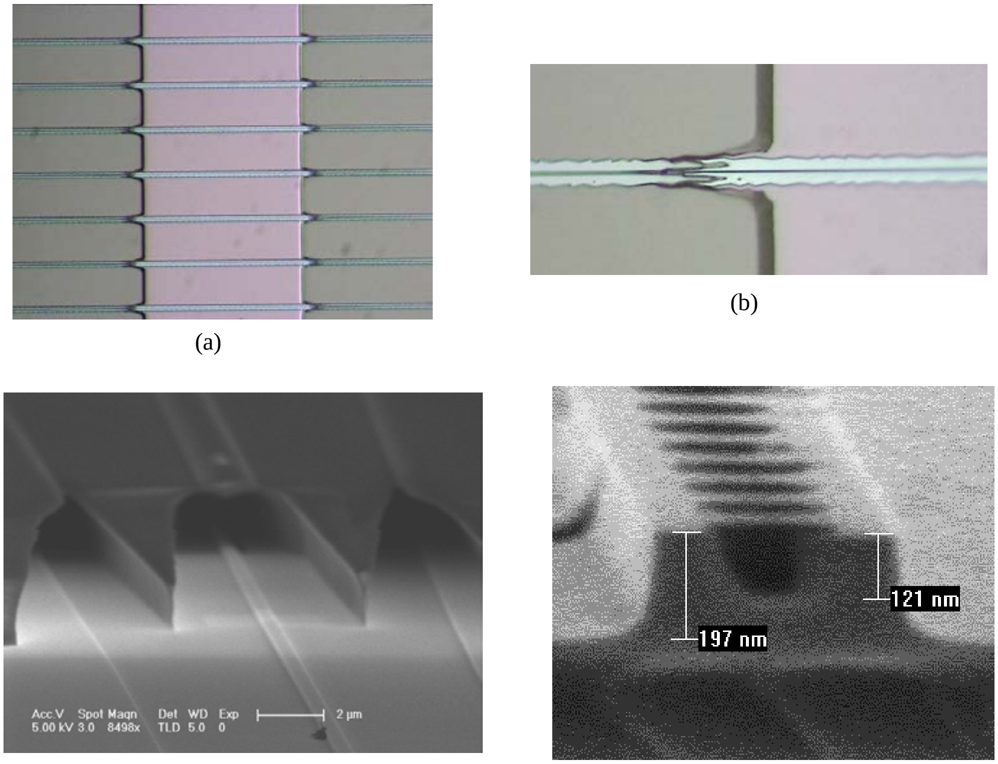

(a) (b) (c) (d)

Fig. 5.13. (a) Microscope top image of the final device after oxide back-etch. (b–c) Microscope and SEM images of the boundary of the oxide back etch. (d) Cross-section SEM image of the hole and the waveguide

Fig. 5.13(d) shows the cross-section of the waveguide and the holes. Due to the Si under-etch for the spot-size converters, the holes are shallower than the designed value. The shallower depth in the holes compared to the depth of the trenches is due to the aspect-ratio dependence of the etch. The depths of the holes were estimated to be 130 nm based on the SEM images and the grating strength derived from the experimental results. We redesigned the tapered grating-defect resonators based on the adjusted hole depth. The new radii of the 6 tapered holes are 46.5, 57.5, 66.5, 74.2, 80.4, and 86.3 nm, respectively, while the radius of the regular holes remains 100 nm. The periods are 357.5, 362.5, 367.5, 370, 375.5, 377.5 nm, respectively, and the period of the regular holes is 385 nm. To compensate for the over-exposure of the e-beam, the radii of the e-beam mask are 80% of the designed values.

Fig. 5.14(a) shows a SEM image of a tapered grating-defect resonator with six tapered holes and two regular holes on each side of the defect. Fig. 5.14(b) shows an N=6 Butterworth CROW with m=14. The coupling coefficients are tailored so that the number of holes is the most in the center of the CROW and the fewest at the end of the CROW.

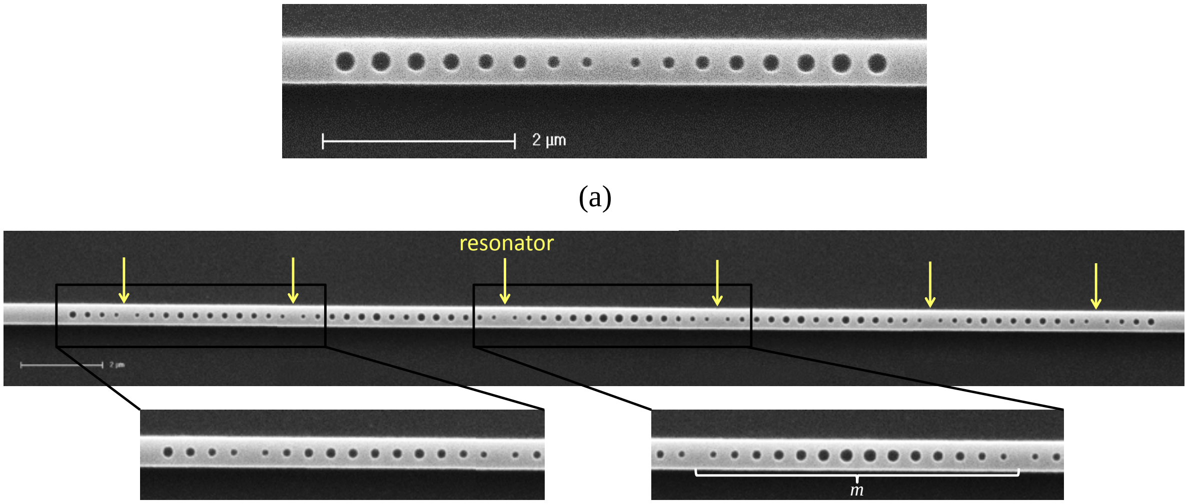

(a)

(b)

Fig. 5.14. SEM images of (a) a tapered grating-defect resonator and (b) an N=6 Butterworth CROW and the close-ups of the defects and the inter-defect sections

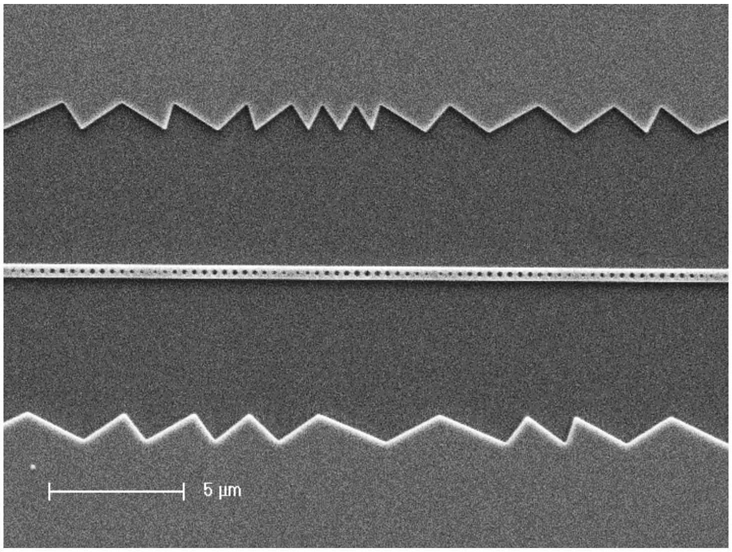

Fig. 5.15. SEM image of the grating resonators and the trenches with random corrugation

The length of the entire CROW is 26.5 μm.

The transmission of CROWs at frequencies outside the CROW band is ideally very low, say −100 dB. However, the measured transmission outside the CROW band can be as high as −20 dB. This is mainly due to part of the input power coupling into the leaky modes confined by the boundary of the trenches. To increase the loss of the leaky modes, we introduce random corrugation on the boundary of the trenches, as shown in Fig. 5.16. The amplitude of the corrugation is 1 μm, and the periods are random and uniformly distributed between 0.2 and 2.5 μm. With the corrugation, the transmission outside the CROW band has been reduced to −40 dB.

5.3 Measurement of Transmission and Group Delay

Fig. 5.16 shows the experimental setup for the measurement of transmission and group delay. We used a Santec TSL-510A tunable laser whose tuning range is from 1510 nm to 1630 nm. The input light from laser is collimated by a fiber collimator and focused by an objective with a NA of 0.65 to a 2 μm big beam spot. A polarization controller and a

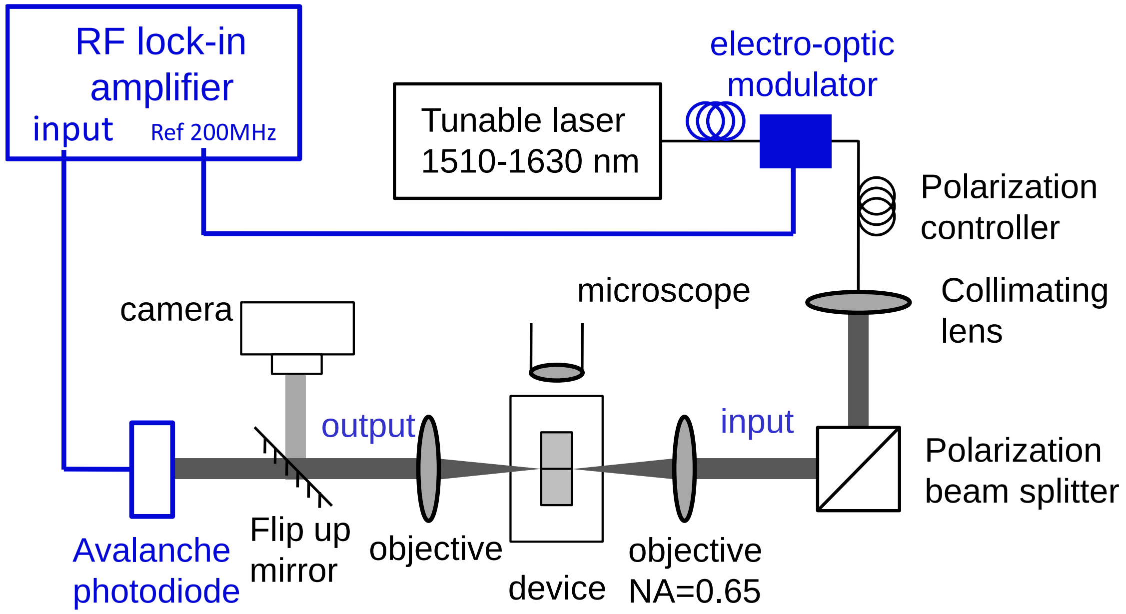

Fig. 5.16. Experimental setup for the measurement of transmission and group delay

polarization beam splitter are used to select the TE polarization. The focused spot couples into the devices with spot-size converters. At the output of the devices, another objective collects and images the output on a camera. The image in the camera is very useful in aligning the waveguide with the input beam. After seeing the waveguide mode at the output, we switch from camera to a photodetector to measure the power and optimize the coupling of light. The laser and the photodetector are controlled by Matlab in a computer via GPIB. The transmission spectra of the devices are obtained by sweeping the wavelength of the laser and are normalized with the output power of a reference waveguide.

The spectra of group delay were measured with a phase-shift technique [40]. As shown in Fig. 5.16, we modulated the intensity of the input light with a 200 MHz RF signal generated from a RF lock-in amplifier (SR844). The output light was collected with a Fujitsu high-speed (2.5 GHz) InGaAs avalanche photodiode (APD) for converting photons to electrons and amplification of signal through avalanche multiplication. The detected signal was sent to the lock-in amplifier to measure the phase difference between the reference and the output RF signal. An optical isolator was inserted before the APD to remove backreflection from APD. We measured the phase shifts for the devices and reference waveguides, respectively. The group delay due to the devices can be obtained via

$$\tau = \frac{\theta_d - \theta_{ref}}{360^\circ} \frac{1}{f_{\mathrm{mod}}}, \tag{5-8}$$

where θ_d and θ_{ref} are the phase-shifts of the device and the reference waveguide, respectively, and f_{mod} is the modulation frequency. For $f_{\mathrm{mod}} = 200\ \mathrm{MHz}$, a phase difference of 1° corresponds to a group delay of 13.9 picosecond. The accuracy of the phase measurement is therefore very important for group delay of picoseconds.

The group delay induced by the APD depends on its multiplication factor *M*, which is controlled via a reverse bias voltage V_r. A larger *M* corresponds to a large delay during the multiplication process. As we increase the input power, *M* gradually decreases due to saturation. Therefore, the group delay induced by the APD depends on the power and is a nonlinear effect. A calibration of the APD needs to be performed before measurement for the choice of an appropriate V_r. A large *M* leads to a strong nonlinear effect while a too small *M* leads to a small signal-to-noise ratio. We chose V_r around 41 V for a balance between nonlinear effect and signal-to-noise ratio. A calibration of a delay versus optical power curve is necessary to correct the nonlinear effect.

5.4 Measurement Results

Fig. 5.17 shows the transmission spectrum of a reference waveguide with a SiO_2 SSC as shown in Fig. 5.1(d). The transmission is defined as the power measured by the detector at the output divided by the power in the input fiber, i.e., including the input and output couplers. The average insertion loss is 7.4 dB, and the amplitude of the Fabry-

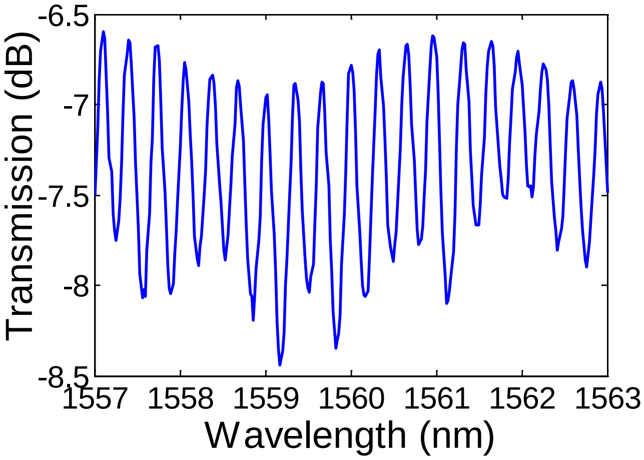

Fig. 5.17. Transmission spectrum of a reference waveguide

Perot oscillations due to reflection at the facets is approximately 1 dB. The transmission spectra shown in this section are normalized with the transmission of the reference waveguide.

5.4.1 Quality Factor of Tapered Grating-Defect Resonators

We measured the transmission spectra of single tapered-grating resonators with 6 tapered holes. A SEM image of a single resonator is shown in Fig. 5.14(a). The transmission peaks were fit with Lorentzian functions, and the Q is obtained as $\lambda/\Delta\lambda$,

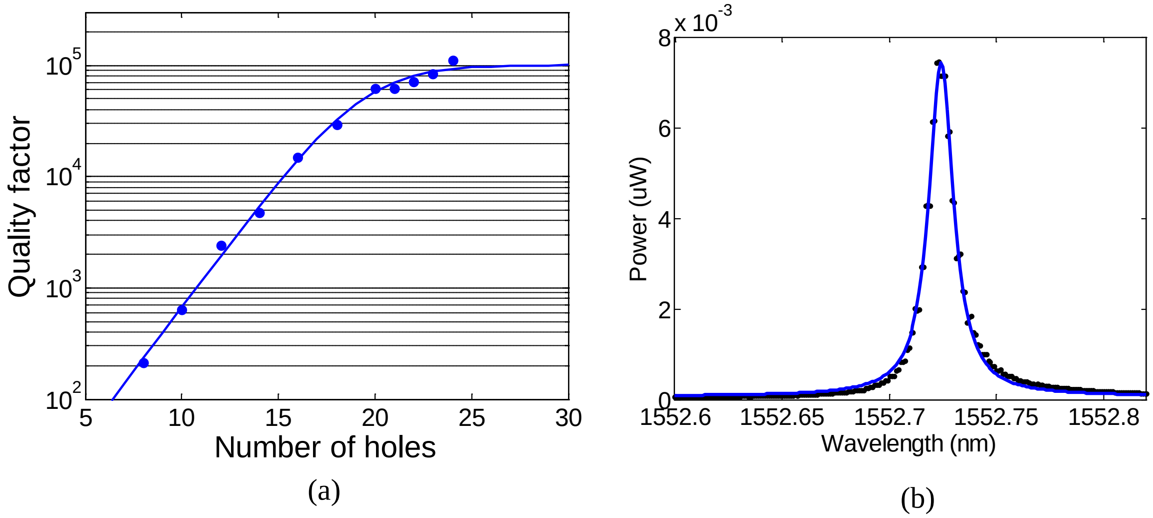

Fig. 5.18. (a) Quality factor a function of n. (b) Transmission spectrum of a grating-defect resonator with n=24 and Q=1.13×10^5

where $\Delta\lambda$ is the full width at half maximum (FWHM) of the Lorentzian function.

Fig. 5.18(a) shows the measured Q as a function of n, the number of holes on each side of the defect. Q increases exponentially at lower n and saturates at the intrinsic Q of the resonator. We fit the curve with

$$\frac{1}{Q(n)} = \frac{1}{Q_i} + \frac{1}{Q_e(n)}, \tag{5-9}$$

where Q_i is the intrinsic Q and $Q_e(n) = Q_0 \cdot a^{2n}$ is the external Q, according to Eq. (4-15). The obtained Q_i is 1.01×10^5, and a=1.30. Since $a \equiv \exp(\kappa_g \Lambda)$, we obtain $\kappa_g = 0.689/\mu\text{m}$ for the regular holes, about half of the value shown in Fig. 4.4 since the holes are much shallower. Fig. 5.18(b) shows a transmission spectrum of a resonator with n=24. The linewidth $\Delta\lambda$ is 13.7 pm, corresponding to a Q of 1.13×10^5.

5.4.2 Butterworth Grating-Defect CROWs

The coupling coefficients of the N=6 Butterworth CROW shown in Fig. 5.14(b) are $(1/\tau_{e1}, \kappa_1, \kappa_2, \cdots, \kappa_5, 1/\tau_{e2})/B$ =(1.932, 1.169, 0.605, 0.518, 0.605, 1.169, 1.932). These coupling coefficients were converted to n_{reg} based on Eqs. (4-16) and (4-17). We chose the bandwidth parameter B so that n_{reg} is equal to 2 in the middle of the CROW (m=14). The numbers of regular holes are $(-1.76, -1.41, 1.35, 2.00, 1.35, -1.41, -1.76)$. A negative n_{reg} means that the number and size of the tapered holes are reduced, as can be seen in the first and second grating sections of Fig. 5.14(b).

Fig. 5.19(a) shows the transmission spectrum of the N=6 Butterworth CROW. The passband is 12 nm wide and the amplitude is flat, with 1.5 ~ 2 dB oscillations, as shown in the close-up (Fig. 5.19(b)). The period and amplitude of the oscillations are similar to the Fabry-Perot oscillations of a reference waveguide, as shown in Fig. 5.19(c). Therefore, we can conclude that the oscillations in the passband are mainly due to the reflection at

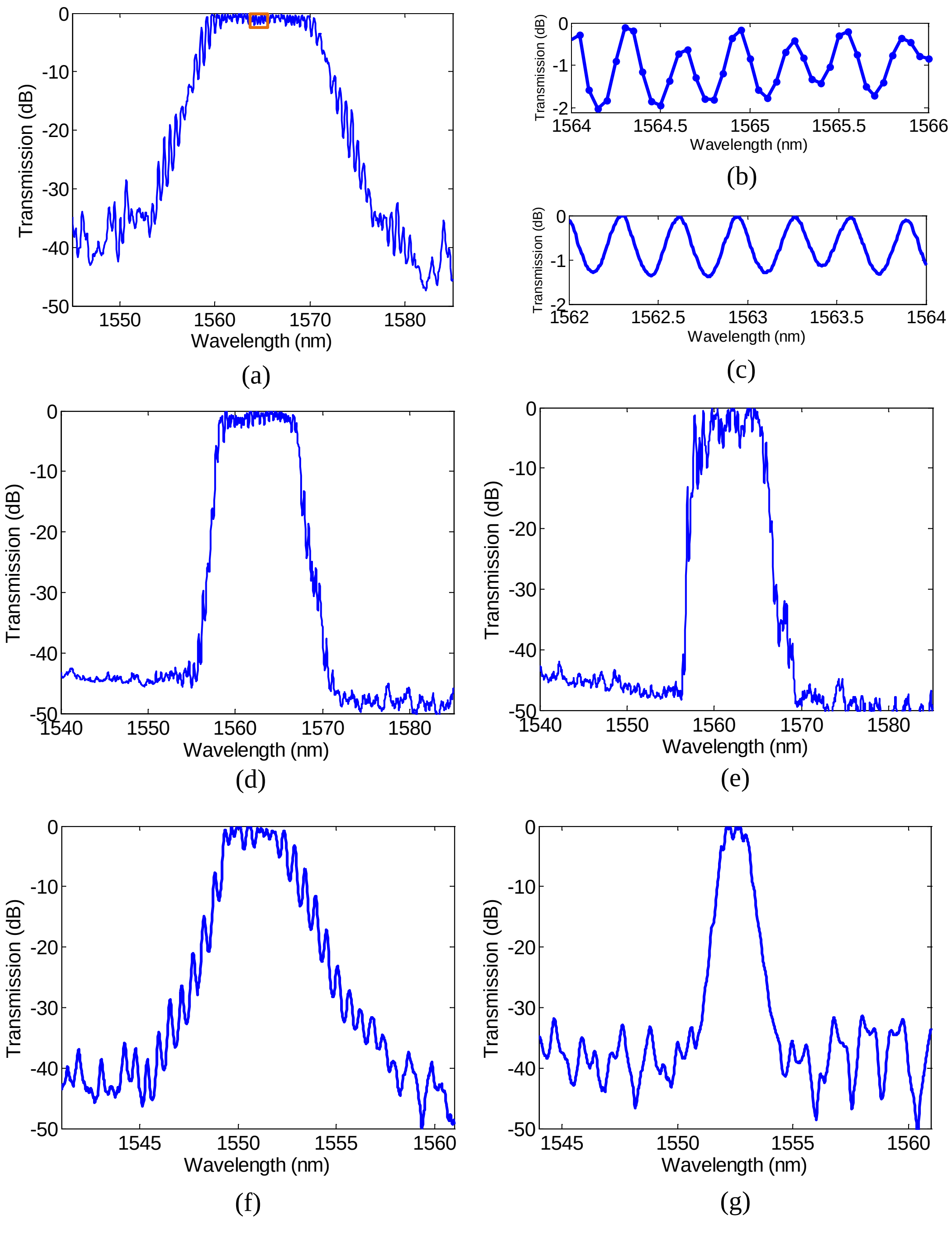

Fig. 5.19. (a) Transmission spectrum of an *N*=6 Butterworth CROW with *m*=14. (b) Close-up of the oscillation in the passband in (a). (c) Fabry-Perot oscillation of a reference waveguide. (d–g) Transmission spectrum of (d) an *N*=24 Butterworth CROW with *m*=14, (e) an *N*=36 Butterworth CROW with m=14, (f) an *N*=8 Butterworth CROW with *m*=18, (g) an *N*=4 Butterworth CROW with m=22

the facets. At the band edge, the transmission decays exponentially (linearly in the dB scale), which agrees with the property of Butterworth filters.

Fig. 5.19(d) and Fig. 5.19(e) show the transmission spectra of m=14 Butterworth CROWs with 24 and 36 resonators, respectively. The bandwidth does not change with the number of resonators, and the roll-off at band edge becomes steeper with more resonators. The oscillations at the passband are larger for 36 resonators and are due to the effect of fabrication disorder. Fig. 5.19(f) and Fig. 5.19(g) show the transmission spectra of an N=8 Butterworth CROW with m=18 and an N=4 Butterworth CROW with m=22, respectively. As m increases and thus the coupling coefficients decrease, the bandwidths

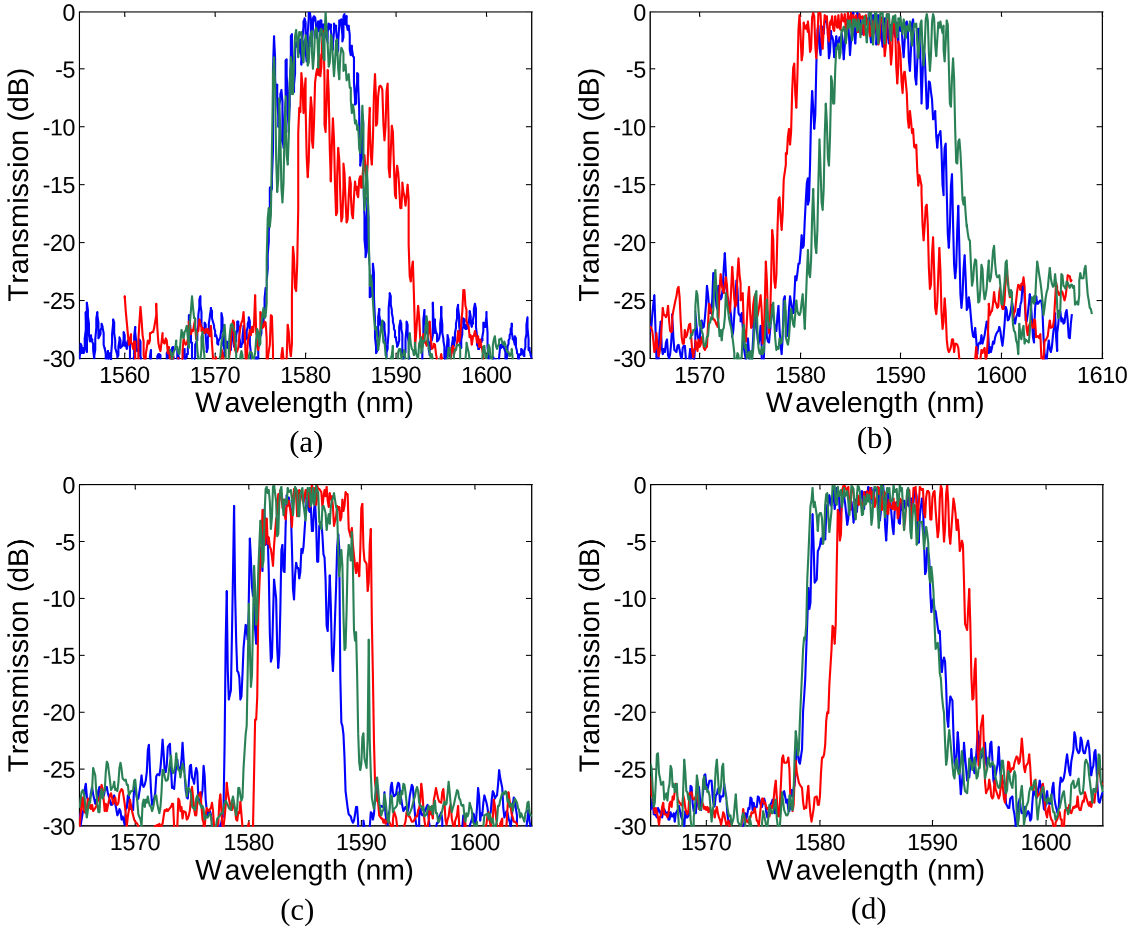

(a)

(b)

(c)

(d)

Fig. 5.20. Measured transmission spectra of three m=14 CROWs with identical design for (a) N=6 Uniform CROWs, (b) N=6 Butterworth CROWs, (c) N=10 Uniform CROWs, and (d) N=10 Butterworth CROWs

dropped to approximately 3 nm and 1 nm for m=18 and m=22 respectively.

5.4.3 Robustness of Butterworth CROWs

In the measurement we observed that Butterworth CROWs are more robust against fabrication disorder than CROWs with uniform coefficients. We measured the transmission spectra of several CROWs with identical design and overlapped their spectra on the same figure. Fig. 5.20 shows the measured spectra for m=14 CROWs with uniform coupling and Butterworth design, respectively. The spectra of Butterworth CROWs are similar and consistent, while the spectra of uniform CROWs vary a lot. Besides, the passband oscillations of some uniform CROWs are larger than 10 dB. Therefore, Butterworth CROWs are more robust than uniform CROWs. According to the disorder analysis in Section 2.7, the disorder of resonant frequency is the dominant disorder loss, which agrees with the analysis for grating-defect CROWs shown in Section 4.7.

5.4.4 Group Delay of Grating-Defect CROWs

We measured the spectra of group delay with the method described in Section 5.3 . The spectra of transmission and group delay for Butterworth CROWs with m=14, 18, and 22, respectively, are shown in Fig. 5.21. The reflection at the facets causes oscillations in the group delay spectra, and the oscillating amplitude is typically a few picoseconds. We smoothed out the oscillations with a moving average method. We verified in the simulation that the moving average method successfully recovers the distorted spectra to the original spectra without reflection at the facets.

The measured group delay is smaller at the band center and increases as the frequency approaches the band edge, which agrees with the dispersion curve of CROWs (Fig. 2.1). We took the average of the group delay over the center half of bandwidth as the group delays of the CROWs. The group delays of the three CROWs in Fig. 5.21 are 6.79, 9.02,

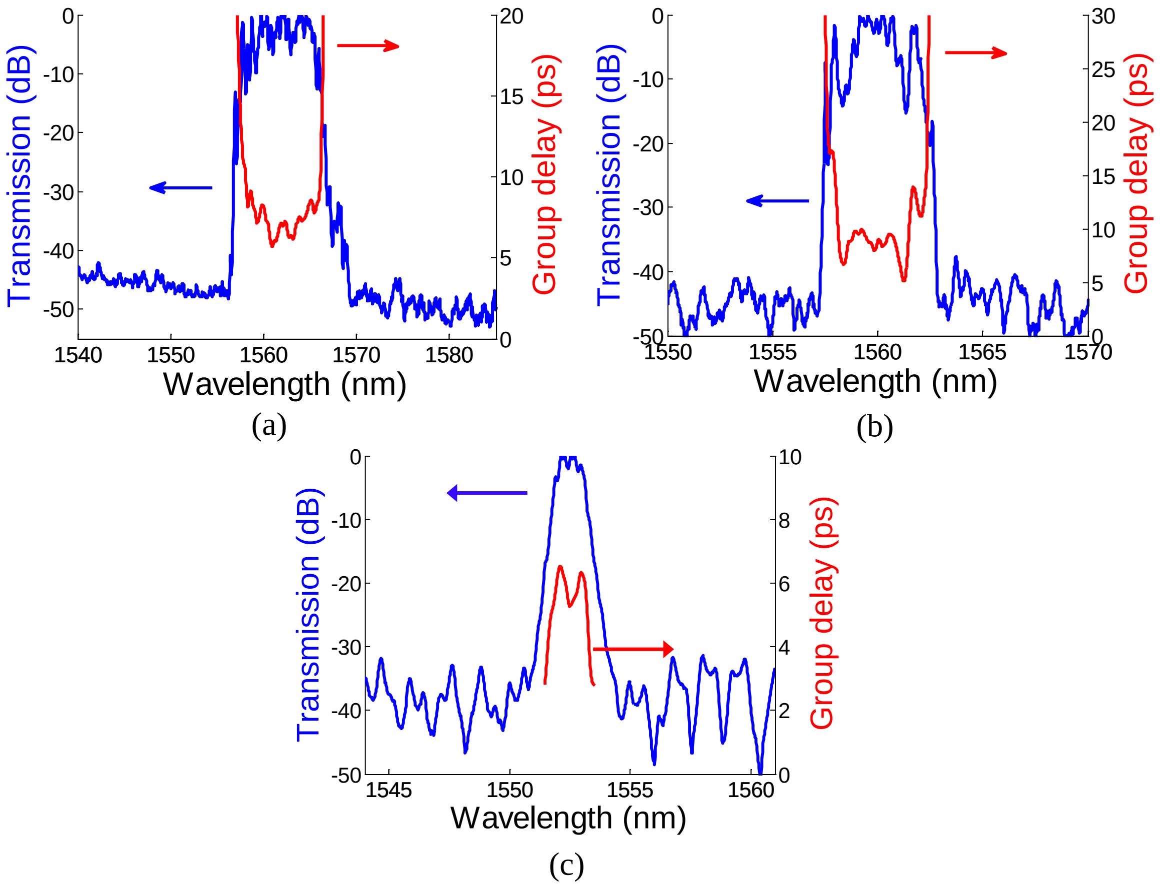

(a) (b) (c)

Fig. 5.21. Spectra of transmission and group delay for (a) an *N*=36 Butterworth CROW with *m*=14, (b) an *N*=20 Butterworth CROW with *m*=18, and (c) an *N*=4 Butterworth CROW with *m*=22

and 5.98 picoseconds, respectively. Considering the lengths of the CROWs which are 175.1, 116.5, and 30.9 μm, respectively, the group indices of the CROWs are 11.6, 23.2, and 58.1, respectively.

Fig. 5.22 shows the group delay versus the number of resonators for CROWs with *m*=14, 18, and 22, respectively. For every given *m*, group delay is a linear function of *N*. We fit the data with lines and obtained the group indices from the slope of the lines. The group indices for *m*=14, 18, and 22 are 12.8, 25.3, and 49.0, respectively. The standard deviation of group delay for given *m* and *N* is smaller than 1 ps. The three curves show a reliable control of group velocity via *m*.

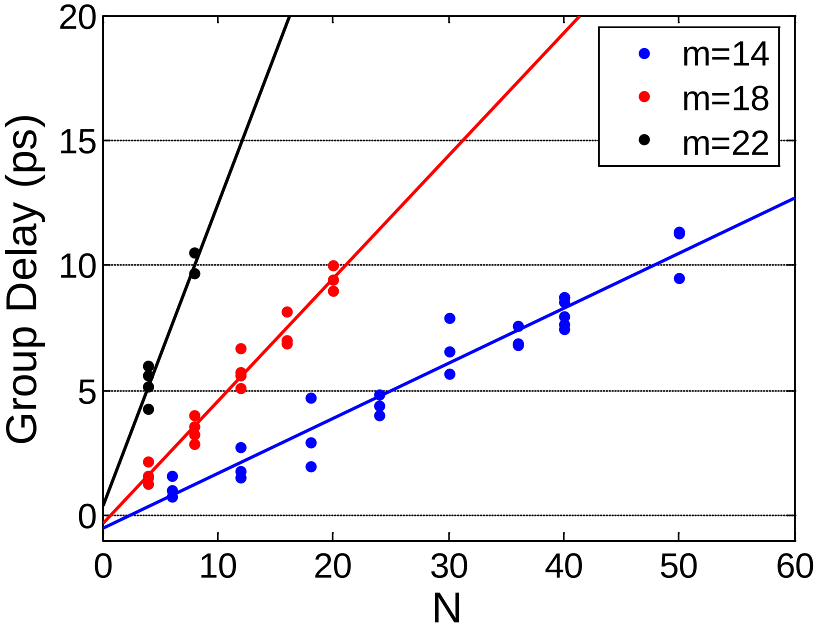

Fig. 5.22. Group delay versus N for CROWs with *m* = 14, 18, and 22, respectively

The maximum numbers of resonators, $N_{\max}$, for *m*=14, 18, and 22 are approximately 50, 20, and 8. The yield decreases as we increase the number of resonators, as presented in Fig. 2.12(c) where the disorder loss increases with *N*. The dependence of $N_{\max}$ on the bandwidth leads to a maximum group delay around 10 ps for the three different *m*. This agrees with the simulated results in Fig. 2.12(c) where the achievable group delay is flat over a wide range of bandwidth.

Chapter 6

CROWs Based on Bandgap-Modulated Grating Resonators

6.1 Introduction

The grating-defect CROWs introduced in Chapter 4 possess short resonator lengths, small modal volume, and convenient control of inter-resonator coupling – all because they are designed to resonate at the Bragg wavelength of the grating. However, there are two drawbacks of these resonators. First, the ultra-small modal volume leads to high sensitivity to fabrication disorder, as discussed in Section 4.7 . Second, fabrication of the tapered holes (the smallest one is 41.5 nm in radius) is challenging. Moreover, further increasing the theoretical Q requires more tapered holes, which will correspond to even smaller holes.

Recently, it has been demonstrated in both theory and experiment that a smooth modulation of 1D or 2D periodic structures can create resonances with high quality factor [53, 54, 61-64]. Rather than a physical defect cavity, varying the period or the size of the holes creates an “extended” defect. Modulation of the unit cells leads to a spatially-modulated grating band gap, and the resulting resonant mode is smooth in space and narrow-band in the spatial frequency domain. Therefore, the Q reported in the literature is typically $10^7 \sim 10^8$ in theory. Since this kind of high-Q resonator does not require fabrication of very small holes, they can be more robust.

In this Chapter, we introduce the theory of bandgap-modulated grating resonators, including the coupled-mode theory and 3D simulations. As discussed in Section 4.4 , since the resonant frequencies are near the grating band edge, an additional phase section is required for the coupling between resonators. We will show the importance of the phase sections in this chapter. Finally, the experiment of bandgap-modulated resonators is presented.

6.2 Coupled-Mode Formalism

Fig. 6.1(a) shows a schematic drawing of a bandgap-modulated resonator based on a grating on a silicon waveguide. The radii of the holes are identical, whereas the periods of the holes are modulated in the middle section and uniform in the end sections. The modulated period leads to a spatially modulated band gap as shown in Fig. 6.1(b). This "extended" defect can support modes whose frequency is outside the band gap in the modulated section and within the band gap in the end sections, shown as the blue line in Fig. 6.1(b). As a result, the resonant mode propagates as a grating band-edge mode in the modulated section and evanesces exponentially in the end sections.

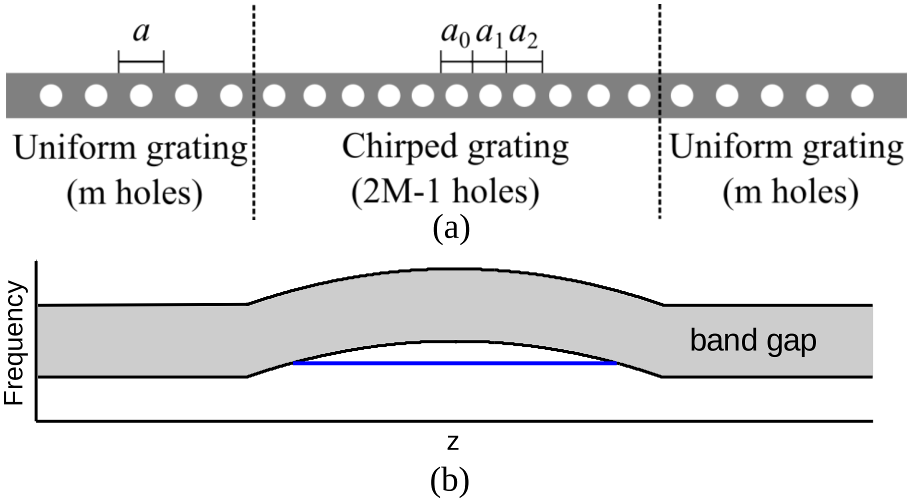

Fig. 6.1. (a) A bandgap-modulated grating resonator. (b) The corresponding spatially-modulated grating bandgap

The modulated grating can be analyzed with coupled-mode equations similar to Eq. (4-1). Since the Bragg frequency varies along the grating, the detuning of propagation constant, δ, becomes a function of z. We write the coupled-mode equations as

$$\begin{aligned} \frac{da}{dz} &= -i[\delta - \delta_B(z)]a + i\kappa_g b \\ \frac{db}{dz} &= i[\delta - \delta_B(z)]b - i\kappa_g a \end{aligned}, \tag{6-1}$$

where $\delta_B(z) \equiv \beta_B(z) - \beta_{B0}$ is the detuning of the propagation constant of the local Bragg condition from a reference propagation constant, defined as the Bragg condition of the uniform grating. $\delta \equiv \beta - \beta_{B0}$ is defined as the detuning of the propagation constant of the input frequency from the reference Bragg condition. Therefore, $\delta - \delta_B(z) = \beta - \beta_B(z)$ is the detuning of propagation constant from the local Bragg condition. The grating strength κ_g is assumed constant for small modulation of the grating.

The transmission spectra and field distribution of the grating resonator can be simulated with Eq. (6-1). The supermodes of the local grating unit cells can be obtained by solving the eigenvectors of the coupling matrix, which leads to

$$\begin{aligned} &\text{propagation constant } K = \pm\sqrt{\left[\left(\delta - \delta_B(z)\right)^2 - \kappa_g{}^2\right]} \\ &\text{supermodes } \begin{bmatrix} a \\ b \end{bmatrix} = \begin{bmatrix} \kappa_g \\ \delta - \delta_B(z) \pm K \end{bmatrix}. \end{aligned} \tag{6-2}$$

The supermodes are propagating if $\left|\delta - \delta_B(z)\right| > \kappa_g$ and exponentially decaying or growing if $\left|\delta - \delta_B(z)\right| < \kappa_g$. We consider frequencies near the lower band edge, i.e., $\delta \approx -\kappa_g$. We express δ as $-\kappa_g + \delta_{be}$, where δ_{be} is the detuning of propagation constant from the band edge of the uniform grating section. If the absolute value of $\delta_{be} - \delta_B(z)$ is much less than κ_g, the frequency is near the local band edge, and the propagation constant of the supermodes can be approximated as

$$K \approx \pm\sqrt{2\kappa_g\left(\delta_B(z) - \delta_{be}\right)}. \tag{6-3}$$

The formula is similar to the wave vector of quantum states in potential wells. An one-dimensional time-independent Schodinger equation is given by

$$-\frac{\hbar^2}{2m}\frac{d^2}{dz^2}\varphi(z)+V(z)\varphi(z)=E\varphi(z), \tag{6-4}$$

where φ is the wave function, $V(z)$ is the potential, E is the eigen-energy, and m denotes the mass of the particle. The wave vector K of the wave function is given by

$$K=\sqrt{\frac{2m}{\hbar^2}\left(E-V(z)\right)}. \tag{6-5}$$

Comparing Eqs. (6-3) and (6-5), we obtain

$$\begin{aligned} E &= -\frac{\hbar^2\kappa_g}{m}\delta_{be} \\ V(z) &= -\frac{\hbar^2\kappa_g}{m}\delta_B(z). \end{aligned} \tag{6-6}$$

δ_{be} represents the energy of the mode, and $\delta_B(z)$ defines the energy potential. Therefore, we can apply the well-developed knowledge of quantum mechanics to the design of bandgap-modulated resonators. As an example, a harmonic oscillator with a quadratic $\delta_B(z)$ will lead to a mode with Gaussian profile, a good function for reducing the

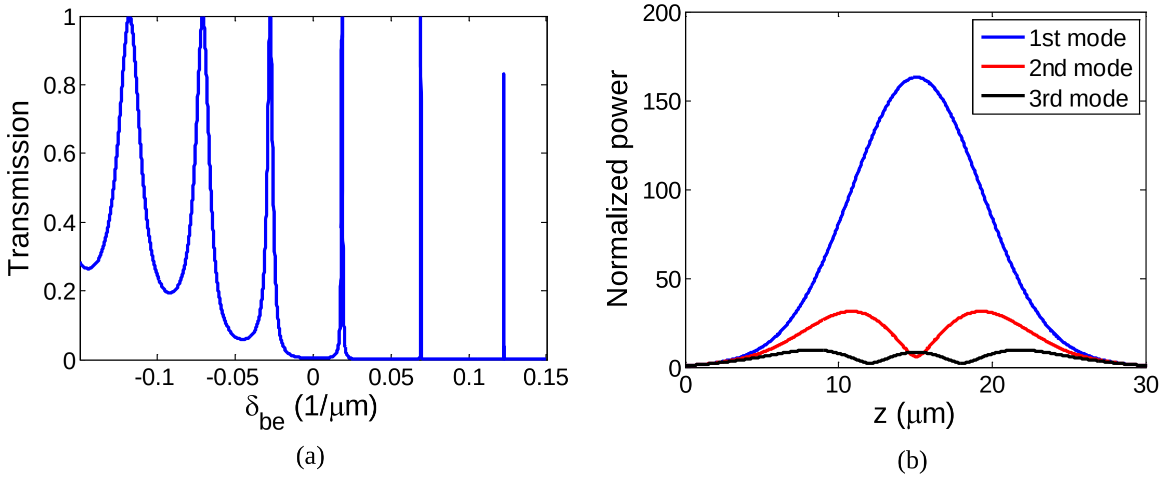

(a) (b)

Fig. 6.2. Transmission spectrum of a bandgap-modulated grating resonator. (b) Field distribution of the three modes.

coupling to the radiation modes.

We simulate a grating with $\kappa_g = 1/\mu\text{m}$. The mirror sections are 5 μm long, and the modulated section is 20 μm long. $\delta_B(z)$ of the modulated section is a quadratic function which is 0.15/μm at the center and 0 at the two ends. $\delta_B(z) = 0$ for the mirror sections. Fig. 6.2(a) shows the transmission spectrum of the resonator. There are three modes confined in the potential well, i.e., between $\delta_{be} = 0$ and 0.15/μm. Modes with $\delta_{be} < 0$ are band-edge modes of the grating. Fig. 6.2(b) shows the field distribution of the three modes. The first mode corresponds to $\delta_{be} = 0.123/\mu\text{m}$, which is the deepest inside the potential well. The field is close to a Gaussian and is the fundamental mode of the resonator. The second and third modes are at $\delta_{be} = 0.0692/\mu\text{m}$ and $0.0186/\mu\text{m}$, respectively. They have two and three lobes, respectively, in the field distribution. The frequency spacings between adjacent modes are about equal, similar to the case of harmonic oscillators.

The number of modes can be controlled with the depth and width of the modulation, $\delta_B(z)$. Increasing the width or depth results in more number of modes. The coupled-mode equations here do not account for radiation modes. The radiation loss can be estimated with Fourier analysis or calculated in 3D simulations.

6.3 High-Q Bandgap-Modulated Resonators

We consider the same waveguide grating used in Section 4. The resonator is shown in Fig. 6.1(a). The silicon waveguides are 490 nm wide and 220 nm thick. The radii of the holes are 100 nm. We chose *a*=362 nm as the grating period of the mirror sections. In the modulated section, the period is decreased to a_0=350 nm with a quadratic modulation. There are 2*M*-1 holes (*M* different periods) in the modulated section and *m* holes in each mirror section. The periods of 362 nm and 350 nm correspond to lower-frequency band

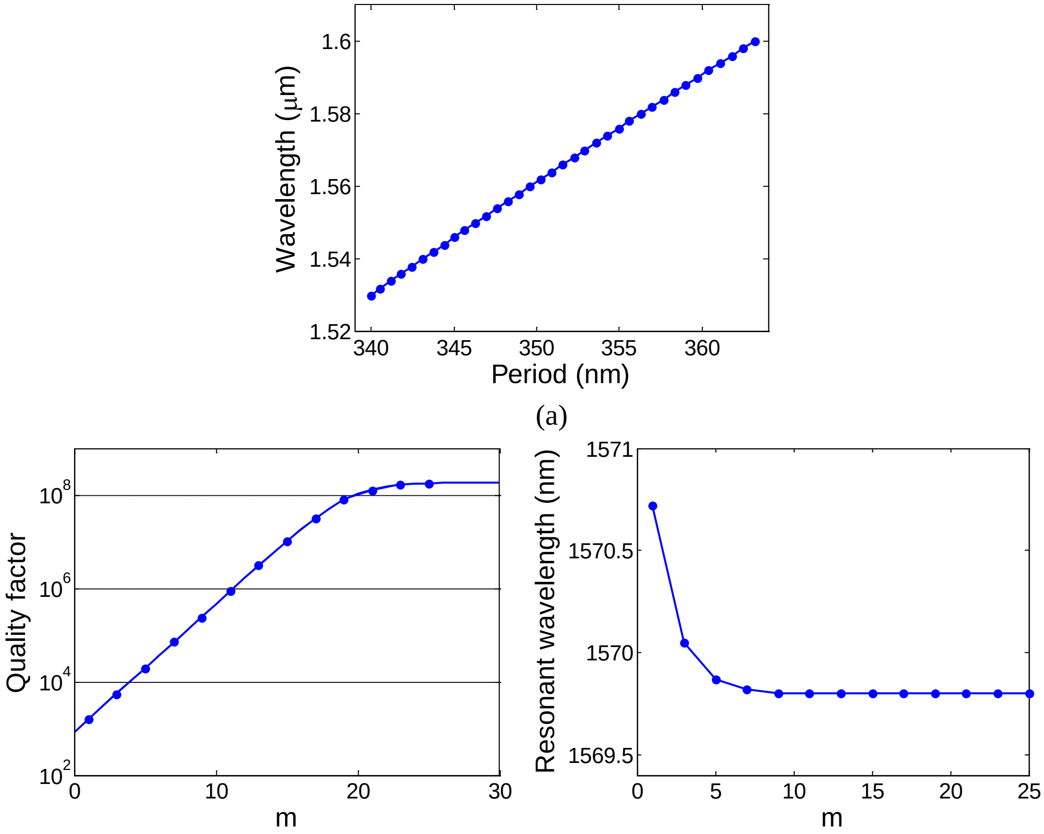

(a)

(b)

(c)

Fig. 6.3. (a) Band-edge wavelength as a function of grating period. (b) Quality factor of the designed bandgap-modulated resonators as a function of *m*. (c) Resonant wavelength as a function of *m*

edges at wavelengths of 1596.5 nm and 1561.2 nm, respectively, as shown in Fig. 6.3(a). As a result, the resonant frequency falls in between the two wavelength and was found to be near 1570 nm.

Fig. 6.3(b) and Fig. 6.3(c) show the quality factor and resonant wavelength as we increase the number of mirror holes, *m*. The intrinsic *Q* is as high as 1.83×10^8. At lower *m*, the external *Q* can be fitted as $Q_e = Q_0 \cdot a^m$, where a=1.88. Compared to grating-defect resonators shown in Section 4, where adding one hole increases the Q by a factor of 3.42, the grating strength of bandgap-modulated resonators is weaker since the frequency is near the band edge. The resonant wavelength also changes with *m*. As *m* increases, the resonant wavelength goes deeper in the potential well and eventually saturates at a value. This is different from the case of grating-defect resonators where the resonant wavelength is always at the Bragg wavelength.

6.4 Coupling Bandgap-Modulated Resonators for CROWs

In Section 4.4, we have discussed inline coupling of resonators. Two resonators coupled via a waveguide are equivalent to two directly coupled resonators. The coupling coefficient depends not only on the individual quality factors but also on the round-trip phase of the coupling cavity, 2θ. The individual resonant frequencies are shifted due to the coupling if 2θ is not equal to π. The formulas for the coupling coefficient and the frequency shift were shown in Eq. (4-12).

We mentioned in Section 4.4 that for CROWs we require 2θ equals π. This can be explained using Fig. 6.4. Fig. 6.4(a) shows a CROW where resonators are coupled via waveguides. The round-trip phases of the coupling cavities are 2θ, and the external loss of each resonator to each waveguide is $1/\tau_e$. According to the derivation in Section 4.4 , the CROW in Fig. 6.4(a) is equivalent to the CROW in Fig. 6.4(b), where resonators are

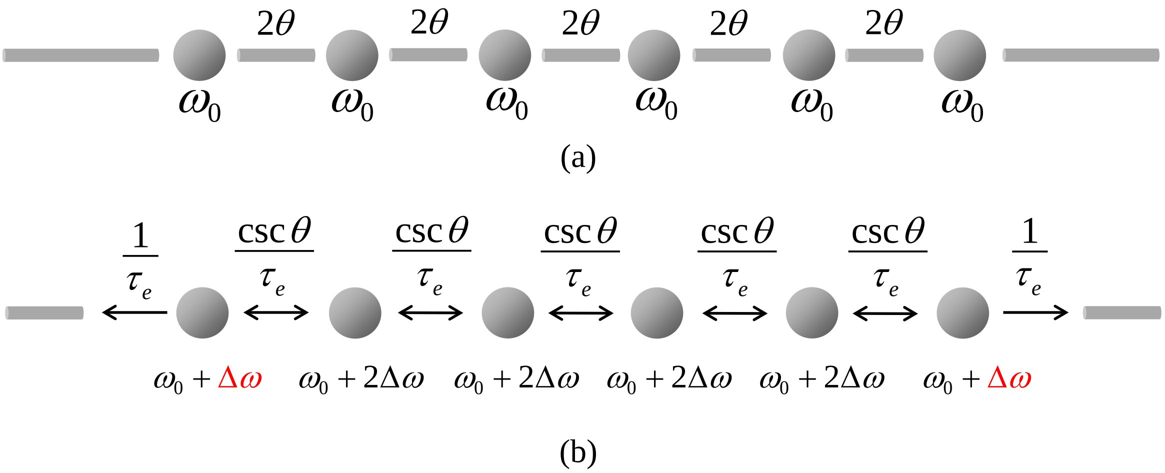

Fig. 6.4. Schematic drawings of (a) indirectly coupled resonators and (b) directly coupled resonators which are equivalent to (a)

directly coupled. The frequency shifts of the resonators depend on the number of resonators they are coupled to. The first and last resonators are shifted by $\Delta\omega = -\cot\theta/\tau_e$, while the rest of the resonators are shifted by $2\Delta\omega = -2\cot\theta/\tau_e$. Resonators with different frequency shifts can distort the CROW spectra. When $2\theta = \pi$, all the frequency shifts are zero and the resonant frequencies are identical. Besides, the inter-resonator coupling coefficient is given by $\csc\theta/\tau_e$, while the external loss to the input and output waveguides are $1/\tau_e$. They are equal only when $2\theta = \pi$.

Fig. 6.5 shows the transmission spectra of 10-resonator CROWs with different 2θ. When $2\theta = \pi$, both the coupling coefficients and the resonant frequencies are uniform, so the spectrum is symmetric and maximally flat (Fig. 6.5(a)). As we increase 2θ, the frequency shift is positive, and the coupling coefficient increases. Therefore, we start to

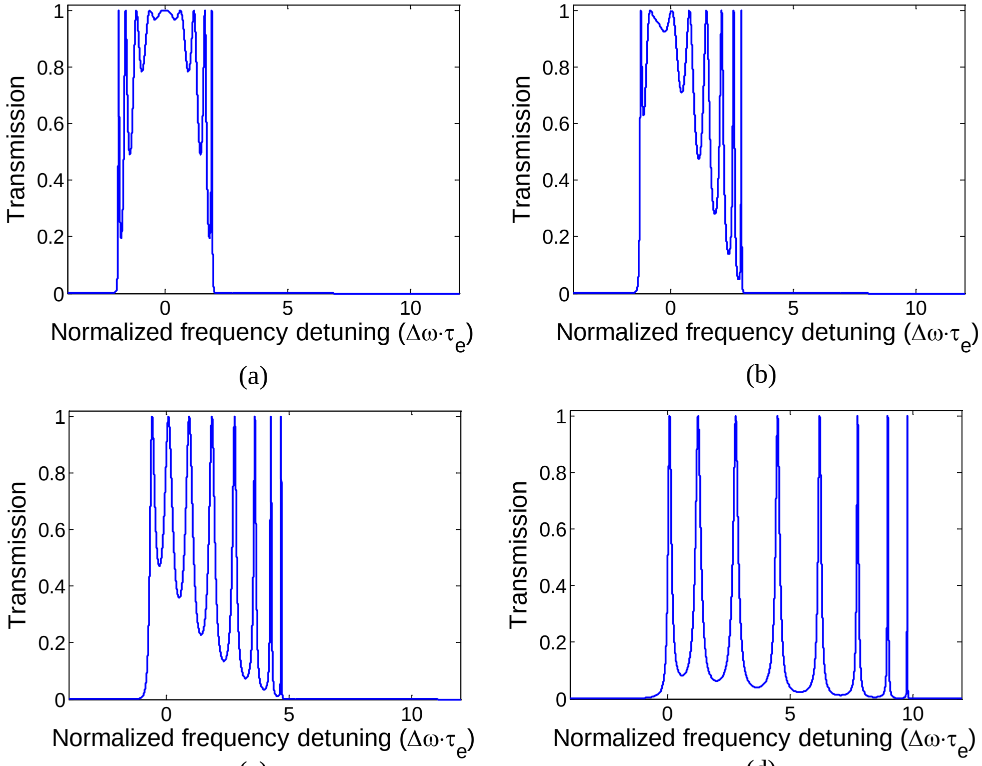

(a)

(b)

(c)

(d)

Fig. 6.5. Transmission spectra of 10-resonator CROWs with 2θ = (a) π, (b) $(5/4)\pi$, (c) $(3/2)\pi$, and (d) $(7/4)\pi$

see the center of the spectra move and the bandwidth become broader (Fig. 6.5(b-d)). Due to the non-uniform resonant frequencies and coupling coefficients, the passband oscillations increase as 2θ increases from π. Therefore, choosing $2\theta = \pi$ for the inter-resonator coupling cavity is important for CROWs.

We consider the round-trip phase for the coupling of grating resonators. Fig. 6.6(a) shows an inter-resonator cavity whose length is *d*. The round-trip phase 2θ consists of the reflection phase from the grating and the propagation phase in the cavity. The single-side reflection phase of the grating is given by $\theta_r = -\pi/2 - \sin^{-1}(\delta/\kappa_g)$. At the Bragg wavelength ($\delta = 0$), $\theta_r = -\pi/2$, and the round-trip phase is exactly $-\pi$. No additional

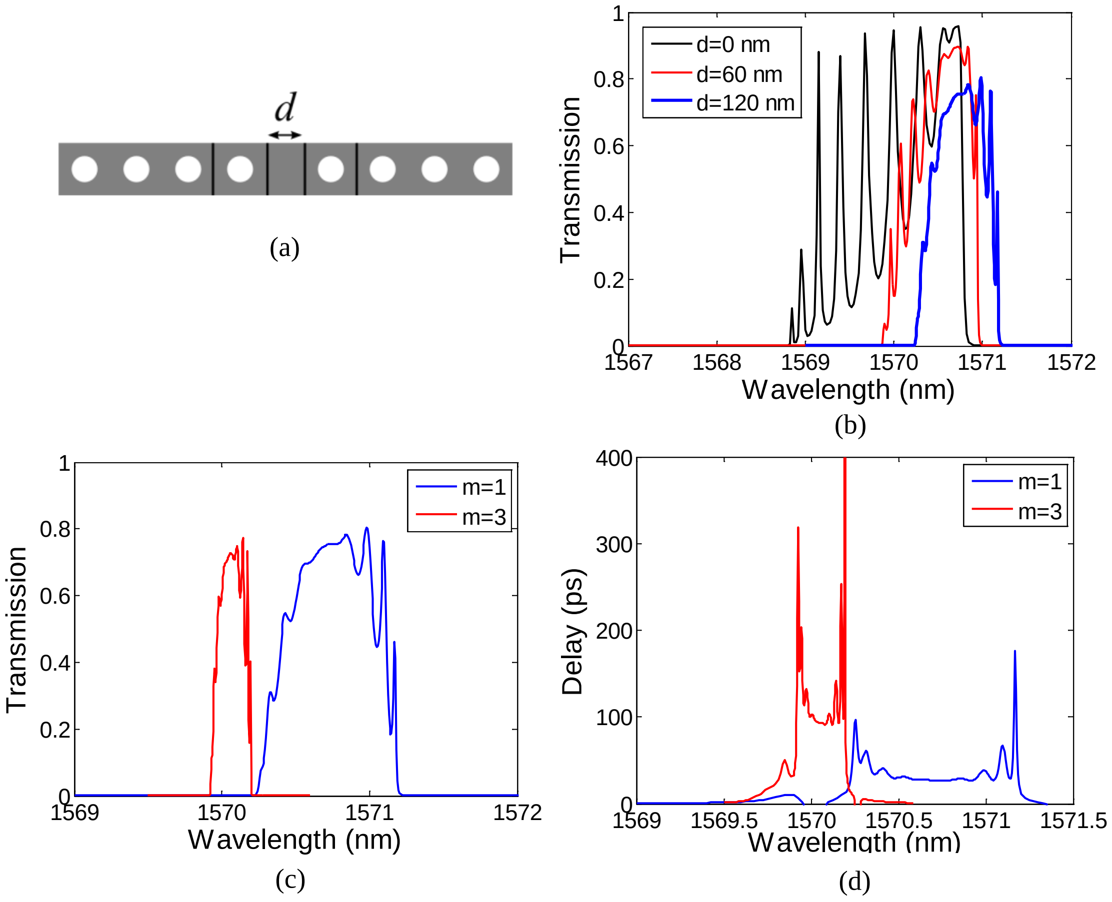

(a)

(b)

(c)

(d)

Fig. 6.6. (a) Schematic drawing of the inter-resonator coupling cavity. (b) Transmission spectra of 10-resonator CROWs with *d* = 0, 60, and 120 nm, respectively (*m*=1). (c–d) Spectra of transmission and group delay for 10-resonator CROWs with *d* = 120 nm and with *m*=1 and *m*=3, respectively

cavity is required for the Bragg wavelength. For the bandgap-modulated resonators which resonates near the band edge ($\delta \approx -\kappa_g$), an addition phase section is required. If we consider $\delta = -0.9\kappa_g$, a phase section corresponding to a phase of $\sin^{-1}(0.9) = 0.36\pi$ is required. Since the effective index of the waveguide is 2.4 for a wavelength of 1570 nm, the phase of 0.36π corresponds to *d*=118 nm.

We simulated the transmission and group delay of CROWs based on bandgap-modulated resonators in 3D simulations. Fig. 6.6(b) shows the transmission spectra of *N*=10, *m*=1 CROWs with *d* = 0, 60, and 120 nm, respectively. The resonant wavelength of a single resonator is at 1570.7 nm. Without the phase section, the spectrum with *d* = 0 consists of large oscillations. The wavelength blue-shifts, and the bandwidth is broad. With *d* = 120 nm, the oscillations are much smaller, and the wavelength does not shift. However, the peak of the transmission is smaller. Fig. 6.6(c) and Fig. 6.6(d) show the transmission and group delay of CROWs with *d* = 120 nm and with different *m* (*m*=1 and 3). With *m*=3, the bandwidth is narrower, and the group delay is larger. The control of coupling coefficients via *m* is similar to the control of coupling coefficient in grating-defect resonators. However, the wavelength changes with *m* in bandgap-modulated CROWs.

6.5 Effect of Disorder on Bandgap-Modulated CROWs

We calculate how deviation of the hole radii affects the resonant frequency. Fig. 6.7 shows the wavelength shift corresponding to 1 nm change of radius for each hole starting from the one at the center of the modulated region. Since the mode is concentrated at the center, the resonant wavelength is more sensitive to the deviation of the first few holes. If the standard deviation of each hole radius is $\delta r = 1$ nm, the standard deviation of the resonant wavelength, considering holes on both sides of the defect, is $\delta\lambda = 0.756$ nm.

Depending on the fabrication quality (δr), the standard deviation of the resonant wavelength is $\delta\lambda = 0.756 \cdot \delta r$. The disorder in the resonant frequency for bandgap-modulated resonators is slightly smaller than that for grating-defect resonators shown in Chapter 4. To reduce the disorder in resonant frequency for a given deviation of hole radii, we can increase the length of the modulated section while decreasing the modulation depth of the period. In this way the modal size is longer, and the resonant wavelength is less sensitive to the deviation of holes.

6.6 Experiment Results

We fabricated bandgap-modulated resonators and CROWs with a different geometry of grating. Fig. 6.8(a) shows a top image of a CROW. The waveguide is 565 nm wide. The holes are in a racetrack shape and are 150 nm long in the longitudinal direction and 452.5 nm wide in the transverse direction. The periods are 377.5 nm in the mirror section and 362.4 nm at the center of the modulated section, with a quadratic modulation. The modulated section consists of 9 different periods (M=9) and thus 17 holes. The length of the coupling section was chosen as 120 nm, as shown in Fig. 6.8(a) and Fig. 6.8(b). As

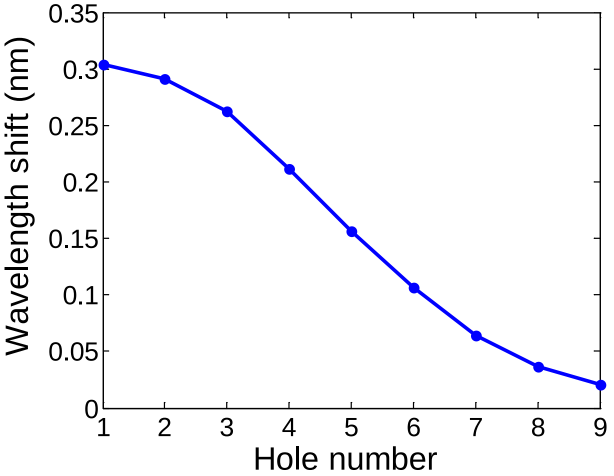

Fig. 6.7. Shift of resonant wavelength due to 1 nm change of radius for each hole starting from the center of the modulated section

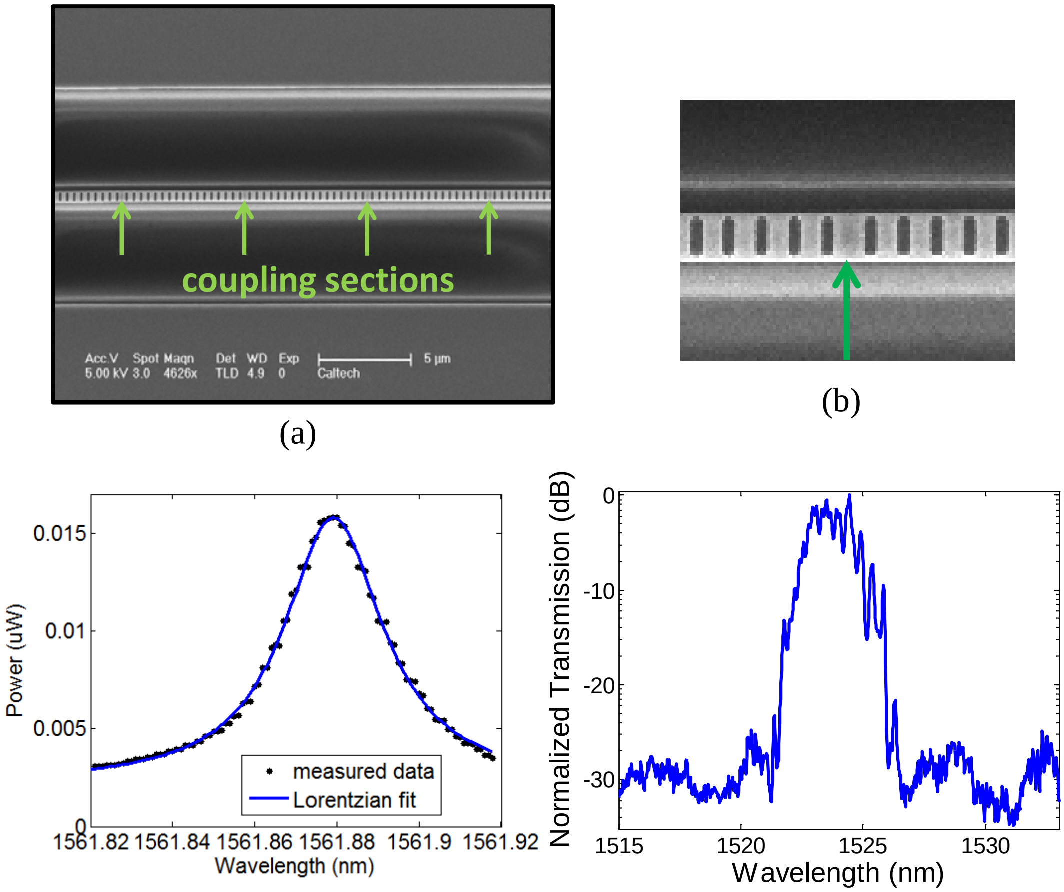

(a) (b) (c) (d)

Fig. 6.8. (a) SEM image of a CROW based on bandgap-modulated resonators. Arrows point out the coupling sections. (b) Close-up of the coupling section. (c) Transmission spectrum of a bandgap-modulated resonator. (d) Transmission spectrum of an N=6 CROW with M=8

we increase the number of mirror holes (m), the quality factor increases and saturates at the intrinsic Q. Fig. 6.8(c) shows the transmission spectrum of a resonator whose Q is 53300. Fig. 6.8(d) shows the transmission spectrum of a 6-resonator CROW with M=8. The bandwidth is approximately 4 nm.

In summary, we have demonstrated the design and experiment of bandgap-modulated resonators and CROWs. Compared to grating-defect resonators, bandgap-modulated resonators do not consist of small holes and are more robust in fabrication. These resonators possess higher theoretical Q. However, CROWs with these resonators require inter-resonator coupling sections. We showed in simulation and experiment that a judicious choice of the coupling sections reduces the oscillations in the transmission spectra and leads to maximally flat transmission.

Chapter 7

Grating Induced Transparency (GIT)

7.1 Introduction

Electromagnetically induced transparency (EIT) is a phenomenon that comes from quantum destructive interference between excitation pathways to the upper level of an atomic three-level system [65]. The combination of absorption cancellation and strong dispersion has led to the observation of very slow and stored light [14, 66]. In these experiments, atoms are prepared in a “dark”, coherent superposition of the two lower levels, a stationary eigenstate of the system of a three-level atom and two laser fields.

Classical analogs of EIT can be established in coupled optical resonators, referenced as coupled-resonator-induced transparency (CRIT) [67], where the mode splitting is a classical counterpart of dressed states arising from ac Stark effect. Several configurations of coupled resonators to obtain EIT-like resonances have been proposed and experimentally demonstrated [67-75]. These EIT-like resonances demonstrate much narrower linewidth than those of individual resonators.

In this chapter we propose to use a three-mode waveguide modulated by two co-spatial gratings as an optical analog to EIT. The three waveguide modes play the roles of the three quantum states in EIT, while the gratings are counterparts of the electromagnetic waves. Unlike CRIT, where the waveguide-resonator and inter-resonator coupling occur only at discrete points, the coupling of waveguide modes by gratings is continuous along the waveguide. This enables us to describe our system by coupled mode equations, in analogy to the Hamiltonian in the EIT system. The counterpart of the dark state in EIT is one of the supermodes of the waveguide-plus-grating system. By inserting phase shifts or apodizing the gratings, we are able to utilize the slow dark mode and produce EIT-like resonance. The structures can be a new class of optical resonators or optical delay lines.

7.2 Grating Induced Transparency and the Dark Mode

Guided by the formalism of the EIT three quantum state atomic system, we consider a waveguide supporting three distinct spatial modes with complex amplitudes *a*, *b*, *c*, propagation constants β_a, β_b, β_c, and containing two co-spatial gratings (one connects *a* and *b*; the other connects *b* and *c*). We do not restrict the direction of propagation of each mode. In the case of weak perturbation, the eigenmodes of the waveguide-plus-grating system, the supermodes, can be taken as linear superpositions of the unperturbed modes *a*, *b*, *c*, which obey the coupled equations [76]:

$$\begin{aligned} \frac{da}{dz} &= -j\beta_a a + \kappa_{ab}\exp(-j\frac{2\pi}{\Lambda_{ab}}z)b \\ \frac{db}{dz} &= -j\beta_b b + \kappa_{ba}\exp(j\frac{2\pi}{\Lambda_{ab}}z)a + \kappa_{bc}\exp(j\frac{2\pi}{\Lambda_{cb}}z)c\,, \\ \frac{dc}{dz} &= -j\beta_c c + \kappa_{cb}\exp(-j\frac{2\pi}{\Lambda_{cb}}z)b \end{aligned} \tag{7-1}$$

where $\Lambda_{ab} = 2\pi/(\beta_{a0} - \beta_{b0})$ and $\Lambda_{bc} = 2\pi/(\beta_{c0} - \beta_{b0})$ are the periods of the two gratings designed for a center frequency ω_0. κ_{ij} (i, j = a, b, c) are the coupling coefficient connecting modes *i* and *j*. By introducing new variables *A*, *B*, *C*, defined by $a(z) = A(z)\exp(-j\beta_{a0}z)$, $b(z) = B(z)\exp(-j\beta_{b0}z)$, $c(z) = C(z)\exp(-j\beta_{c0}z)$, we arrive at a *z*-independent coupling matrix:

$$\frac{d}{dz}\begin{bmatrix} A \\ B \\ C \end{bmatrix} = \begin{bmatrix} -j\delta_a & \kappa_{ab} & 0 \\ \kappa_{ba} & -j\delta_b & \kappa_{bc} \\ 0 & \kappa_{cb} & -j\delta_c \end{bmatrix} \cdot \begin{bmatrix} A \\ B \\ C \end{bmatrix}, \tag{7-2}$$

where $\delta_i \equiv \beta_i - \beta_{i0}$ is the detuning of the propagation constant. In the neighborhood of ω_0, $\delta_i = n_i(\Delta\omega)/c$ where n_i is the group index of each mode and $\Delta\omega = \omega - \omega_0$. The eigenvectors of the matrix are the supermodes of the perturbed waveguide, while the eigenvalues are the propagation constants of the supermodes. For example, the electric field of a supermode $[v_a\ v_b\ v_c]^{\mathrm{T}}$ with a propagation constant μ is given by $\exp(-i\mu z)\cdot [v_a \exp(-i\beta_{a0}z)E_a(x,y) + v_b \exp(-i\beta_{b0}z)E_b(x,y) + v_c \exp(-i\beta_{c0}z)E_c(x,y)]$, where $E_i(x,y)$ is the transverse mode profile. At center frequency ω_0, one of the supermodes is proportional to $[\kappa_{bc}\ 0\ -\kappa_{ba}]^{\mathrm{T}}$, with the eigenvalue equal to 0. In this supermode, which we name the dark mode, the intermediate mode *B* is unexcited. For comparison, the coupled equation of EIT ignoring decay rates is [65]

$$\frac{d}{dt}\left|\Psi\right\rangle = \begin{bmatrix} -j\Delta\omega & -\frac{j}{2}\Omega_p & 0 \\ -\frac{j}{2}\Omega_p & 0 & -\frac{j}{2}\Omega_c \\ 0 & -\frac{j}{2}\Omega_c & 0 \end{bmatrix} \left|\Psi\right\rangle, \tag{7-3}$$

where Ω_p and Ω_c are the Rabi frequencies of the probe and coupling beams, respectively, and $\Delta\omega$ is the frequency detuning of the probe beam. Eqs. (7-2) and (7-3) are similar on resonance. They are respectively equations of space and time. Conservation of energy defines the relation between κ_{ij} and κ_{ji} [76]: If mode *i* and *j* copropagate, $\kappa_{ij} = -\kappa_{ji}^*$; if mode *i* and *j* counterpropagate, $\kappa_{ij} = \kappa_{ji}^*$. Suppose *A* is the input forward mode, there are four different choices of propagating directions of mode *B* and *C* (Fig. 7.1). The formal similarity between Eqs. (7-2) and (7-3) depends on the nature of the κ_{ij} coefficients, which implies both modes *B* and *C* are forward propagating (Fig. 7.1(a)). This makes sense since in quantum mechanics each state evolves forward with time. Nevertheless,

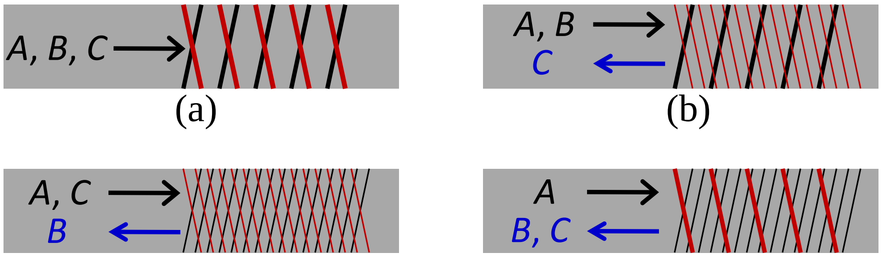

(a) (b)

(c) (d)

Fig. 7.1. Four configurations of the directions of the three modes. The black grating (/) couples modes *A* and *B*, while the red grating (\) couples mode *B* and *C*. The gratings are short-period or long-period depending on the directions of the connected modes.

the choice which is the most interesting for our slow light phenomenology is one where mode *A* is forward while *B* and *C* are backward propagating (Fig. 7.1(d)). A short-period grating connects modes A and B (κ_{ab}), while a long- period grating connects modes B and C (κ_{bc}). The coupling constants obey $\kappa_{bc} = -\kappa_{cb}^*$ and $\kappa_{ab} = \kappa_{ba}^*$. By shifting constant phases of variables *A*, *B*, and *C*, Eq. (7-2) can be rewritten as

$$\frac{d}{dz}\begin{bmatrix} A \\ B \\ C \end{bmatrix} = \begin{bmatrix} -j\delta_a & \kappa_{ab} & 0 \\ \kappa_{ab} & -j\delta_b & j\kappa_{bc} \\ 0 & j\kappa_{bc} & -j\delta_c \end{bmatrix} \cdot \begin{bmatrix} A \\ B \\ C \end{bmatrix} \equiv \boldsymbol{K} \cdot \begin{bmatrix} A \\ B \\ C \end{bmatrix}, \tag{7-4}$$

where $\boldsymbol{K}$ is defined as the coupling matrix. Now both κ_{ab} and κ_{bc} are real numbers. At $\Delta\omega = 0$, if $|\kappa_{ab}| \neq |\kappa_{bc}|$, the corresponding eigenvectors and eigenvalues are:

$$\text{Dark mode: } \frac{1}{\sqrt{\kappa_{ab}^2 + \kappa_{bc}^2}} \begin{bmatrix} \kappa_{bc} \\ 0 \\ j\kappa_{ab} \end{bmatrix}, \text{ eigenvalue} = 0 \tag{7-5}$$

and

$$\text{the two bright modes} \propto \begin{bmatrix} -j\kappa_{ab} \\ \pm\sqrt{\kappa_{bc}^2 - \kappa_{ab}^2} \\ \kappa_{bc} \end{bmatrix}, \text{ eigenvalues} = \pm j\sqrt{\kappa_{bc}^2 - \kappa_{ab}^2} \equiv \pm j\Delta\beta_0. \tag{7-6}$$

The three eigenvectors are not orthogonal to each other. They are nearly parallel when $|\kappa_{ab}|$ and $|\kappa_{bc}|$ are nearly equal. The two bright modes can propagate only if $|\kappa_{ab}| < |\kappa_{bc}|$, in which case the propagation constants $\pm\Delta\beta_0$ are real. Interestingly, the dark mode is a "propagating" (non-evanescent) supermode consisting of a superposition of two counter-propagating waves, *A* and *C*, which results in a group velocity that falls between the positive group velocity of the forward wave *A* and the negative group velocity of the backward wave *C* and can be derived by perturbation theory as

$$v_{g,dark} = \frac{1-\alpha^2}{n_a + \alpha^2 n_c} \cdot c, \tag{7-7}$$

where the tuning factor $\alpha \equiv \kappa_{ab} / \kappa_{bc}$. The group velocity is reduced to 0 when α approaches 1. We focus on the region $|\alpha| < 1$ where the group velocity is positive. Plotting the propagation constants of the three supermodes as functions of $\Delta\omega$ results in the band structure shown in Fig. 7.2 where α = 0.9. In general the waveguide is not periodic, unless the ratio of Λ_{ab} and Λ_{bc} is rational. Therefore, the band structure has two sets of Brillouin zones that repeat the dispersion curves periodically. The three modes intersect at $\Delta\omega = 0$ and anti-crossing occurs. A narrow transmission band in the center lies between two band gaps. All the three supermodes can propagate within the

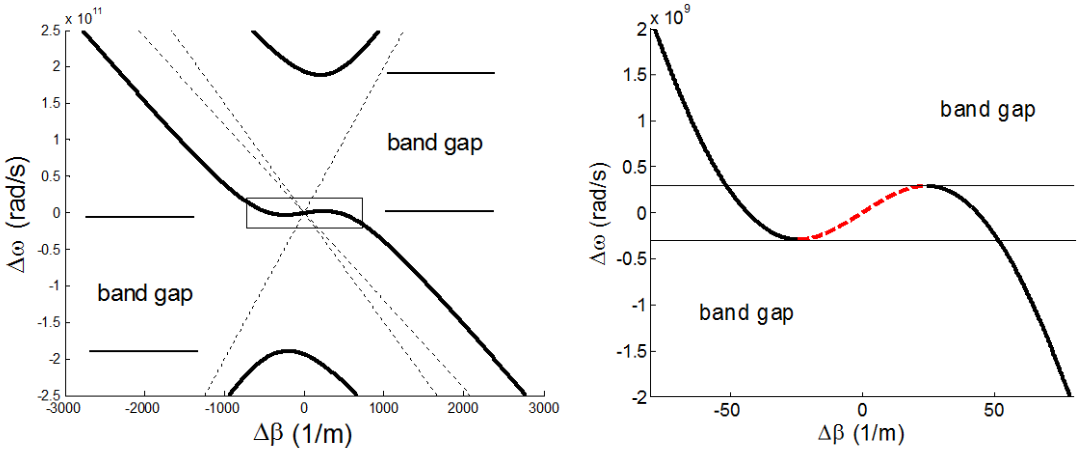

(a) (b)

Fig. 7.2. (a) Band structures of a GIT waveguide. n_a = 1.5, n_b = 2.5, n_c = 2. κ_{ab} = 90/m, κ_{bc} = 100/m. Dash lines are the band structure without grating perturbation. (b) Zoom-in figure of the bending region. The red dashed curve is the dark mode.

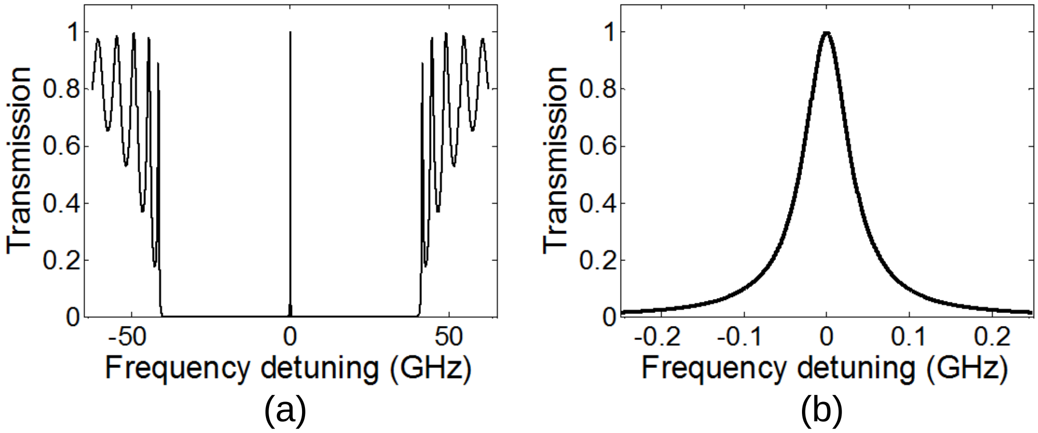

Fig. 7.3. (a) Transmission spectrum of a uniform structure. κ_{ab} = 900/m, κ_{bc} = 1,000/m, and $L = L_{min}$ = 1.44 cm. The refractive indices are n_a = 1.45, n_b = 1.425, and n_c = 1.4. (b) Transmission spectrum in a narrower span of the same structure in (a)

transmission band, while no forward-propagating mode exists within the two band gaps since the only propagating supermode consists mainly of backward modes *B* and *C*. The group velocity dispersion (GVD) of the dark mode in the center ($\Delta\omega = 0$) is zero. The group velocity of the two bright modes is $v_{g,bright} = -(1-\alpha^2)\cdot c/n$ in the assumption that $n_a \approx n_b \approx n_c \approx n$.

7.3 Uniform GIT Waveguides

To take advantage of the new modes, especially the dark one, we propose two types of structures. The first is a uniform one where both gratings (κ_{ab} and κ_{bc}) are of uniform strengths along the length *L* of the waveguide. If the boundary condition corresponds to a single input mode *A* at $z = 0$ and no input backward modes *B* and *C* at $z = L$, the field at $z = L$ is proportional to $[1\ 0\ 0]^T$, which decomposes into all the three supermodes. Transmission of mode *A* and field distribution along the structure can be obtained by back propagating the three supermodes to $z = 0$. Unity transmission at $\Delta\omega = 0$ results if the length is a multiple of $L_{min} = 2\pi/\sqrt{\kappa_{bc}^2 - \kappa_{ab}^2}$ since 0 and $\pm\sqrt{\kappa_{bc}^2 - \kappa_{ab}^2}$ are the propagation constants of the three supermodes. Fig. 7.3 shows the transmission spectrum of a waveguide with $\alpha = 0.9$,κ_{bc} = 1,000/m, and L = L_{min} = 1.44 cm. The transmission spectrum is similar to that of EIT. The FWHM bandwidth is 66.2 MHz, and the group delay in the center wavelength is 4.97 ns with group velocity reduction of 71.3 (compared to group velocity of mode *A*).

The case of uniform gratings occupying $0 < z < L$ can be viewed as a resonator where the two backward bright modes are reflected into the forward dark mode at z = 0 and conversely at $z = L$. The round-trip phase of the cavity includes the forward propagation of the dark mode, the backward propagation of the two bright modes, and the phase of reflectance of the two mirrors. This explains why L has to be a multiple of L_{min} for resonance at $\Delta\omega = 0$. Since the transmission of mode *A* depends on phase matching of the three supermodes, the bandwidth is extremely narrow and the group velocity reduction is much larger than that of the dark mode in Eq. (7-7). At $\Delta\omega = 0$, the field distributions of the individual modes are

$$\begin{aligned} A(z) &= \frac{1}{1-\alpha^2}[1-\alpha^2\cos(\Delta\beta_0 z)] \\ B(z) &= \frac{\alpha}{\sqrt{1-\alpha^2}}\sin(\Delta\beta_0 z) \\ C(z) &= \frac{j\alpha}{1-\alpha^2}[1-\cos(\Delta\beta_0 z)], \end{aligned} \tag{7-8}$$

assuming the input $A(0) = 1$. Fig. 7.4 plots the field distribution for α = 0.95 and L = $2L_{min}$. Since the three supermodes are nearly parallel, they interfere constructively to extremely high intensities of individual modes *A*, *B*, *C* in the middle of the structure, and destructively interfere to small intensity of *A* at the two ends. The quality factor *Q* of the resonator defined as $\omega \cdot$(energy stored) / (power loss) can be obtained from Eq. (7-8) assuming $n_a \approx n_b \approx n_c$ and is given by

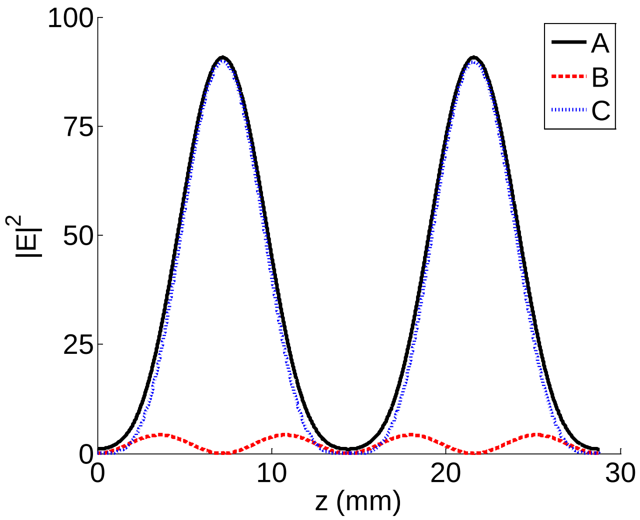

Fig. 7.4. Energy distribution of a uniform structure with $L = 2L_{min}$ and an input $A(0) = 1$. $\kappa_{ab} = 900$/m, $\kappa_{bc} = 1{,}000$/m, and $L = 2.88$ cm. The refractive indices are $n_a = 1.45$, $n_b = 1.425$, and $n_c = 1.4$.

$$Q = \beta_a L \frac{1+2\alpha^2}{(1-\alpha^2)^2}, \tag{7-9}$$

where L is fixed to be a multiple of L_{min}. If α is close to 1, say 0.999 for example, the factor $(1+2\alpha^2)/(1-\alpha^2)^2$ is as high as 7.5×10^5, while the length required is 14 cm assuming $\kappa_{bc} = 1{,}000$/m. By employing gain in the structure with a high quality factor we can make a laser with the minimum threshold gain occurring when L is a multiple of L_{min} and is inversely proportional to the quality factor.

For the example in Fig. 7.3, the phase shift across the transmission band is about π, limiting the delay-bandwidth product less than 0.5, like a single resonator. Cascading N resonators, namely increasing L to $N\cdot L_{min}$, will result in more delay but reduced bandwidth, since the phase mismatch of the three supermodes is approximately proportional to $(\Delta\omega)L$. In fact, as shown in Fig. 7.6(a), there are $2N$–1 peaks in the transmission spectrum, each with a phase shift of π across, limiting the delay-bandwidth product still less than 0.5. To break this limit, we propose to invert the sign of α $(=\kappa_{ab} / \kappa_{bc})$ every L_{min} along the waveguide, as illustrated in Fig. 7.6(a). By doing this periodic inversion, it can be shown that the first-order term of the reflectance at z=0 as a function of $\Delta\omega$ is cancelled out when N is even. Fig. 7.5(b) and Fig. 7.5(c) show the transmission spectrum and group delay of the modified waveguide with $L = N\cdot L_{min}$, where the bandwidth is not reduced and the envelope of the ripples is approximately a quadratic function. The group delay at $\Delta\omega = 0$ and the quality factor of the modified waveguide is exactly the same as the original one, while the delay-bandwidth product is unlimited and the total phase shift across the bandwidth is $N\pi$.

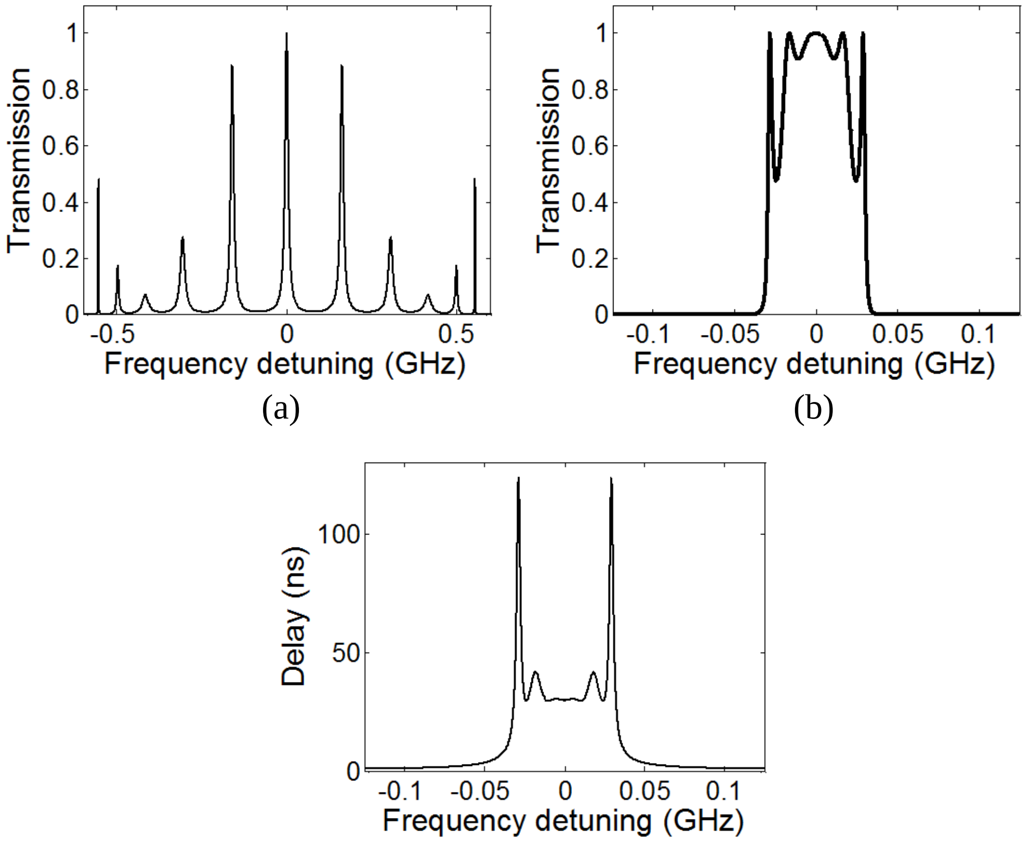

(a)

(b)

(c)

Fig. 7.5. (a) Transmission spectrum of a uniform structure with $L = 6L_{min}$. (b) Transmission spectrum of a uniform structure with $L = 6L_{min}$ and periodic inversion of κ_{ab}. (c) Group delay of the structure in (b)

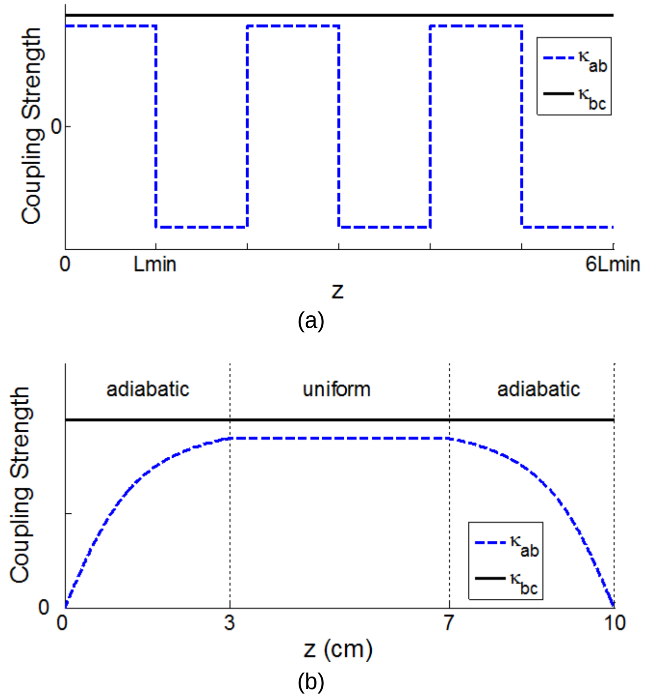

Fig. 7.6. (a) κ_{ab} and κ_{bc} in a uniform structure with periodic inversion. (b) κ_{ab} and κ_{bc} in an adiabatic structure. L_{ad} and L_{uni} are the lengths of the adiabatic and uniform region, respectively

7.4 Adiabatic GIT Waveguides

The second structure limiting the excitation to the dark mode alone is achieved by employing adiabatic transition [77, 78]. This is accomplished by changing the structure (waveguide + gratings) sufficiently slowly along the direction of propagation (z) so that the propagating wave remains in the same local eigenmode. As shown in Fig. 7.6(b), the waveguide consists of two adiabatic regions at the two ends and a uniform region in the middle. κ_{bc} is set to be a constant throughout the structure, while κ_{ab}, and thus α, are functions of z. The input mode A entering the structure encounters only grating κ_{bc} and is thus the dark mode (Eq. (7-5)) where it will remain till exiting the structure. As it propagates, the grating κ_{ab} is turned on spatially adiabatically. In the middle of the structure, the dark mode which now has a mode C component possesses a small group velocity. At the output, κ_{ab} is adiabatically decreased to 0, and the propagating wave is transformed back, always staying dark, to mode *A* at the exit.

The adiabatic condition ensuring that a wave remains in the same (dark) mode is defined as the situation where the fraction of the energy converted to other modes never exceeds an arbitrarily chosen small number ε. The adiabatic condition of the GIT waveguide and an optimal function $\alpha(z)$ can be derived in a similar way as in quantum mechanics [79] and an adiabatic mode converter [80], with careful treatment of the non-orthogonal basis. The three eigenvectors in Eqs. (7-5) and (7-6) should be renormalized such that the total forward energy flow is 1 or –1, given by

$$\boldsymbol{v_{dark}} = \frac{1}{\sqrt{1-\alpha^2}}\begin{bmatrix}1\\0\\j\alpha\end{bmatrix},\ \boldsymbol{v_{bright\text{-}1,2}} = \frac{1}{\sqrt{2(1-\alpha^2)}}\begin{bmatrix}-j\alpha\\ \pm\sqrt{1-\alpha^2}\\ 1\end{bmatrix}. \tag{7-10}$$

When decomposing a vector $\boldsymbol{x} = [A\ B\ C]^{\mathrm{T}}$ into the three supermodes, the amplitude of each supermode can be determined by the product with the associated left eigenvectors of the coupling matrix $\boldsymbol{K}$ since $\boldsymbol{u_i}^T\boldsymbol{v_j} = \delta_{ij}$, where $\boldsymbol{u_i}^T$ and $\boldsymbol{v_i}$ are respectively the ***i***-th left and right eigenvectors associated with the eigenvalue λ_i of the coupling matrix $\boldsymbol{K}$. The fields $\boldsymbol{x}$ can be written as the superposition of the supermodes $\boldsymbol{v_i}$,

$$\boldsymbol{x}(z) = \sum_{i=dark,bright} a_i(z)\boldsymbol{v_i}(z)\exp[-j\int_0^z \beta_i(z')dz']. \tag{7-11}$$

Substituting Eq. (7-11) into the coupled equations $d\boldsymbol{x}(z)/dz = \boldsymbol{K}(z)\boldsymbol{x}(z)$ (Eq. (7-4)) leads to

$$\sum_{i=dark,bright}[(\partial_z a_i)\boldsymbol{v_i} + a_i(\partial_z \boldsymbol{v_i})]\exp[-j\int_0^z \beta_i(z')dz'] = 0. \tag{7-12}$$

For adiabatic transition of the Dark mode ($\boldsymbol{v_{dark}}$), $a_{dark} \approx 1$ and $a_{bright-1,2} \approx 0$. Multiplying $\boldsymbol{u_{bright\text{-}1}}^{\mathrm{T}}$ from the left side results in

$$da_{bright-1}/dz = \boldsymbol{u_{bright\text{-}1}}^T(\partial_z \boldsymbol{v_{dark}})\exp[\mathrm{j}\int_0^z \beta_{\mathrm{bright\text{-}1}}(z')dz'], \tag{7-13}$$

since $\beta_{dark} = 0$. $\boldsymbol{u}_{\boldsymbol{bright\text{-}1}}{}^{T}(\partial_z \mathbf{v}_{\boldsymbol{dark}})$ can be shown to be $j/\left[\sqrt{2}(1-\alpha^2)\right]\cdot\partial\alpha/\partial z$, and with the assumption that it is slowly varying compared to the exponential term, Eq. (7-13) can be solved as

$$a_{bright-1}(z) = \frac{-\sqrt{2}j}{\kappa_{bc}(1-\alpha^2)^{3/2}}\frac{\partial\alpha}{\partial z}\sin(\frac{\beta_{\text{bright-1}}}{2}z)\exp[j\frac{\beta_{\text{bright-1}}}{2}z]. \tag{7-14}$$

Likewise for $a_{bright\text{-}2}(z)$. The adiabatic condition where only the Dark mode exists requires $\left|a_{bright-1}(z)\right|^2 + \left|a_{bright-2}(z)\right|^2 \leq \varepsilon$, which give

$$\frac{d\alpha}{dz} \leq \frac{\kappa_{bc}}{4}(1-\alpha^2)^{\frac{3}{2}}\sqrt{\varepsilon}. \tag{7-15}$$

The closer α is to 1, the smaller $d\alpha/dz$ is required to achieve adiabaticity. By solving Eq. (7-15) with equality, we obtain an optimal function $\alpha(z)$ given by

$$\alpha(z) = \sin^{-1}(\tan(az)), \tag{7-16}$$

where a is a scaling constant. It takes infinite length to transform α to 1 to reach zero group velocity. Fig. 7.7 shows the transmission spectrum and group delay of an adiabatic GIT structure, where α of the uniform region is 0.9 and the total length is 10 cm. The

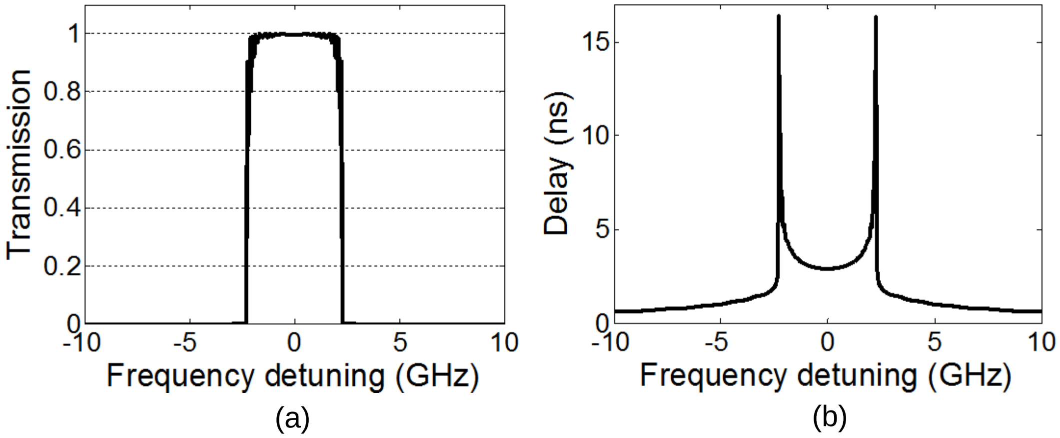

Fig. 7.7. (a) Transmission and (b) group delay of an adiabatic structure. L_{ad} = 3 cm, L_{uni} = 4 cm, κ_{bc} = 4,000/m, and $\alpha_{\max}$ = 0.9. The refractive indices are n_a = 1.45, n_b = 1.425, and n_c = 1.4.

transmission spectrum resembles a rectangular function, with a bandwidth of 4.48 GHz, equal to that of the dark mode of the uniform region. The group delay mainly depends on the group velocity of the dark mode of the uniform region and is 2.92 ns at the center wavelength with group velocity reduction of 6.04. The delay-bandwidth product, which is 13.1 in this case, can be made arbitrarily large by increasing the length of the uniform region without reducing the bandwidth.

7.5 Discussion

We have analyzed the EIT-analog waveguide and proposed two types of structures to control the propagation of supermodes. This GIT waveguide can be implemented using a few-mode fiber or a few-mode on-chip waveguide. One short-period grating and another long-period grating are imposed on the waveguide. For a waveguide with geometric symmetry, the modes are either symmetric or anti-symmetric, so are the gratings that couple the modes. Therefore, the two gratings can be independent of each other if they have opposite symmetry. The symmetry of a grating can be controlled by tilting the grating in fibers or designing the transverse profile of a waveguide grating. The phase indices of the three modes should be carefully chosen, in case any unwanted mode is coupled by one of the gratings, since there are three forward and three backward modes in total. Moreover, to reduce loss, coupling into the radiation modes should be prevented.

In conclusion, the new energy storage mechanism resulting from the internal bouncing of waves between two Bragg gratings gives rise to a new class of propagating modes which includes a dark mode with “slow light” characteristics. These modes can potentially form the basis of a new class of narrow band filters, high Q resonators and lasers. The adiabatic GIT structures which excite the dark mode alone possess high delay-bandwidth product.

Chapter 8

Conclusion

8.1 Summary of the Thesis

In this thesis, we discussed methods for overcoming the transmission losses of CROWs – Resonator loss, discontinuity between CROWs and waveguides, and fabrication disorder. These transmission losses have been the major limitation of CROWs since it was proposed in 1999 [26]. The type of resonators we worked on are waveguide-grating resonators, including grating-defect resonators shown in Chapter 4 and bandgap-modulated resonators shown in Chapter 6. The features of these resonators are their small footprints, control of coupling coefficients via holes, and natural implementation on waveguides.

We overcame the resonator loss by designing high-Q grating-defect resonators. We demonstrated a systematic design approach for choosing the taper profile which minimizes the coupling to radiation modes and possesses a Q of 2.16×10^{6}. We presented the design of bandgap-modulated resonators which possess a Q of 1.83×10^{8}. In the fabrication, we developed the recipes which minimize the roughness on the sidewall. The measured Q is approximately 10^{5} and is high enough that the propagation loss with a delay of a few picoseconds is negligible. We demonstrated the coupling of these high-Q resonators and the control of coupling coefficients via the number of holes.

The discontinuity between CROWs and waveguides is addressed by adiabatically changing the coupling coefficients. While we were working on the choice of the coupling coefficients, we found that the optimal design is a Butterworth filter. Therefore, we developed a filter design formalism for deriving the coupling coefficients which directly relate to a desired filter response. The formalism is based on coupled-mode theory and can be applied to various types of resonators, including grating resonators. The filters of interest are Butterworth filters and Bessel filters, which possess optimal-flat transmission and optimal-flat group delay, respectively. The final step in the optimization of CROWs is an “ideal” optical delay line which possesses constant amplitude and constant group delay simultaneously over a prescribed bandwidth. This ideal delay line is based on a reflecting and tailored-coupling CROW whose transfer function is an all-pass Bessel filter.

We analyzed the effect of disorder in resonant frequencies and coupling coefficients on CROWs, especially CROWs based on grating resonators. The effect of disorder in resonant frequencies is bandwidth-dependent, while the effect of disorder in coupling coefficients is independent of the bandwidth. We showed in the simulation that Butterworth filters are more robust against disorder in resonant frequencies than CROWs with uniform coupling. This was later confirmed in the measurement of grating CROWs. In the experiment of grating CROWs, we concluded that the disorder of resonant frequencies is the dominant disorder effect, which is based on the fact that Butterworth filters are more robust than uniform CROWs and that the disorder effect is bandwidth-dependent.

We demonstrated the fabrication and measurement of grating CROWs. We worked on several types of couplers for increasing the coupling efficiency and reducing the facet reflection. The most significant results include high-Q (Q~10^5) grating resonators, coupling of up to 50 resonators, control of group velocity (between c/13 and c/49) via the number of holes, and Butterworth filters. These devices are very short on silicon waveguides (less than 10 μm per resonators).

I also presented my earlier work on an optical analog to EIT. The proposed GIT structure consists of two co-spatial gratings imposed on a three-mode waveguide. One of the supermodes, the Dark mode, possesses a group velocity which depends on the ratio of the two grating strengths. The group velocity approaches zero when the two grating strengths are nearly equal. We proposed an adiabatic structure which excites only the Dark mode.

In summary, this thesis presented the theory and experiment of CROWs and grating structures. Three kinds of transmission losses have been addressed by the design of resonators and coupling coefficients as well as the fabrication. The grating CROWs developed in this thesis may be important components of optical networks in the future.

8.2 Outlook

Bandgap-modulated resonators for CROWs can potentially be more robust than CROWs based on grating-defect resonators, due to the identical and larger hole sizes. The experimental results shown in Chapter 7 are preliminary. We are working on the realization of bandgap-modulated CROWs with our optimized fabrication technology. Filter design based on bandgap-modulated CROWs will be tricky, since the resonant wavelength changes with the number of mirror holes. Since Butterworth filter design suppress the disorder effect, it may be necessary to apply the filter design.

Grating resonators can also be side-coupled in the transverse direction. Adjacent resonators couple to each other via the evanescent field in the cladding, and the coupling strength depends on the distance between adjacent waveguides. Controlling the coupling strength via the gap between waveguides can be challenging. However, this may enable filter design on bandgap-modulated resonators since the coupling coefficients are independent of the resonant frequency.

Grating resonators with weaker grating strength may be interesting. Since the modal size is larger, it will be less sensitive to fabrication disorder. CROWs with narrower bandwidth and larger group delay will be possible with weaker gratings. The footprints of the CROWs will increase as well, so there is a trade-off between large group delay and small footprints of CROWs. Weaker gratings on silicon waveguides can be achieved with shallower holes or sidewall gratings.

One important application of slow light is nonlinear optics. If all the components in the nonlinear process, i.e., pump, signal, and idler, are slowed down, the nonlinear efficiency is greatly enhanced. The major limitations of slow light enhanced nonlinear optics are the propagation loss and the group velocity dispersion. The propagation loss can be overcome with the fabrication of high-Q resonators. The group velocity dispersion may be minimized with a judicious choice of coupling coefficients. In this thesis we have shown the filter design approach and various types of filters for both transmitting and reflecting CROWs. It is worth studying the choice of coupling coefficients for nonlinear optics in both theory and experiment.

The idea of GIT which consists of two gratings and three modes may be applied to the design of 2D photonic crystal. In a 2D photonic crystal, there are infinite number of reciprocal vectors. The idea of GIT can be realized with two reciprocal vectors and three plane waves. GIT in photonic crystals results in a dispersion curve whose slope is small over a range of frequencies and controllable via the strength of the two Fourier components.

Bibliography

[1] F. S. Johnson, "Physical Cause of Group-Velocity in Normally Dispersive, Nondissipative Media," Am. J. Phys. **58**, 1044-1056 (1990).

[2] R. S. Tucker, P. C. Ku, and C. J. Chang-Hasnain, "Slow-light optical buffers: Capabilities and fundamental limitations," J. Lightwave Technol. **23**, 4046-4066 (2005).

[3] Z. M. Shi, R. W. Boyd, D. J. Gauthier, and C. C. Dudley, "Enhancing the spectral sensitivity of interferometers using slow-light media," Opt. Lett. **32**, 915-917 (2007).

[4] A. Schweinsberg, Z. M. Shi, J. E. Vornehm, and R. W. Boyd, "Demonstration of a slow-light laser radar," Opt. Express **19**, 15760-15769 (2011).

[5] T. Baba, "Slow light in photonic crystals," Nature Photon. **2**, 465-473 (2008).

[6] C. Monat, B. Corcoran, D. Pudo, M. Ebnali-Heidari, C. Grillet, M. D. Pelusi, D. J. Moss, B. J. Eggleton, T. P. White, L. O'Faolain, and T. F. Krauss, "Slow Light Enhanced Nonlinear Optics in Silicon Photonic Crystal Waveguides," IEEE J. Sel. Topic Quantum Electron. **16**, 344-356 (2010).

[7] A. Melloni, F. Morichetti, and M. Martinelli, "Four-wave mixing and wavelength conversion in coupled-resonator optical waveguides," J. Opt. Soc. Am. B **25**, C87-C97 (2008).

[8] C. Monat, M. Ebnali-Heidari, C. Grillet, B. Corcoran, B. J. Eggleton, T. P. White, L. O'Faolain, J. Li, and T. F. Krauss, "Four-wave mixing in slow light engineered silicon photonic crystal waveguides," Opt. Express **18**, 22915-22927 (2010).

[9] N. Matsuda, T. Kato, K. Harada, H. Takesue, E. Kuramochi, H. Taniyama, and M. Notomi, "Slow light enhanced optical nonlinearity in a silicon photonic crystal coupled-resonator optical waveguide," Opt. Express **19**, 19861-19874 (2011).

[10] J. R. Ong, M. L. Cooper, G. Gupta, W. M. J. Green, S. Assefa, F. N. Xia, and S. Mookherjea, "Low-power continuous-wave four-wave mixing in silicon coupled-resonator optical waveguides," Opt. Lett. **36**, 2964-2966 (2011).

[11] B. Corcoran, C. Monat, C. Grillet, D. J. Moss, B. J. Eggleton, T. P. White, L. O'Faolain, and T. F. Krauss, "Green light emission in silicon through slow-light enhanced third-harmonic generation in photonic-crystal waveguides," Nature Photon. **3**, 206-210 (2009).

[12] C. Husko, T. D. Vo, B. Corcoran, J. Li, T. F. Krauss, and B. J. Eggleton, "Ultracompact all-optical XOR logic gate in a slow-light silicon photonic crystal waveguide," Opt. Express **19**, 20681-20690 (2011).

[13] B. Corcoran, M. D. Pelusi, C. Monat, J. T. Li, L. O'Faolain, T. F. Krauss, and B. J. Eggleton, "Ultracompact 160 Gbaud all-optical demultiplexing exploiting slow light in an engineered silicon photonic crystal waveguide," Opt. Lett. **36**, 1728-1730 (2011).

[14] L. V. Hau, S. E. Harris, Z. Dutton, and C. H. Behroozi, "Light speed reduction to 17 metres per second in an ultracold atomic gas," Nature **397**, 594-598 (1999).

[15] M. S. Bigelow, N. N. Lepeshkin, and R. W. Boyd, "Superluminal and slow light propagation in a room-temperature solid," Science **301**, 200-202 (2003).

[16] Y. Okawachi, M. S. Bigelow, J. E. Sharping, Z. M. Zhu, A. Schweinsberg, D. J. Gauthier, R. W. Boyd, and A. L. Gaeta, "Tunable all-optical delays via Brillouin slow light in an optical fiber," Phys Rev Lett **94** (2005).

[17] J. E. Sharping, Y. Okawachi, and A. L. Gaeta, "Wide bandwidth slow light using a Raman fiber amplifier," Opt. Express **13**, 6092-6098 (2005).

[18] H. C. Liu and A. Yariv, "Grating induced transparency (GIT) and the dark mode in optical waveguides," Opt. Express **17**, 11710-11718 (2009).

[19] M. Notomi, E. Kuramochi, and T. Tanabe, "Large-scale arrays of ultrahigh-Q coupled nanocavities," Nature Photon. **2**, 741-747 (2008).

[20] J. K. S. Poon, L. Zhu, G. A. DeRose, and A. Yariv, "Transmission and group delay of microring coupled-resonator optical waveguides," Opt. Lett. **31**, 456-458 (2006).

[21] F. N. Xia, L. Sekaric, and Y. Vlasov, "Ultracompact optical buffers on a silicon chip," Nature Photon. **1**, 65-71 (2007).

[22] S. Nishikawa, S. Lan, N. Ikeda, Y. Sugimoto, H. Ishikawa, and K. Asakawa, "Optical characterization of photonic crystal delay lines based on one-dimensional coupled defects," Opt. Lett. **27**, 2079-2081 (2002).

[23] J. Li, T. P. White, L. O'Faolain, A. Gomez-Iglesias, and T. F. Krauss, "Systematic design of flat band slow light in photonic crystal waveguides," Opt. Express **16**, 6227-6232 (2008).

[24] Y. A. Vlasov, M. O'Boyle, H. F. Hamann, and S. J. McNab, "Active control of slow light on a chip with photonic crystal waveguides," Nature **438**, 65-69 (2005).

[25] D. Janner, G. Galzerano, G. Della Valle, P. Laporta, S. Longhi, and M. Belmonte, "Slow light in periodic superstructure Bragg gratings," Phys. Rev. E **72**, 056605 (2005).

[26] A. Yariv, Y. Xu, R. K. Lee, and A. Scherer, "Coupled-resonator optical waveguide: a proposal and analysis," Opt. Lett. **24**, 711-713 (1999).

[27] X. S. Luo and A. W. Poon, "Many-element coupled-resonator optical waveguides using gapless-coupled microdisk resonators," Opt. Express **17**, 23617-23628 (2009).

[28] H. A. Haus and Y. Lai, "Theory of cascaded quarter wave shifted distributed feedback resonators," IEEE J. Quantum Elect. **28**, 205-213 (1992).

[29] A. Melloni, F. Morichetti, C. Ferrari, and M. Martinelli, "Continuously tunable 1 byte delay in coupled-resonator optical waveguides," Opt. Lett. **33**, 2389-2391 (2008).

[30] B. E. Little, S. T. Chu, P. P. Absil, J. V. Hryniewicz, F. G. Johnson, E. Seiferth, D. Gill, V. Van, O. King, and M. Trakalo, "Very high-order microring resonator filters for WDM applications," IEEE Photon. Technol. Lett. **16**, 2263-2265 (2004).

[31] F. N. Xia, M. Rooks, L. Sekaric, and Y. Vlasov, "Ultra-compact high order ring resonator filters using submicron silicon photonic wires for on-chip optical interconnects," Opt. Express **15**, 11934-11941 (2007).

[32] P. Dong, N. N. Feng, D. Z. Feng, W. Qian, H. Liang, D. C. Lee, B. J. Luff, T. Banwell, A. Agarwal, P. Toliver, R. Menendez, T. K. Woodward, and M. Asghari, "GHz-bandwidth optical filters based on high-order silicon ring resonators," Opt. Express **18**, 23784-23789 (2010).

[33] Q. Li, M. Soltani, S. Yegnanarayanan, and A. Adibi, "Design and demonstration of compact, wide bandwidth coupled-resonator filters on a silicon-on-insulator platform," Opt. Express **17**, 2247-2254 (2009).

[34] S. J. Xiao, M. H. Khan, H. Shen, and M. H. Qi, "A highly compact third-order silicon microring add-drop filter with a very large free spectral range, a flat passband and a low delay dispersion," Opt. Express **15**, 14765-14771 (2007).

[35] D. Park, S. Kim, I. Park, and H. Lim, "Higher order optical resonant filters based on coupled defect resonators in photonic crystals," J. Lightwave Technol. **23**, 1923-1928 (2005).

[36] A. Martinez, J. Garcia, P. Sanchis, E. Cuesta-Soto, J. Blasco, and J. Marti, "Intrinsic losses of coupled-cavity waveguides in planar-photonic crystals," Opt. Lett. **32**, 635-637 (2007).

[37] P. Chak and J. E. Sipe, "Minimizing finite-size effects in artificial resonance tunneling structures," Opt. Lett. **31**, 2568-2570 (2006).

[38] M. Sumetsky and B. J. Eggleton, "Modeling and optimization of complex photonic resonant cavity circuits," Opt. Express **11**, 381-391 (2003).

[39] J. Capmany, P. Munoz, J. D. Domenech, and M. A. Muriel, "Apodized coupled resonator waveguides," Opt. Express **15**, 10196-10206 (2007).

[40] C. K. Madsen and J. H. Zhao, *Optical filter design and analysis, a signal processing approach* (Wiley, 1999).

[41] R. Orta, P. Savi, R. Tascone, and D. Trinchero, "Synthesis of multiple-ring-resonator filters for optical systems," IEEE Photon. Technol. Lett. **7**, 1447-1449 (1995).

[42] B. E. Little, S. T. Chu, H. A. Haus, J. Foresi, and J. P. Laine, "Microring resonator channel dropping filters," J. Lightwave Technol. **15**, 998-1005 (1997).

[43] V. Van, "Circuit-based method for synthesizing serially coupled microring filters," J. Lightwave Technol. **24**, 2912-2919 (2006).

[44] A. Melloni and M. Martinelli, "Synthesis of direct-coupled-resonators bandpass filters for WDM systems," J. Lightwave Technol. **20**, 296-303 (2002).

[45] J. K. S. Poon and A. Yariv, "Active coupled-resonator optical waveguides. I. Gain enhancement and noise," J. Opt. Soc. Am. B **24**, 2378-2388 (2007).

[46] H. A. Haus, *Waves and fields in optoelectronics* (Prentice-Hall, Englewood Cliffs, New Jersey, 1984).

[47] A. M. Prabhu and V. Van, "Predistortion techniques for synthesizing coupled microring filters with loss," Opt. Commun. **281**, 2760-2767 (2008).

[48] J. K. S. Poon, J. Scheuer, S. Mookherjea, G. T. Paloczi, Y. Y. Huang, and A. Yariv, "Matrix analysis of microring coupled-resonator optical waveguides," Opt. Express **12**, 90-103 (2004).

[49] S. Mookherjea and A. Oh, "Effect of disorder on slow light velocity in optical slow-wave structures," Opt. Lett. **32**, 289-291 (2007).

[50] C. Ferrari, F. Morichetti, and A. Melloni, "Disorder in coupled-resonator optical waveguides," J. Opt. Soc. Am. B **26**, 858-866 (2009).

[51] P. Velha, E. Picard, T. Charvolin, E. Hadji, J. C. Rodier, P. Lalanne, and D. Peyrade, "Ultra-high Q/V Fabry-Perot microcavity on SOI substrate," Opt. Express **15**, 16090-16096 (2007).

[52] A. R. M. Zain, N. P. Johnson, M. Sorel, and R. M. De la Rue, "Ultra high quality factor one dimensional photonic crystal/photonic wire micro-cavities in silicon-on-insulator (SOI)," Opt. Express **16**, 12084-12089 (2008).

[53] E. Kuramochi, H. Taniyama, T. Tanabe, K. Kawasaki, Y. G. Roh, and M. Notomi, "Ultrahigh-Q one-dimensional photonic crystal nanocavities with modulated mode-gap barriers on SiO_2 claddings and on air claddings," Opt. Express **18**, 15859-15869 (2010).

[54] Q. M. Quan, P. B. Deotare, and M. Loncar, "Photonic crystal nanobeam cavity strongly coupled to the feeding waveguide," Appl. Phys. Lett. **96**, 203102 (2010).

[55] Y. Akahane, T. Asano, B. S. Song, and S. Noda, "High-Q photonic nanocavity in a two-dimensional photonic crystal," Nature **425**, 944-947 (2003).

[56] A. Yariv and P. Yeh, *Photonics,* 6th ed. (Oxford University Press, 2007).

[57] J. W. Mu and W. P. Huang, "Simulation of three-dimensional waveguide discontinuities by a full-vector mode-matching method based on finite-difference schemes," Opt. Express **16**, 18152-18163 (2008).

[58] H. C. Liu and A. Yariv, "Synthesis of high-order bandpass filters based on coupled-resonator optical waveguides (CROWs)," Opt. Express **19**, 17653-17668 (2011).

[59] V. R. Almeida, R. R. Panepucci, and M. Lipson, "Nanotaper for compact mode conversion," Opt. Lett. **28**, 1302-1304 (2003).

[60] S. J. McNab, N. Moll, and Y. A. Vlasov, "Ultra-low loss photonic integrated circuit with membrane-type photonic crystal waveguides," Opt. Express **11**, 2927-2939 (2003).

[61] J. Chan, M. Eichenfield, R. Camacho, and O. Painter, "Optical and mechanical design of a "zipper" photonic crystal optomechanical cavity," Opt. Express **17**, 3802-3817 (2009).

[62] A. H. Safavi-Naeini, T. P. M. Alegre, M. Winger, and O. Painter, "Optomechanics in an ultrahigh-Q two-dimensional photonic crystal cavity," Appl. Phys. Lett. **97** (2010).

[63] K. Srinivasan and O. Painter, "Momentum space design of high-Q photonic crystal optical cavities," Opt. Express **10**, 670-684 (2002).

[64] E. Kuramochi, M. Notomi, S. Mitsugi, A. Shinya, T. Tanabe, and T. Watanabe, "Ultrahigh-Q photonic crystal nanocavities realized by the local width modulation of a line defect," Appl. Phys. Lett. **88** (2006).

[65] S. E. Harris, "Electromagnetically induced transparency," Phys. Today **50**, 36-42 (1997).

[66] C. Liu, Z. Dutton, C. H. Behroozi, and L. V. Hau, "Observation of coherent optical information storage in an atomic medium using halted light pulses," Nature **409**, 490-493 (2001).

[67] D. D. Smith, H. Chang, K. A. Fuller, A. T. Rosenberger, and R. W. Boyd, "Coupled-resonator-induced transparency," Physical Review A **69** (2004).

[68] L. Maleki, A. B. Matsko, A. A. Savchenkov, and V. S. Ilchenko, "Tunable delay line with interacting whispering-gallery-mode resonators," Opt. Lett. **29**, 626-628 (2004).

[69] M. F. Yanik, W. Suh, Z. Wang, and S. Fan, "Stopping light in a waveguide with an all-optical analog of electromagnetically induced transparency," Phys Rev Lett **93**, 233903 (2004).
[70] A. Naweed, G. Farca, S. I. Shopova, and A. T. Rosenberger, "Induced transparency and absorption in coupled whispering-gallery microresonators," Physical Review A **71** (2005).
[71] Q. F. Xu, S. Sandhu, M. L. Povinelli, J. Shakya, S. H. Fan, and M. Lipson, "Experimental realization of an on-chip all-optical analogue to electromagnetically induced transparency," Phys. Rev. Lett. **96** (2006).
[72] Q. F. Xu, J. Shakya, and M. Lipson, "Direct measurement of tunable optical delays on chip analogue to electromagnetically induced transparency," Opt. Express **14**, 6463-6468 (2006).
[73] K. Totsuka, N. Kobayashi, and M. Tomita, "Slow light in coupled-resonator-induced transparency," Phys. Rev. Lett. **98** (2007).
[74] L. Y. Mario and M. K. Chin, "Optical buffer with higher delay-bandwidth product in a two-ring system," Opt. Express **16**, 1796-1807 (2008).
[75] Y. F. Xiao, B. K. Min, X. Jiang, C. H. Dong, and L. Yang, "Coupling Whispering-Gallery-Mode Microcavities With Modal Coupling Mechanism," IEEE J. Quantum Electron. **44**, 1065-1070 (2008).
[76] A. Yariv and P. Yeh, *Photonics: Optical Electronics in Modern Communications*, 6th ed. (Oxford University Express, New York, 2007).
[77] E. Peral and A. Yariv, "Supermodes of grating-coupled multimode waveguides and application to mode conversion between copropagating modes mediated by backward Bragg scattering," J. Lightwave Technol. **17**, 942-947 (1999).
[78] D. Marcuse, *Theory of Dielectric Optical Waveguides* (Academic Press, New York and London, 1974).
[79] L. I. Schiff, *Quantum Mechanics* (McGraw-Hill, New York, 1955).
[80] X. Sun, H.-C. Liu, and A. Yariv, "Adiabaticity criterion and the shortest adiabatic mode transformer in a coupled-waveguide system," Opt. Lett. **34**, 280-282 (2009).